Control of Spin Transition Behaviour of Hofmann-type MOFs by Crystal Lattice Engineering

辻, 美穂

https://doi.org/10.15017/4059990

出版情報：九州大学, 2019, 博士（理学）, 課程博士
バージョン：
権利関係：

Control of Spin Transition Behaviour of Hofmann-type MOFs by Crystal Lattice Engineering

Miho Tsuji

March 2020

Department of Chemistry
Graduate School of Science
Kyushu University

Contents

General Introduction

Metal-organic Frameworks (MOFs)

Coordination polymers (CPs) have structures with infinite coordination, consisting of organic/inorganic ligands and metal ions, and they have been studied since the early 1960s.[1,2,3] The ordering framework and porous structure of CPs have attracted attention from research fields involving molecular magnets and porous materials.

In the late 1980s, a rational synthetic strategy for molecular magnets assembled with paramagnetic molecules was clearly presented.[4,5] Long-range magnetic ordering is achieved by the formation of the desired assembled structure by arranging paramagnetic centres via appropriate bridging ligands for a magnetic exchange interaction. Since magnetic ordering is a three-dimensional (3D) phenomenon, it is essential to design a framework to propagate the 3D magnetic interaction. After the establishment of the basic synthetic strategy, in the late 1990s, Kahn and co-workers found that some molecular magnets exhibited drastic changes in structure and magnetic behaviour with the adsorption/desorption of water.[6,7,8] They named this phenomenon a "*molecular magnetic sponge*." Then, molecular magnets were developed into multifunctional materials that had both magnetic properties and porosity. Our group has

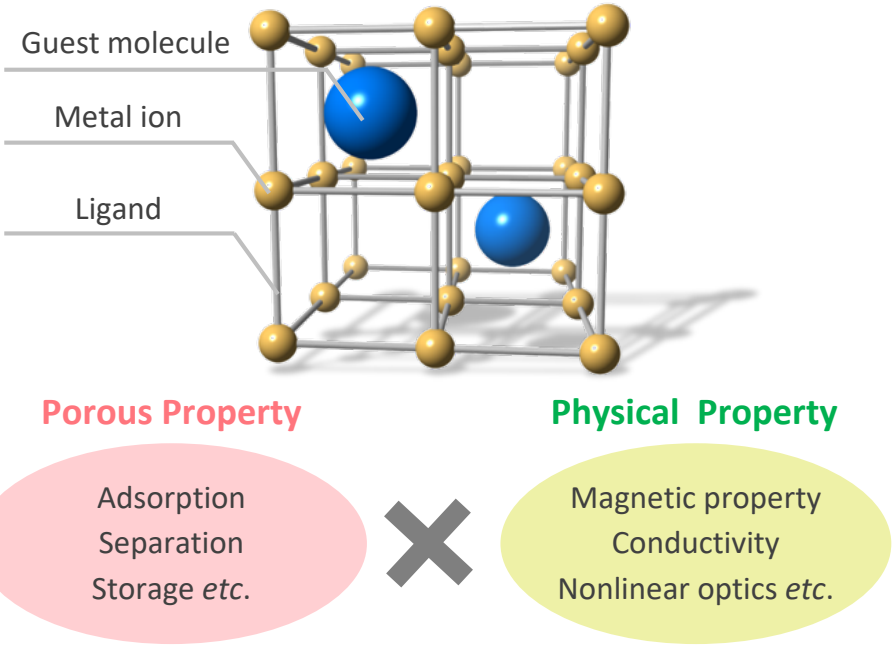

Figure 1. Schematic illustration of metal-organic frameworks (MOFs) and properties of MOFs

reported the magnetic switching behaviour of $[Ni(dipn)]_2[Ni(dipn)(H_2O)][Fe(CN)_6]_2 \cdot nH_2O$ (dipn = *N*,*N*-di(3-aminopropyl)amine; **Figure 3**).[9] Because of the orthogonality of the magnetic orbitals of the adjacent Ni^{II} and Fe^{III} ions, the as-synthesized crystalline compound (n = 11) showed ferromagnetic ordering at 9.5 K. However, the dehydrated compound (n = 0) showed paramagnetic behaviour with changes to the amorphous phase, implying that the ferromagnetic interaction was weakened via dehydration owing to disordered magnetic interaction pathways. In addition, the initial ferromagnetic behaviour and ordered structure were recovered by rehydration, which is a reversible structural and magnetic conversion involving hydration/dehydration. In the case of $[Mn(NNdmenH)(H_2O)][Cr(CN)_6] \cdot H_2O$ (NNdmenH = N,N-dimethylethylenediamine), a reversible transformation occurs between a two-dimensional (2D) sheet and a 3D framework by the formation/cleavage of cyano-bridges via dehydration/hydration.[10] These compounds are examples of how to solve the trade-off between porosity and long-range magnetic ordering. The framework design of molecular magnets and porous magnets is a basic design concept for the incorporation of physical properties into the porous framework and a basic mechanism for linking the physical properties with porous functions.

In contrast, Yaghi[11], Kitagawa[12], and Férey[13] focused on the “porosity” of CP in 1999. Porous materials have been used in our lives as water purification systems and deodorants since ancient times.[14] “Porous” coordination polymers (PCPs) or metal-organic frameworks (MOFs) are promising porous materials for gas storage[15,16], separation[17,18,19], heterogeneous catalysis[20,21], sensing[22,23,24], and other applications (**Figure 1**).[25,26,27,28] Compared with typical porous materials, such as zeolite and activated carbon, MOFs have narrow pore size distributions and highly regular and designable structures.[29,30] The porosity and guest-interactive sites for host–guest interactions can be tuned and designed by selecting the components in their frameworks. In 2012, Hupp and co-workers reported **NU-110E** ($[Cu_3(L^{6-})(H_2O)_3]$ (H_6L = 1,3,5-tris[((1,3-carboxylic acid-5-(4-(ethynyl)phenyl))ethynyl)phenyl]-benzene), which has a Brunauer–Emmett–Teller (BET) surface area of 7140 cm^{-1}.[31] Such large porosity paves the way for practical applications. In addition, MOFs provide guest-interactive sites: metal-metal bonds, hydrogen bonding and π-π, CH-π, Coulomb, and van der Waals interactions.[32,33] In particular, the open metal site (OMS) is a guest-interactive site that can be created by the removal of coordinated solvent molecules.[34,35,36] **MOF-74** ($M_2(L)$, L = 2,5-dioxidoterephthalate, M = Mg, Mn, Fe, Co, Ni, Cu, Ni, Cu, Zn) is a prototypical example of MOFs that have OMSs.[37,38] **Mg-MOF-74** (M = Mg), which includes open magnesium sites, showed CO_2 capture with a 8.9 wt.% capacity and release CO_2 at

80 °C.[34] More recently, Ghosh used **MOF-74** as a separator of benzene and cyclohexane, which have similar molecule sizes and boiling points, and found that OMS can interact with the π-cloud of benzene as a Lewis acid.[18] To introduce OMSs into MOF, Matsuda suggested the metal replacement approach.[35] This approach is classified in the category of mixed-metal MOFs, as described later. In **SIFSIX-1-Cu** [$Cu(SiF_6)(bpy)_2$] (bpy = 4,4'-bipyridine), Cu^{2+} ions have an octahedral geometry and no OMS. They attempted to exchange Cu^{2+} with Pd^{2+}, which has square planar geometry, while maintaining the original structure and stability. **SIFSIX-1-CuPd-10** [$Cu_{0.9031}Pd_{0.0969}(SiF_6)(bpy)_2$] is an isostructure of **SIFSIX-1-Cu**, and regarding the adsorption amount of O_2, **SIFSIX-1-CuPd-10** had much larger than that of **SIFSIX-1-Cu**, although the adsorption amount of Ar was similar because of the interaction between open palladium sites with O_2. These results indicate that a framework can be designed for each objective, and OMSs are useful guest-interactive sites that can be introduced into frameworks.

As mentioned above, the framework properties and porosities of CPs have been studied in parallel. In MOF research, the focus is changing from porosity to combination with the physical properties of the framework. Recently, the coexistence of magnetic properties and porosity has attracted interest in terms of promising applications, such as in magnetic sensors and switches.[39] These ideas are similar to the *molecular magnetic sponge* described above.[40] In 2002, a typical example of guest-driven spin crossover (SCO) behaviour was reported by Kepert and co-workers.[41] SCO phenomenon in $\{Fe_2(azpy)_4(NCS)_4 \cdot G\}$ (azpy = *trans*-4,4'-azopyridine) can be switched reversibly by alcohol vapour, which hydrogen bonds the framework. Miyasaka and co-workers used the electronic state modulation as a trigger to change the magnetic properties, which was not a structural change, and introduced donor D $\{Ru_2(O_2CPh\text{-}2,3,5\text{-}Cl_3)_4\}$ ($Cl_3PhCO_2^-$ = 2,3,5-trichlorobenzonate) and acceptor A $TCNQMe_2$ (2,5-dimethyl-7,7,8,8-tetracyanoquinodimethane) into the framework $[\{Ru_2(O_2CPh\text{-}2,3,5\text{-}Cl_3)_4\}_2(TCNQMe_2)]\cdot 4DCM$ (**1;** DCM = dichloromethane) (**Figure 2**).[42] This D_2A-layered magnetic system showed a large T_C change (ΔT_C = 70 K) with the electronic state modulation by desolvation/solvation of the guest molecules. This type of guest-induced electronic state modulation system has the potential to act as a multifunctional material that combines not only magnetism and porosity but also conductivity.

The physical and chemical properties of the framework extend not only to magnetic[43] but also to electrical[44,45,46] and optical properties.[28,47] The engineering of the framework enhances the possibility of MOFs as the multifunctional platform combining the physical properties with porosity.

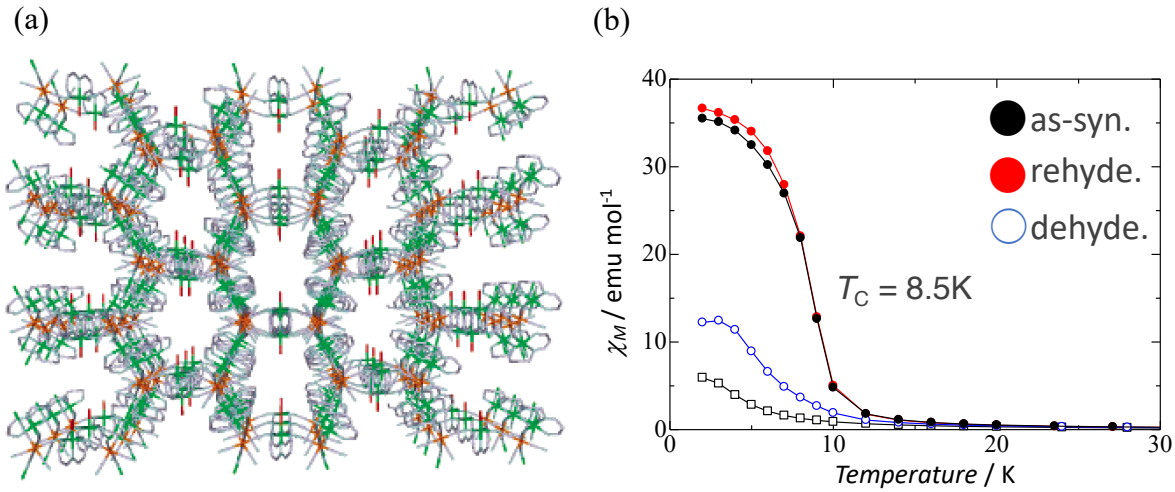

Figure 3. (a) Structure of $[Ni(dipn)]_2[Ni(dipn)(H_2O)][Fe(CN)_6]_2 \cdot nH_2O$ (dipn = N,N-di(3-aminopropyl)amine) viewed along the c-axis, with lattice water molecules omitted. Ni, Fe, and O atoms are indicated by green, orange, and red. (b) Temperature dependences of χM measured at an applied dc field of 500 Oe (black circles, n = 11; open circles, dehydrated form; red circles, rehydrated form; open squares, anhydrous form.

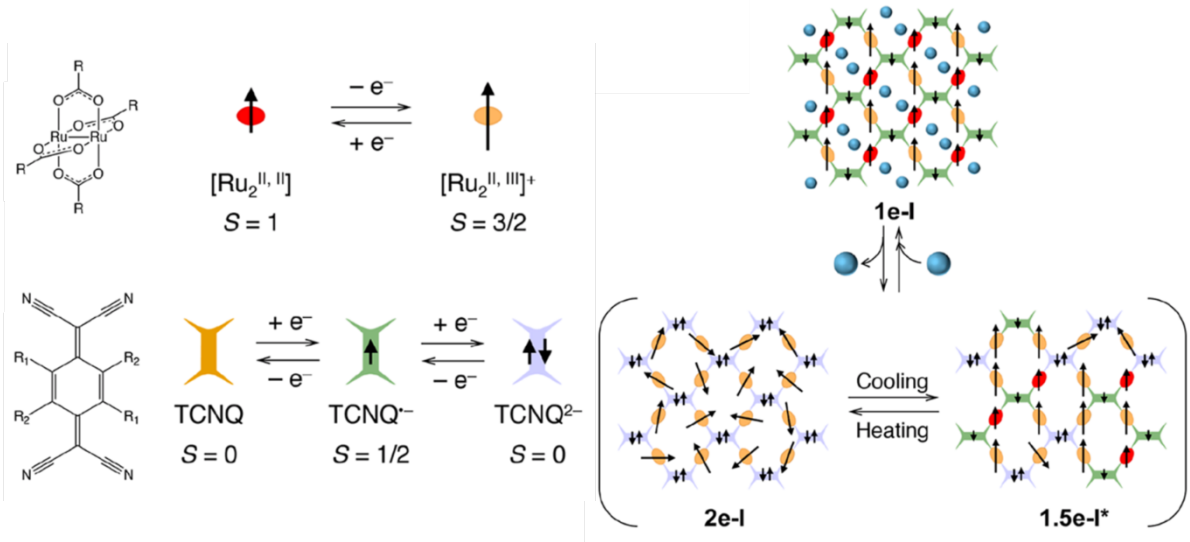

Figure 2. Schematic illustration of the redox reaction of [Ru2] complex with the TCNQ moiety and the electronic state of $[\{Ru_2\}_2(TCNQ)]$ (a D_2A system). 1e-I, 2e-I, and 1.5e-I* refer to the one electron-transferred ionic state, fully electron-transferred ionic state, and charge disproportionate-disordered ionic state, respectively.

Mixed-component MOFs

As mentioned above, MOFs can act a platform to combine porous materials with physical properties, and their possible applications can be enhanced by selecting different components.[48,49,50] By mixing components or combining MOFs, the physical properties can be tuned or exceed those of original single MOFs.[51,52,53] MOFs consisting of two or more components are classified as mixed-component MOFs (MC-MOFs; **Figure 4**).[48] When different metals (or ligands) have similar structural roles and these metals (or ligands) arrange completely random in a single MOF, they are called mixed-metal (or mixed-ligand) MOFs.[54,55] Mixed-metal (or mixed-ligand) MOFs are classified as solid solutions in which more than two kinds of solutes melt into each other. MC-MOFs consist of isostructural metals or ligands, which means that it is necessary to select components carefully to prevent an amorphous structure. One example of a mixed-ligand MOF, MTV-MOF (multivariate functionalities), was reported by Yaghi and coworkers.[56] They prepared 18 types of **MTV-MOF-5** structures by combining nine types of BDC (1,4-benzenedicarboxylate) derivatives -NH_2, -Br, -$(Cl)_2$, -NO_2, -$(CH_3)_2$, -C_4H_4, -$(OC_3H_5)_2$, and -$(OC_7H_7)_2$) that contain up to eight distinct functionalities in one phase. One of the **MTV-MOF-5** containing -NO_2, -$(OC_3H_5)_2$, and -$(OC_7H_7)_2$ exhibited a 400% better selectivity for carbon dioxide over carbon monoxide than the original **MOF-5**. The mixed-metal approach also creates multiple functionalities;[57] however, it is difficult to

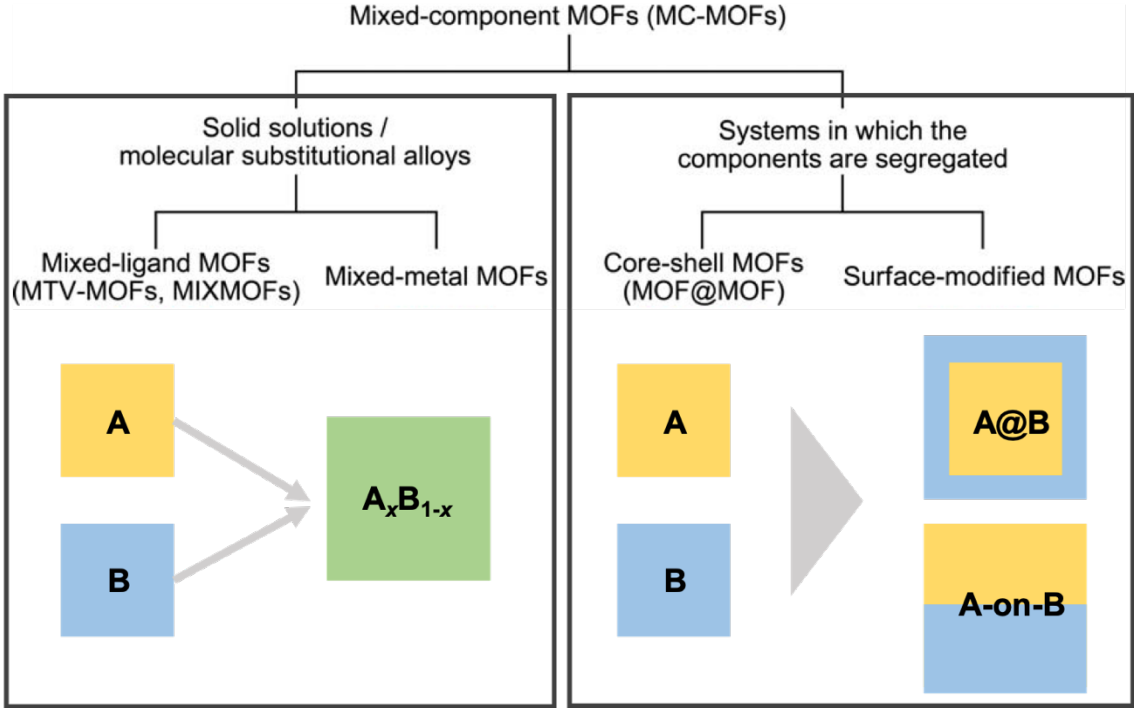

Figure 4. Classification of mixed-component MOFs (MC-MOFs)

select components because more than two different metals are used in the synthesis as a precursor, and the crystallizations of single metal phases compete with each other. For instance, in the case of **MIL-53(Cr-Fe)** $\{[Cr_{0.6}Fe_{0.4}(OH)_{0.7}F_{0.3}(bdc)]\cdot H_2O\}$, one of the components, Cr^{III}, is more inert than Fe^{III}. In the preparation of the single MOF **MIL-53(Cr)** precursor, chromium nitrate hydrate and terephthalic acid were heated in water at 493 K for 4 days. In contrast, **MIL-53(Fe)** was prepared from the more reactive Fe^{III} chloride in DMF at 423 K for only 1 day. Therefore, to obtain mixed-metal MOF **MIL-53(Cr-Fe)**, less reactive Fe^0 was used to control the reactivity. **MIL-53(Cr-Fe)** exhibited unique carbon dioxide adsorption behaviour that was different than that of the original MOFs of **MIL-53(Cr)** and **MIL-53(Fe)**.[58] At 283 K, **MIL-53(Cr)** uptakes carbon dioxide until 10 mmol/g, while **MIL-53(Fe)** uptakes it until approximately 3 mmol/g (＞20 bar); therefore, the calculated mixture (60/40% Cr/Fe) was expected to absorb carbon dioxide until approximately 7 mmol/g (＞20 bar). However, mixed-metal MOF **MIL-53(Cr-Fe)** showed adsorption up to 10 mmol/g with an adsorption hysteresis. This result indicated that the mixed phase of Cr (easy to open) and Fe (hard to open) sites provided unique adsorption properties exceeding the original single MOFs. Furthermore, by controlling the ratio of metal cations, the adsorption behaviour can be tuned on-demand without any change in the polarity of the pores. The other type of MC-MOFs include hetero-structured MOFs, which are called MOF-on-MOF[59,60,61] or core-shell type MOFs.[62,63,64] These hetero-structured MOFs can be formed via hetero-epitaxial growth in which a MOF is grown on another MOF surface.[48] Epitaxial growth is a way to grow crystals on another crystal as a substrate

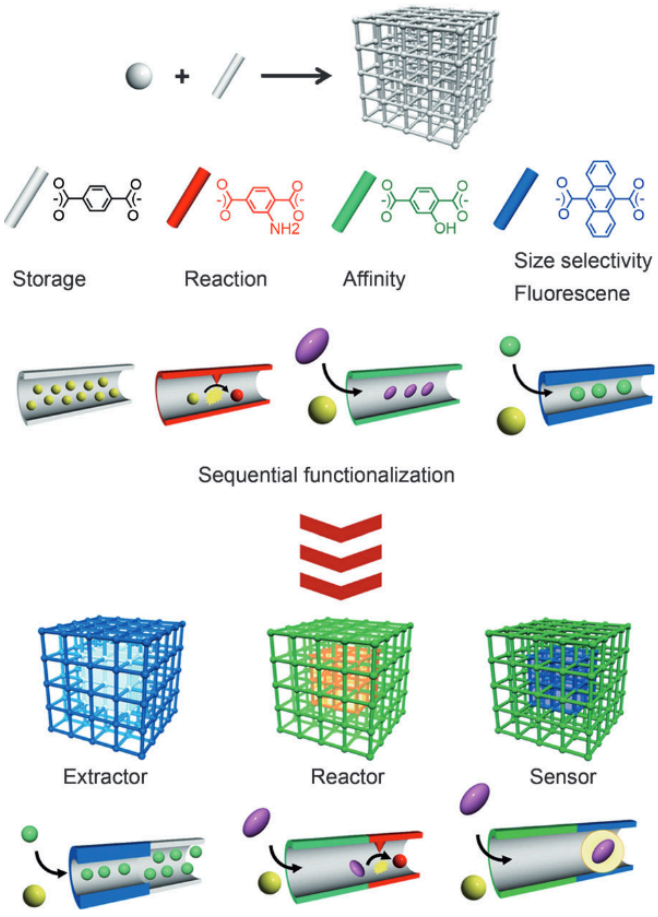

Figure 5. MOF crystal hybridization for sequential functionalization systems

while maintaining the orientation; therefore, the lattice parameters of the two crystals must be close. The first report on the hetero-epitaxy of bulk MOF was on a core-shell A@B structure using $\{Zn_2(ndc)_2$-(dabco)$\}$ as the core crystal A and $\{Cu_2(ndc)_2(dabco)\}$ as the shell crystal B (ndc = 1,4-naphthalenedicarboxylate, dabco = diaza bicyclo[2.2.2]octane).[60] Core-shell MOF A@B is one of the promising hierarchical materials than has an arrangement of chemical functionalities at the desired positions (

Figure 5**)**.[65] S. Kitagawa et al. fabricated a core-shell MOF that has $\{Zn_2(adc)_2(dabco)\}$ (**2**) (adc = 9,10-anthracene dicarboxylate; pore sizes 1.7 × 1.7 $Å^2$ along the c axis, 4.5 × 2.7 $Å^2$ along the *a* and *b* axes; micropore volume of 0.31 cm^3g^{-1}) as the size separation filter and $\{Zn_2(bdc)_2(dabco)\}$ (**1**) (pore sizes 7.5 × 7.5 $Å^2$ along the *c* axis, 5.3 × 3.2 $Å^2$ along the *a* and *b* axes; micropore volume 0.75 of cm^3g^{-1}) as the storage container in the core.[66] The prepared core-shell type MOF **1@2** could separate cetane (*n*-hexadecane) from its branched isomer, isocetane (2,2,4,4,6,8,8-heptamethylnonane), although when using a 1:100 mixture of cetane/isocetane, the cetane storage amount was enhanced compared with that of the original MOF. This result showed the possibility of enhancing the properties of MOFs by combining with other MOFs, which have different roles as heterogeneous arrangements.

Crystal lattice engineering enables to design the pore space or layered structure by forming mixed-metal MOFs or hetero-structured MOF, respectively. The author focused on MC approach as a method of crystal lattice engineering to modulate or enhance the physical properties and functions.

Hofmann-type MOFs

The spin crossover (SCO) phenomenon was first observed in 1931[67], and this phenomenon has attracted attention from a theoretical point of view because of the possibility of realizing devices.[68,69,70] The SCO phenomenon is explained by ligand field theory.[71,72] For octahedral coordination compounds, the *d* orbital splits into t_{2g} and e_g sets, and the spin state of d^4 – d^7 coordination compounds is either a high spin (HS) or low spin (LS) state depending on the ligand field strength. For example, in the case of Fe^{II}, $t_{2g}^4e_g^2$ (T_{2g}) and $t_{2g}^6e_g^0$ (A_{1g}) configurations correspond to the HS and LS states, respectively. When the strength of the ligand field is appropriate, the difference in the zero-point energies for the HS and LS states, $\Delta E^0_{HL} = E^0_{HS} - E^0_{LS}$, can fall within a range of thermal energies. When the cooperativity is strong, abrupt or even hysteretic SCO behaviour can occur. Magnetic hysteresis is important for practical applications, such as memory storage and switching devices. To obtain strong cooperativity, the introduction of interactions (e.g. π-π interaction and hydrogen bonding) or covalent linkers to form coordination polymers are effective, which means MOFs are suitable compounds.[73,74] The series of Hofmann-type coordination polymers have been expanded to $\{[M^{II}(L)_nM'^{II}(CN)_4]\cdot G\}$ (M^{II} = Mn, Fe, Co, Ni, Cu, Zn, or Cd and M'^{II} = Ni, Pd, or Pt), where L can represent unidentate ligands or bridging ligands to form 2D or 3D coordination networks.[75,76,77] The SCO phenomenon of Hofmann-type MOF $\{Fe(py)[Ni^{II}(CN)_4]\}$ (py = pyridine) was reported by Kitazawa and co-workers in 1996.[78,79] However, their ST temperatures were lower than room temperature. To obtain

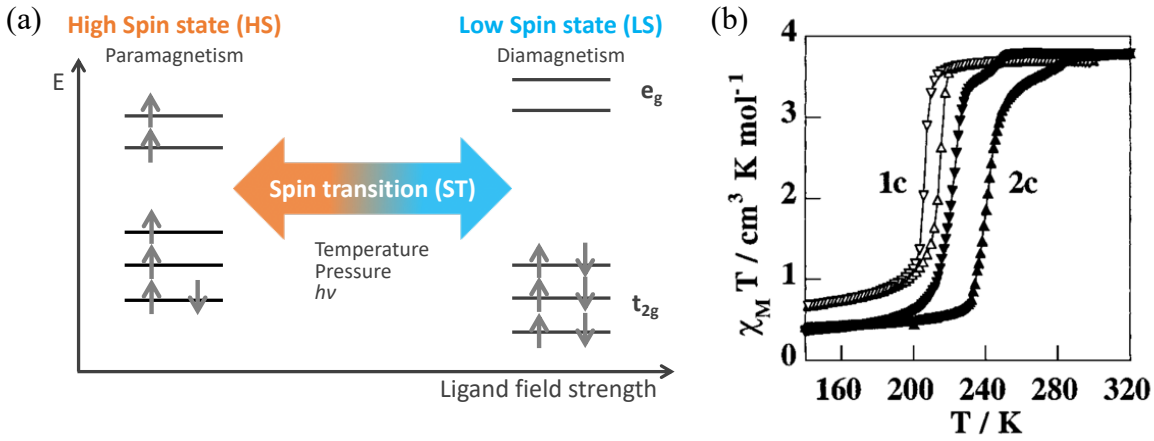

Figure 6. (a) Electronic configurations of the high spin (HS) state and low spin (LS) state of the d^6 transition metal in an octahedral ligand field (b) $\chi_M T$ *vs.* *T* plot (χM: molar magnetic susceptibility) and for 2D structure $\{Fe(py)[Pt^{II}(CN)_4]\}$ (**1c**; py = pyridine) and 3D structure $\{Fe(pz)[Pt^{II}(CN)_4]\}$ (**2c**; pz = pyrazine)

both a high ST temperature and hysteresis width, it is important to change the pillar ligands from pyridine to pyrazine because the internal pressure originating from the more rigid 3D structures can result in a stronger ligand field at the Fe^{II} sites. As a result, 3D Hofmann-type MOFs, $\{Fe(pz)[M^{II}(CN)_4]\cdot nH_2O\}$ (pz = pyrazine, M = Ni, Pd, Pt(**1**)), showed higher ST temperatures (T_C^{up} = 240–305 K and T_C^{down} = 220–280 K) and a wide hysteresis near 25 K (**Figure 6**).[79] These 3D networks have solvent-accessible voids depending on the spin state (LS state: 18.1% and HS state: 22.4 %). Interestingly, guest adsorption can be used as a driving force to change the magnetic behaviours, and these guest-induced magnetic responses have been studied.[80,10,81] Hofmann-type MOFs have two kinds of guest-interactive sites: one is the open metal sites (OMS; M^{II}) mentioned in the general introduction and the other is between the pz-bridges with π-π interaction (**Figure 7 (a)**). Through the adsorption of guest molecules, the spin state can be changed. M. Ohba and S. Kitagawa reported spin-state switching in a 3D Hofmann-type MOF reversibly using carbon disulphide and benzene vapour (**Figure 7 (b)**).[82] Benzene adsorption stabilized the HS state because benzene was a large molecule for the framework and expanded framework, which means that the shrinkage of the framework was prevented. Six- or five-membered aromatic molecules, such as pyrazine, pyridine, thiophene, pyrrole, and furan, or solvents, such as methanol, ethanol, propanol, and tetrahydrofuran, have similar effects on the framework and spin state. In contrast, carbon disulphide adsorption stabilized the LS state. To consider the effect of carbon disulphide adsorption, the position of CS_2 in the framework is important. One S atom in carbon disulphide is located between two pz ligands, and the other S atom is between two OMSs (Ni, Pd, or Pt).[83] The position of this carbon disulphide molecule suppresses the pyrazine rotation in both the HS and LS states, which decreases the rotational entropy difference (ΔS_{rot}^{HS-LS}) between the HS and LS states.[84] However, a similarly shaped molecule, carbon dioxide, is located between two OMSs. This difference in adsorption position can be explained by the difference in stabilization interaction. carbon dioxide absorption is stabilized by the electrostatic interaction with the $Pt(CN)_4$; however, the carbon disulphide absorption is stabilized by the dispersion interaction with two pz molecules. Considering the polarizability of carbon disulphide and carbon dioxide, carbon disulphide is much larger than carbon dioxide. This larger polarization results in a larger dispersion interaction in carbon disulphide. Only when a gas molecule is present between the pz rings can two pz molecules induce a considerably large dispersion interaction, and this dispersion interaction determines the carbon disulphide position in the framework.

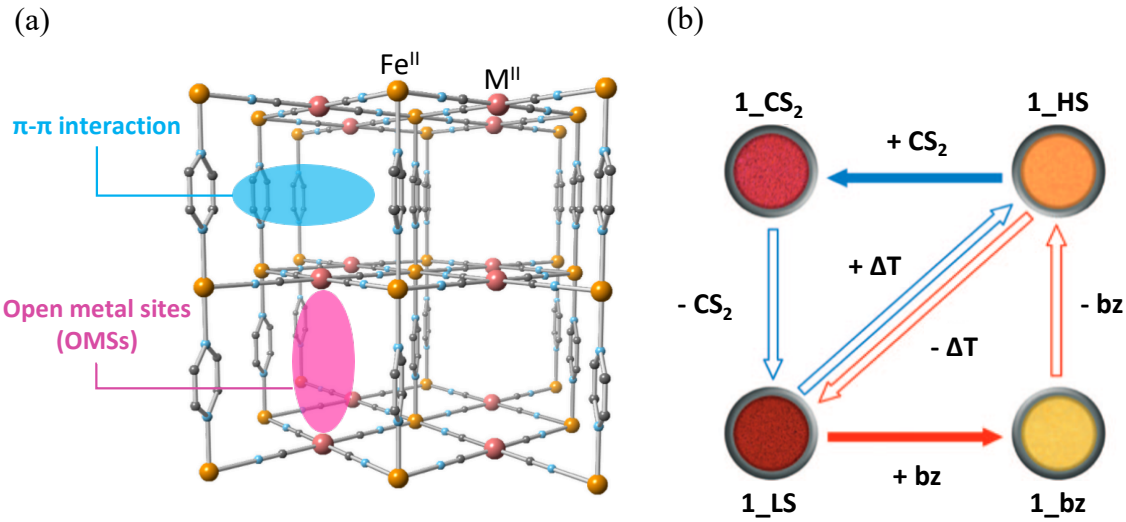

Figure 7. (a) Structure of 3D Hofmann-type MOF $\{Fe(pz)[M^{II}(CN)_4]\}$ (pz = pyrazine, M = Ni, Pd, Pt (**1**)) and interactive sites: open metal sites and π-π interaction between pz rings (b) Schematic chemical and thermal memory process and sample colour from the photos of compound **1**. After removal of guest molecules, bz (benzene) and carbon disulphide, the colour of samples did not change, which means the spin state was maintained.

Some guest molecules, such as SO_2, interact strongly with OMSs. SO_2 molecules are coordinated to Pt^{II} sites by an S atom which means that SO_2 adsorption is chemisorption (not physisorption) in other gases, such as N_2, O_2. The MOF absorbed ca. 1 mol of SO_2 per mol of **1**, and the LS state was stabilized. Thus, the ST temperature, T_C^{up}, increased compared with that of the guest-free **1**.[85] According to DFT calculations, SO_2 molecules and Pt atoms formed a tilted pyramidal coordination geometry. Considering this geometry of SO_2, there was no significant interaction between pz rings and SO_2 molecules, and the barrier of pz ring rotation increased slightly (LS state: approximately 2 kcal/mol) compared with guest-free **1**. Halogen adsorb with chemisorption as well as SO_2 molecules. Real et al. prepared halogen adducts of $\{Fe(pz)[Pt(CN)_4(X)_n]\}$ ($X^- = Cl$ ($n = 1$; **1_Cl**), Br ($n = 1$; **1_Br**), I ($0 \leq n \leq 1$; **1_I**)) (**Figure 8 (a)**). The single crystal of **1_I** retained the tetragonal *P*4/*mmm* space group; however, the crystal parameter was similar to the LS state of guest-free **1** at 293 K. Upon increasing the temperature up to 395 K, the colour of the crystal changed to yellow, indicating the HS state, and the crystal parameter agreed with this change in colour. Their results indicated an increase in ST temperature, T_C^{up}. The OMS: Pt sites were coordinated by two halogen anions with half occupancy, forming an alternate arrangement of $[Pt^{II}(CN)_4]^{2-}$ and $[Pt^{IV}(CN)_4(X)_2]^{2-}$, according to the results of the XPS spectra, the ratio

of Pt/X, and the Pt–I bond distance. From the thermal dependence of $\chi_M T$ (χ_M is the molar magnetic susceptibility and T is the temperature), the critical temperatures, T_C^{up}, were 270 K (**1_Cl**), 324 K (**1_Br**), and 392 K (**2_I**); T_C^{down} = 258 K (**1_Cl**), 293 K (**1_Br**), and 372 K (**1_I**), respectively (**Figure 8 (b)**). Because of the enhancement in the σ-donor capability of the nitrogen through the π-donor capability of halide X^-, the LS state became stabilized, and T_C^{up} increased. This trend of increasing T_C^{up} corresponds to the electronegativity of halogen X. The π-donor capability of halide X^- decreases with increasing electronegativity; therefore, the smaller electronegative iodide showed the highest T_C^{up}. Thus, according to these results, the modification of OMSs is useful for modulating the magnetic behaviour in 3D Hofmann-type MOFs.

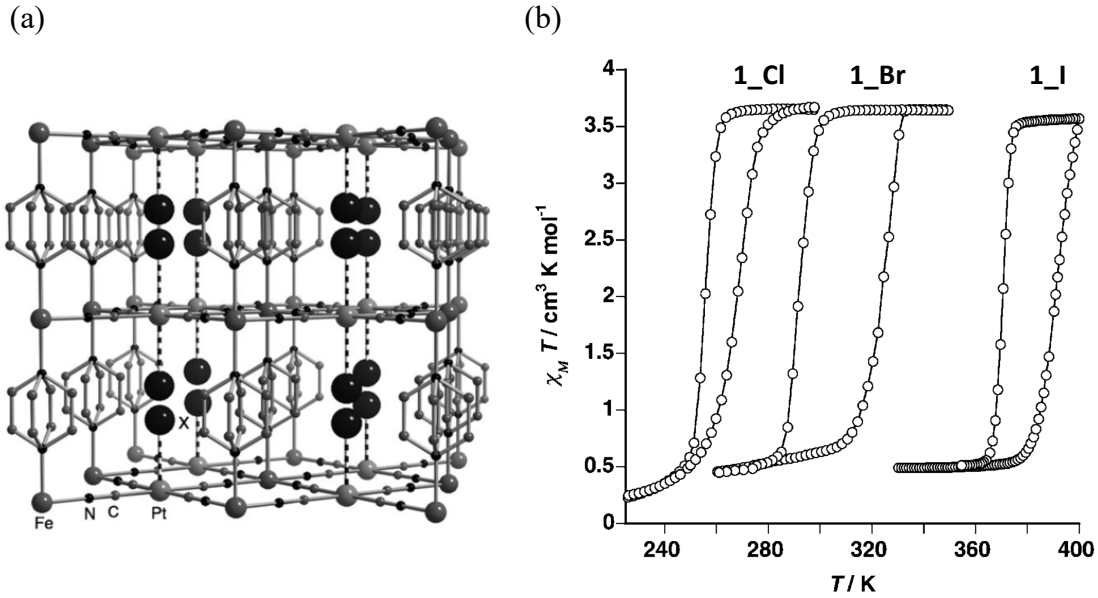

Figure 8. (a) Structure of halogen adducts {Fe(pz)[Pt(CN)$_4$(X)$_n$]} (X^- = Cl (n = 1; **1_Cl**), Br (n = 1; **1_Br**), I (n = 1; **1_I**)). The occupancy of the X atoms was 0.5, and the Pt atoms were in a mixed-valence state (Pt^{II}/Pt^{IV}). The pyrazine ligands were disordered about the C_4 axis. (b) $\chi_M T$ *vs.* T plot for halogen adducts

Concept of This Research

In this research, we designed a pore space (Chapter 1) and layered structure (Chapter 2) through a mixed-component approach to control the physical properties using the behaviour of guest molecules in the pores (**Figure 9)**. Hofmann-type MOFs were selected as a platform in this research for two reasons. (i) There was a variety of components; Hofmann-type MOFs can be expanded to $\{[M^{II}(L)_nM'^{II}(CN)_4]\cdot G\}$ (M^{II} = Mn, Fe, Co, Ni, Cu, Zn, or Cd and M'^{II} = Ni, Pd, or Pt), where L can represent unidentate ligands or bridging ligands to form 2D or 3D coordination networks. (ii) Guest-responsible magnetic properties exist; when Fe^{II} is used for the framework, it exhibits a spin crossover (SCO) phenomenon. The interaction between guest molecules and the framework affects the spin state; thus, the magnetic behaviour can provide a clue to understanding guest molecule behaviours in the pores. In particular, 3D Hofmann-type MOFs, $\{Fe(pz)[M(CN)_4]\}$ (pz = pyrazine, M = Pt (**1**), Pd (**2**), Ni), were selected because they have a high crystallinity structure, and there is considerable of knowledge about their guest responsivity. For example, compounds **1** and **2**, which have Pt or Pd sites as OMSs, are ideal combinations for forming MC-MOFs because of their similar lattice parameters. As a guest molecule, iodine was selected because it provides different magnetic behaviours depending on the difference in open metal sites (OMSs) of Pt and Pd. In the

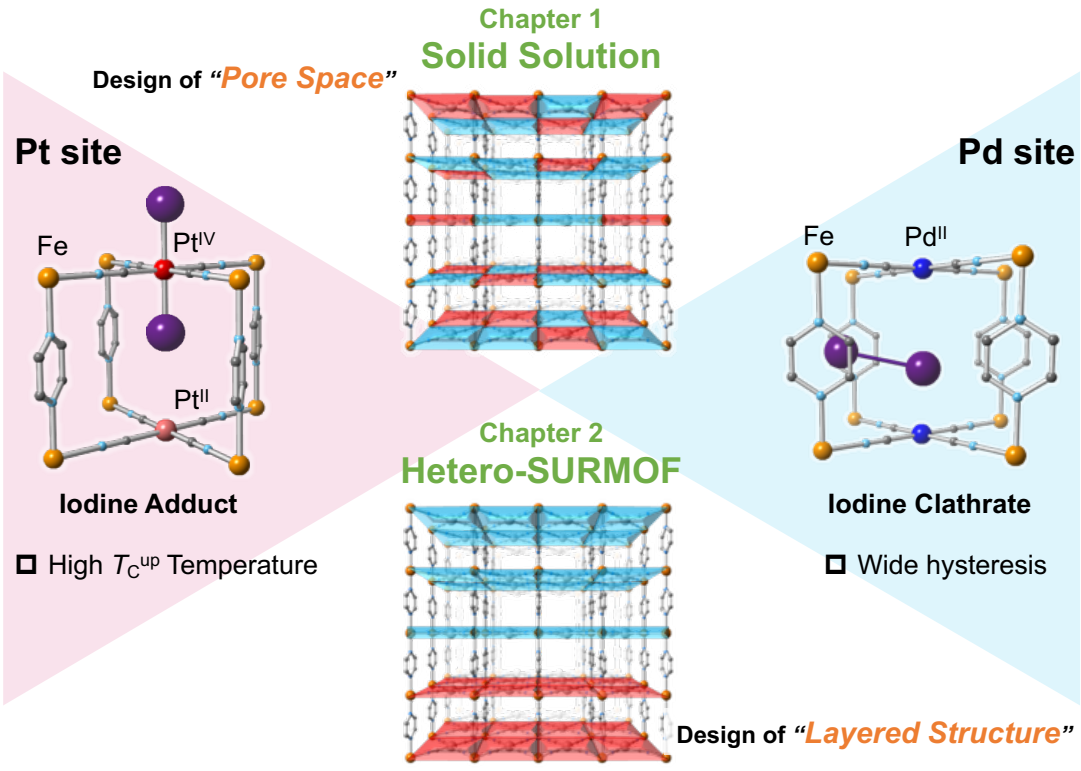

Figure 9. Concept of this research

case of **1**, the mixed-valence state is {Fe(pz)[$Pt^{II/IV}(CN)_4(I)_n$]} (**1_I**; n = 0.0–1.0) because iodine coordinates to Pt sites, and $[Pt^{II}(CN)_4]^{2-}$ and $[Pt^{IV}(CN)_4(X)_2]^{2-}$ arrange alternately (**Figure 10**). The spin transition (ST) temperature of iodine adducts **1_I** increased up to 398 K.[86] However, for **2**, iodine is confined as an I_2 molecule between two Pd centres so that it forms an iodine clathrate of {Fe(pz)[$Pd(CN)_4$]·0.95I_2} (**2_I**; **Figure 11**). In the large pores in the HS state, I_2 molecules have a high mobility and prevent shrinkage for the framework. In contrast, in the small pores in the LS state, I_2 molecules are immobilized through interactions with Pd sites and pyrazine rings. As a result, **2_I** exhibits ST with a wide hysteresis of 94 K through the order-disorder transition of the confined I_2 molecules. Based on these previous studies, the author attempted to control the iodine behaviour in the pore and modulate the magnetic behaviour associated with the iodine behaviour by designing the pore space or crystal structure through the mixed-component approach by using **1** and **2**.

In Chapter 1, the author describes how the pore space was designed using a mixed-metal approach. Solid solutions {Fe(pz)[$Pt_xPd_{1-x}(CN)_4$]} (**3*x***) are expected to form easily because **1** and **2** have similar lattice parameters. Iodine-containing **3*x*_I** will provide different magnetic behaviours depending on the ratio of the Pt and Pd: x values. In Chapter 2, the author describes how the layered structure was designed by arranging Pt and Pd sites using the layer-by-layer (LbL) method. The LbL method is useful to

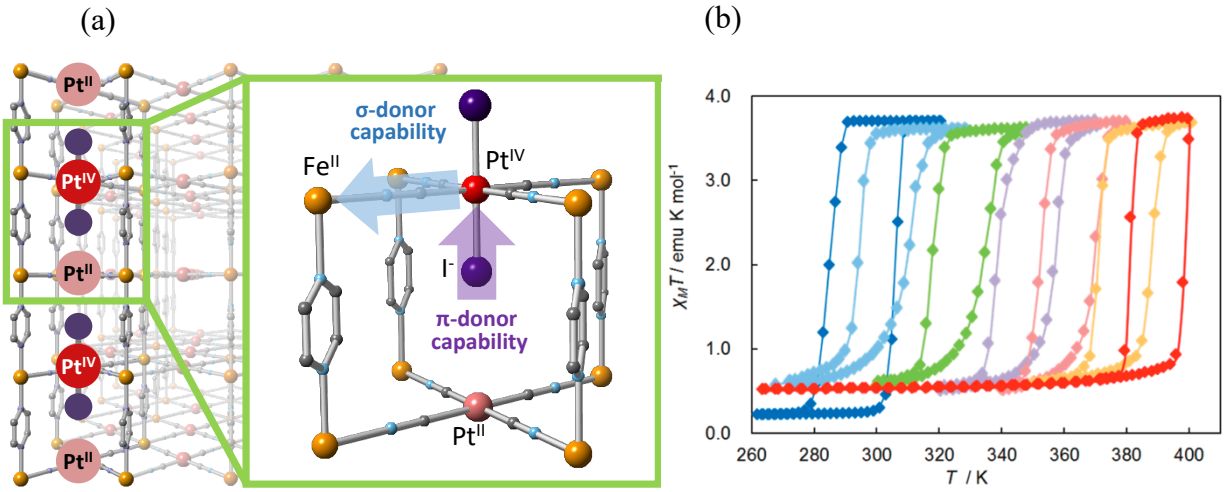

Figure 10. (a) Schematic structure of {Fe(pz)[$Pt^{II/IV}(CN)_4(I)_n$]} (**1_I**, n = 0.0–1.0), which forms I–Pt^{IV}–I bonds and a mixed valance arrangement. The strong π-donor capability of iodide enhances the σ-donor capability of the cyano nitrogen through the Pt^{IV} site. (b) Magnetic behaviour of **1_I**; n = 0.0 (blue); 0.1 (sky blue); 0.3 (green); 0.5 (violet); 0.7 (pink); 0.9 (orange); 1.0 (red). The spin transition temperature, T_C^{up}, increases with increasing amount of iodine (n).

prepare high crystallinity and orientation MOF thin films called SURMOF (surface-mounted MOF). Therefore, the Pt site layer and the Pd site layer will be separated like the forming domain in the hetero-structured SURMOF. This means that I–Pt^{IV}–I bonds and the confiding I_2 molecule space are expected to be separated in these hetero-SURMOFs; thus, the layer arrangement will affect the ST behaviour.

(a)

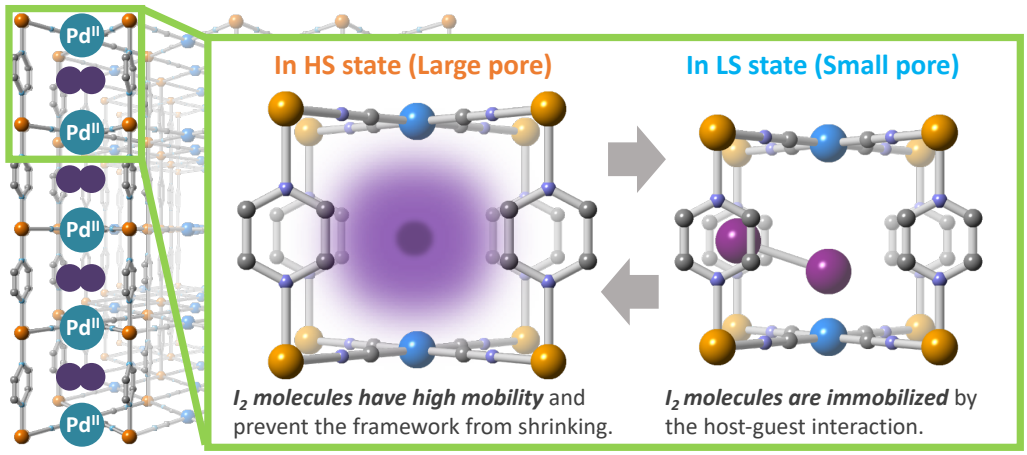

(b)

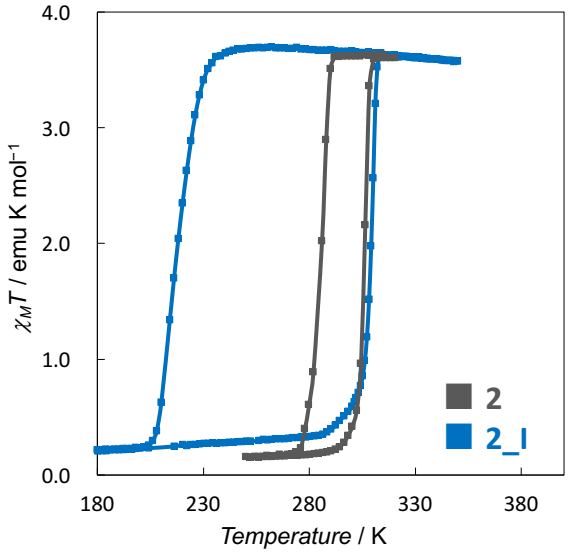

Figure 11. (a) Schematic structure of {Fe(pz)[Pd(CN)$_4$]·0.95I$_2$} (**2_I**), which confines iodine as I_2 molecules and forms iodine clathrate. In the HS state, the framework is prevented form shrinking because of I_2 mobility in the pores. In contrast, I_2 molecules are immobilized in the LS state. (b) Magnetic behaviour of guest-free **1** (grey) and iodine clathrate **2_I** (light blue)

References

1. Kitagawa, S.; Kitaura, R.; Noro, S., *Angew. Chem. Int. Ed.*, **2004**, *43*, 2334−2375.
2. James, S. L., *Chem. Soc. Rev.*, **2003**, *32*, 276−288.
3. Batten, S. R.; Robson, R., *Angew. Chem. Int. Ed.*, **1998**, *37*, 1460−1494.
4. Chittipeddi, S. R.; Miller, J. S.; Rommelmann, H.; Chittipeddi, S. R.; Zhang, J. H.; Reiff, W. M.; Epstein, A. J., *J. Am. Chem. Soc.*, **1987**, *109*, 769−781.
5. Caneschi, A.; Gatteschi, D.; Sessoli, R.; Rey, P., *Inorg. Chem.*, **1988**, *27*, 1756−1761.
6. Kahn, O.; Larionova, J.; Yakhmi, J. V., *Chem. Eur. J*. **1999**, *5*, 3443−3449.
7. Pinkowicz, D.; Podgajny, R.; Sieklucka, B., Molecular Magnetic Materials: Concepts and Applications, Chapter 11, **2016**.
8. Larionova, J.; Chavan, S. A.; Yakhmi, J. V.; Frøystein, A. G.; Sletten, J.; Sourisseau, C.; Kahn, O., *Inorg. Chem.*, **1997**, *36*, 6374−6381.
9. Yanai, N.; Kaneko, W.; Yoneda, K.; Ohba, M.; Kitagawa, S., *J. Am. Chem. Soc*. **2007**, *129*, 3496−3497.
10. Kaneko, W.; Ohba, M.; Kitagawa, S., *J. Am. Chem. Soc.*, **2007**, *129*, 13706−13712.
11. Li, H.; Eddaoudi, M.; O'Keeffe, M.; Yaghi, O. M., *Nature*, **1999**, *402*, 276−279.
12. Kitagawa, S.; Kondo, M., *Bull. Chem. Soc. Jpn*., **1998**, *71*, 1739−1753.
13. Cheetham, A. K.; Férey, G.; Loiseau, T., *Angew. Chem. Int. Ed.*, **1999**, *38*, 3268−3292.
14. Davis, M. E., *Nature*, **2002**, *417*, 813−821.
15. Morris, R. E.; Wheatley, P. S., *Angew. Chem. Int. Ed.*, **2008**, *47*, 4966−4981.
16. Janiak, C., *Dalton. Trans.*, **2003**, 2781−2804.
17. Li, B.; Wen, H. M.; Zhou, W.; Chen, B., *J. Phys. Chem. Lett.*, **2014**, *5*, 3468−3479.
18. Mukherjee, S.; Manna, B.; Desai, A. V.; Yin, Y.; Krishna, R.; Babarao, R.; Ghosh, S. K., *Chem. Commun.*, **2016**, *52*, 8215−8218.
19. Li, J. R.; Kuppler, R. J.; Zhou, H. C., *Chem. Soc. Rev.*, **2009**, 38, 1477−1504.
20. Chughtai, A. H.; Ahmad, N.; Younus, H. A.; Laypkov, A.; Verpoort, F., *Chem. Soc. Rev.*, **2015**, *44*, 6804−6849.
21. Lee, J.; Farha, O. K.; Roberts, J.; Scheidt, K. A.; Nguyen, S. T.; Hupp, J. T., *Chem. Soc. Rev.*, **2009**, *38*, 1450−1459.
22. Dong, M. J.; Zhao, M.; Ou, S.; Zou, C.; Wu, C. De., *Angew. Chem. Int. Ed.*, **2014**, 53, 1575−1579.
23. Chen, L.; Liu, D.; Peng, J.; Du, Q.; He, H. *Coord. Chem. Rev*., **2020**, *404*.
24. Kreno, L. E.; Leong, K.; Farha, O. K.; Allendorf, M.; Van Duyne, R. P.; Hupp, J. T., *Chem. Rev.*, **2012**, *112*, 1105−1125.

25. Furukawa, H.; Cordova, K. E.; O'Keeffe, M.; Yaghi, O. 974M., *Science*, **2013**, *341*,1230444-1−1230444-12.
26. Li, B.; Wen, H. M.; Cui, Y.; Zhou, W.; Qian, G.; Chen, B., *Adv. Mater.*, **2016**, *28*, 8819−8860.
27. Czaja, A. U.; Trukhan, N.; Müller, U., *Chem. Soc. Rev.*, **2009**, *38*, 1284−1293.
28. Hu, Z.; Deibert, B. J.; Li, J., *Chem. Soc. Rev.*, **2014**, *43*, 5815−5840.
29. Furukawa, H.; Ko, N.; Go, Y. B.; Aratani, N.; Choi, S. B.; Choi, E.; Yazaydin, A. Ö.; Snurr, R. Q.; O'Keeffe, M.; Kim, J., *Science*, **2010**, *329*, 424−428.
30. Schneemann, A.; Bon, V.; Schwedler, I.; Senkovska, I.; Kaskel, S.; Fischer, R. A., **2014**, *43*, 6062−6096.
31. Farha, O. K.; Eryazici, I.; Jeong, N. C.; Hauser, B. G.; Wilmer, C. E.; Sarjeant, A. A.; Snurr, R. Q.; Nguyen, S. T.; Yazaydin, A. Ö.; Hupp, J. T., *J. Am. Chem. Soc.*, **2012**. *134*, 15016−15021.
32. Li, Q.; Zhang, W.; Miljanić, O. Š.; Sue, C. H.; Zhao, Y. L.; Liu, L.; Knobler, C. B.; Stoddart, J. F.; Yaghi, O. M., *Science*, **2009**, *325*, 855−859.
33. Chen, B.; Xiang, S.; Qian, G., *Acc. Chem. Res.*, **2010**, *43*, 1115−1124.
34. Britt, D.; Furukawa, H.; Wang, B.; Glover, T. G.; Yaghi, O. M., *Proc. Nat. Acad. Sci. U. S. A.*, **2009**, *106*, 20637−20640.
35. Harada, Y.; Hijikata, Y.; Kusaka, S.; Hori, A.; Ma, Y.; Matsuda, R., *Dalton. Trans.*, **2019**, *48*, 2545−2548.
36. Kim, H. K.; Yun, W. S.; Kim, M. B.; Kim, J. Y.; Bae, Y. S.; Lee, J. D.; Jeong, N. C., *J. Am. Chem. Soc.*, **2015**, *137*, 10009−10015.
37. Wu, H.; Zhou, W.; Yildirim, T., *J. Am. Chem. Soc.*, **2009**, *131*, 4995−5000.
38. Bloch, E. D.; Queen, W. L.; Krishna, R.; Zadrozny, J. M.; Brown, C. M.; Long, J. R., *Science*, **2012**, *335*, 1606−1610.
39. Hou, C.; Wang, Y.; Ding, Q.; Jiang, L.; Li, M.; Zhu, W.; Pan, D.; Zhu, H.; Liu, M., *Nanoscale*, **2015**, *7*, 18770−18779.
40. Dechambenoit, P.; Long, J. R., *Chem. Soc. Rev.*, **2011**, *40*, 3249−3265.
41. Halder, G. J.; Kepert, C. J.; Moubaraki, B.; Murray, K. S.; Cashion, J. D., *Science*, **2002**, *298*, 1762−1765.
42. Zhang, J.; Kosaka, W.; Sugimoto, K.; Miyasaka, H., *J. Am. Chem. Soc.*, **2018**, *140*, 5644−5652.
43. Coronado, E.; Mínguez Espallargas, G., *Chem. Soc. Rev.*, **2013**, *42*, 1525−1539.
44. Jain, P.; Ramachandran, V.; Clark, R. J.; Hai, D. Z.; Toby, B. H.; Dalal, N. S.; Kroto, H. W.; Cheetham, A. K., *J. Am. Chem. Soc.*, **2009**, *131*, 13625−13627.

45. Hurd, J. A.; Vaidhyanathan, R.; Thangadurai, V.; Ratcliffe, C. I.; Moudrakovski, I. L.; Shimizu, G. K. H., *Nat. Chem*., **2009**, *1*, 705−710.
46. Givaja, G.; Amo-Ochoa, P.; Gómez-García, C. J.; Zamora, F., *Chem. Soi, Rev.*, **2012**, *41*, 115−147.
47. Liu, D.; Lu, K.; Poon, C.; Lin, W., *Inorg. Chem.*, **2014**, *53*, 1916−1924.
48. Burrows, A. D., *Cryst. Eng. Comm.*, **2011**, *13*, 3623−3642.
49. Bae, Y. S.; Mulfort, K. L.; Frost, H.; Ryan, P.; Punnathanam, S.; Broadbelt, L. J.; Hupp, J. T.; Snurr, R. Q., *Langmuir*, **2008**, *24*, 8592−8598.
50. Das, M. C.; Guo, Q.; He, Y.; Kim, J.; Zhao, C. G.; Hong, K.; Xiang, S.; Zhang, Z.; Thomas, K. M.; Krishna, R., *J. Am. Chem. Soc.*, **2012**, *134*, 8703−8710.
51. Dhakshinamoorthy, A.; Asiri, A. M.; Garcia, H., *Catal. Sci. Technol.*, **2016**, *6*, 5238-5261.
52. Qin, J. S.; Yuan, S.; Wang, Q.; Alsalme, A.; Zhou, H. C., *J. Mater. Chem. A.*, **2017**, *5*, 4280−4291.
53. Lu, W.; Wei, Z.; Gu, Z. Y.; Liu, T. F.; Park, J.; Park, J.; Tian, J.; Zhang, M.; Zhang, Q.; Gentle, T., *Chem. Soc. Rev.*, **2014**, *43*, 5561−5593.
54. Masoomi, M. Y.; Morsali, A.; Dhakshinamoorthy, A.; Garcia, H., *Angew. Chem. Int. Ed.*, **2019**, *58*, 15118−15205.
55. Das, M. C.; Xiang, S.; Zhang, Z.; Chen, B., *Angew. Chem. Int. Ed.*, **2011**, *50*, 10510−10520.
56. Deng, H.; Doonan, C. J.; Furukawa, H.; Ferreira, R. B.; Towne, J.; Knobler, C. B.; Wang, B.; Yaghi, O. M., *Science*, **2010**, *327*, 846−850.
57. Abednatanzi, S.; Gohari Derakhshandeh, P.; Depauw, H.; Coudert, F. X.; Vrielinck, H.; Van Der Voort, P.; Leus, K., *Chem. Soc. Rev.*, **2019**, *48*, 2535−2565.
58. Nouar, F.; Devic, T.; Chevreau, H.; Guillou, N.; Gibson, E.; Clet, G.; Daturi, M.; Vimont, A.; Grenèche, J. M.; Breeze, M. I., *Chem. Commun.*, **2012**, *48*, 10237−10239.
59. Kim, D.; Lee, G.; Oh, S.; Oh, M., *Chem. Commun*., **2019**, *55*, 43−46.
60. Furukawa, S.; Hirai, K.; Nakagawa, K.; Takashima, Y.; Matsuda, R.; Tsuruoka, T.; Kondo, M.; Haruki, R.; Tanaka, D.; Sakamoto, H., *Angew. Chem.Int. Ed.*, **2009**, *48*, 1766−1770.
61. Gu, Y.; Wu, Y. N.; Li, L.; Chen, W.; Li, F.; Kitagawa, S., *Angew. Chem. Int. Ed.*, **2017**, *56*, 15658−15662.
62. Félix, G.; Mikolasek, M.; Molnár, G.; Nicolazzi, W.; Bousseksou, A., *Eur. J. Inorg. Chem.*, **2018**, 435−442.

63. Zhao, Z.; Ding, J.; Zhu, R.; Pang, H., *J. Mater. Chem. A*., **2019**, *7*, 15519−15540.

64. Gong, Y.; Yuan, Y.; Chen, C.; Zhang, P.; Wang, J.; Zhuiykov, S.; Chaemchuen, S.; Verpoort, F., *J. Catal.*, **2019**, *371*, 106−115.
65. Luo, Y.; Ahmad, M.; Schug, A.; Tsotsalas, M., *Adv. Mater.*, **2019**, *31*, 1901744**.**
66. Hirai, K.; Furukawa, S.; Kondo, M.; Uehara, H.; Sakata, O.; Kitagawa, S., *Angew. Chem. Int. Ed.*, **2011**, *50*, 8057−8061.
67. Cambi, L.; Cagnasso, A., *Atti. Accad. Naz. Lincei*, **1931**, *13*, 809−813.
68. Miller, J. S.; Gatteschi, D., *Chem. Soc. Rev.*, **2011**, *40*, 3076−3091.
69. Bousseksou, A.; Molnár, G.; Real, J. A.; Tanaka, K., *Coord. Chem. Rev.*, **2007**, *251*, 1822−1833.
70. Gütlich, P.; Garcia, Y.; Goodwin, H. A., *Chem. Soc. Rev.*, **2000**, *29*, 419−427.
71. Gütlich, P.; Hauser, A.; Spiering, H., *Angew. Chem. Int. Ed*., **1994**, *33*, 2024−2054.
72. Halcrow, M. A., *Chem. Soc. Rev.*, **2011**, *40*, 4119−4142.
73. Wang, H. Y.; Ge, J. Y.; Hua, C.; Jiao, C. Q.; Wu, Y.; Leong, C. F.; D'Alessandro, D. M.; Liu, T.; Zuo, J. L., *Angew. Chem. Int. Ed.*, **2017**, *56*, 5465−5470.
74. Cirera, J., *Rev. Inorg. Chem.*, **2014**, *34*.
75. Piñeiro-López, L.; Seredyuk, M.; Muñoz, M. C.; Real, J. A., *Chem. Commun.*, **2014**, *50*, 1833−1835.
76. Ni, Z. P.; Liu, J. L.; Hoque, M. N.; Liu, W.; Li, J. Y.; Chen, Y. C.; Tong, M. L., *Coord. Chem. Rev.*, **2017**, *335*, 28−43.
77. Sciortino, N. F.; Scherl-Gruenwald, K. R.; Chastanet, G.; Halder, G. J.; Chapman, K. W.; Létard, J. F.; Kepert, C. J., *Angew. Chem. Int. Ed.*, **2012**, *124*, 10301−10305.
78. Kitazawa, T.; Gomi, Y.; Takahashi, M.; Takeda, M.; Enomoto, M.; Miyazaki, A.; Enoki, T., *J. Mater. Chem.*, **1996**, *6*, 119−121.
79. Niel, V.; Martinez-Agudo, J. M.; Muñoz, M. C.; Gaspar, A. B.; Real, J. A., *Inorg. Chem.*, **2001**, *40*, 338−3839.
80. Murray, K. S.; Kepert, C. J., Spin Crossover Transition Metal Compunds, **2012**, 195−228.
81. Yoshida, Y.; Inoue, K.; Kikuchi, K.; Kurmoo, M., *Chem. Mater.*, **2016**, *28*, 7029−7038.
82. Ohba, M.; Yoneda, K.; Agusti, G.; Muñoz, M. C.; Gaspar, A. B.; Real, J. A.; Yamasaki, M.; Ando, H.; Nakao, Y.; Sakaki, S., Angew. Chem. Int. Ed., 2009, 48, 4767−4771.
83. Deshmukh, M. M.; Ohba, M.; Kitagawa, S.; Sakaki, S., *J. Am. Chem. Soc.*, **2013**, *135*, 4840−4849.

84. Ando, H.; Nakao, Y.; Sato, H.; Ohba, M.; Kitagawa, S.; Sakaki, S., *Chem. Phys. Lett.*, **2011**, *511*, 399−404.
85. Arcís-Castillo, Z.; Muñoz-Lara, F. J.; Muñoz, M. C.; Aravena, D.; Gaspar, A. B.; Sánchez-Royo, J. F.; Ruiz, E.; Ohba, M.; Matsuda, R.; Kitagawa, S., *Inorg. Chem.*, **2013**, *52*, 12777−12783.
86. Ohtani, R.; Yoneda, K.; Furukawa, S.; Horike, N.; Kitagawa, S.; Gaspar, A. B.; Muñoz, M. C.; Real, J. A.; Ohba, M., *J. Am. Chem. Soc.*, **2011**, *133*, 8600−8605.

Chapter 1

Modulation of Spin Transition Behavior by Designing Pore Space trough the Mixed-metal Approach

Abstract

Almost all studied guest molecules provide the same effect on the spin state of 3D Hofmann-type MOF {Fe(pz)[M(CN)$_4$]} (pz = pyrazine, M = Pt (**1**) Pd (**2**)) regardless of the difference open metal sites (OMS): Pt or Pd.[1,2,3] However, when iodine is used as a guest molecule, **1** and **2** show quite different ST behaviour depending on the OMSs. In the case of **1**, iodine coordinates to Pt^{IV} centres as I^-, and gives a mixed-valence {Fe(pz)[$Pt^{II/IV}$(CN)$_4$(I)$_n$]} (**1_I**, n = 0.0-1.0).[4,5] The ST temperature of **1_I** is linearly raised to 398 K (n = 1.0) with increasing the iodine content. On the other hand, for **2**, iodine is confined as I_2 molecules between two Pd centres and forms a clathrate {Fe(pz)[Pd(CN)$_4$]·0.95I_2} (**2_I**). It exhibits ST with a wide hysteresis of 94 K through the order-disorder transition of the confined I_2 molecules. To modulate both high T_C^{up} and wide hysteresis, six types of solid solution {Fe(pz)[Pt_xPd_{1-x}(CN)$_4$]} (**3*x***) were prepared. The magnetic behaviour of iodine-containing **3*x*_I** changed depending on x value, however, it controlled mainly by **1_I** component. The wide hysteresis was observed only when x value was tiny. These results well reflected the different interactions of OMSs to iodine. In the case of **1**, iodine forms I–Pt^{IV}–I bonds irreversibly, on the other hand **2** forms a clathrate with confining I_2 molecule between two Pd sites. In other words, a vertical queue of two Pd sites is necessary to confine I_2 molecule. In the competition for interacting with iodine, Pt site that forms irreversible bond is more advantageous clearly. In the case **3*x***, Pt^{II} sites form I–Pt^{IV}–I bonds preferentially, and the generated I–Pt^{IV}–I sites disturb confinement of I_2 between Pd sites, which is an undesirable situation to obtain wide hysteresis. To obtain both high T_C^{up} and wide hysteresis at the same time, it is essential to achieve both the formation of I–Pt^{IV}–I bonds and the confinement of I_2 in acceptable balance. The small x value (< 0.2) gave a sufficiently diluted Pt site distribution, which successfully brought out high T_C^{up} and wide hysteresis with increasing the number of confined I_2 molecules.

Introduction

Recently, MOFs are one of the promising porous materials for gas storage[6,7] or separation[8,9], heterogeneous catalysis[10,11], sensing[12,13,14] and other applications[15,16,17,18] because MOFs have a potential to be platform combining porous properties and physical properties such as magnetic, electrical[19,20,21] and optical properties.[18] In this work, the author focused on magnetic behaviours, especially, spin crossover (SCO) phenomena in MOFs.[22,23] Spin crossover (SCO) compounds have attached much attention from not only fundamental studies but also their potential applications such as display, memory, and switching devices.[24,25,26] To grow up SCO compounds to these applications, it is necessary to control SCO behaviour.[27] For example, a large thermal hysteresis around RT is needed to save memories safely. To obtain a hysteresis behaviour, long-range elastic interaction between metal centres which has a change of spin state is important, which means the concentration of spin-changing metal centres is related to the magnetic behaviour.[28,29] The metal dilution approach has been investigated to obvious the elastic interaction.[30] In the research filed of Hofmann-type MOFs, there are a few reports about metal dilution.[31] Bousseksou and his co-workers have reported about the metal dilution effect on 3D Hofmann-type MOFs $\{M(pz)[Pt(CN)_4]\}$ (M = Ni or Co, $0 \leq x \leq 1$).[32] Usually, the metal dilution effect can be observed the spin equilibrium temperature (T_{eq}, defined as the temperature for which $G_{HS} - G_{LS} = 0$) and the SCO behaviour becomes more gradual, and the hysteresis width decreases and vanishes finally with increasing dilution. For 3D Hofmann-type MOFs, both Ni and Co dilution decrease the hysteresis width and smooth the transition curves depending on the x value. Here, the metal dilution approach can be considered as the mixed-metal approach. Controlling the x value, magnetic behaviour can be modulated, on-demand, however, dilution of spin-changing metal centres brings out a decrease of hysteresis width. Therefore, the author attempted to modulate the magnetic behaviour including the spin transition (ST) temperature and thermal hysteresis width in 3D Hofmann-type MOFs $\{Fe^{II}(pz)[M^{II}(CN)_4]\}$ (pz = pyrazine, M = Pt (**1**), Pd (**2**)) by mixed-metal approach using two kinds of OMS: Pt and Pd not dilution of spin-changing metal centre Fe. There are two reasons why the combination of Pt and Pd was selected; (i) solid solutions will be formed easily because **1** and **2** have similar lattice parameters; (ii) guest-free compound **1** and **2** show the $^1A_1 \rightleftarrows {}^5T_2$ spin ST behaviour with thermal hysteresis (T_C^{up} = 304 K, T_C^{down} = 284 K)[33] but iodine-containing **1** and **2** show quite different magnetic behaviours although most of the studied guest molecules bring out same effects on both **1** and **2** regardless of the OMSs difference.

In the case of **1**, iodine coordinated to Pt^{IV} centres as iodine anion (I^-) and formed a mixed-valence $\{Fe(pz)[Pt^{II/IV}(CN)_4(I)_n]\}$ (n = 0.0−1.0) (**1_I**).[5,4] In the

framework, the Pt^{II} and I–Pt^{IV}–I sites alternatively arranged because of the steric limit. The ST temperature increased up to 398 K (n = 1.0) with increasing iodine content (n), because the strong π-donor capability of iodide enhanced the σ-donor capability of cyano-nitrogen through Pt^{IV}, and increased ligand field strength around Fe^{II}, which derived stabilization of the LS state. In addition, the ST temperature changes between 304 K (n = 0.0) and 398 K (n = 1.0) depending on iodine content (n). Interestingly, the iodine content (n) can be controlled by the SBH (solid-state blending and heating) method in which solid-state guest-free **1** and iodine adduct **1_I** are ground together and heated up to ST temperatures T_C^{up}. In general, a decrease of guest molecules provides heterogeneous state and magnetic behaviour originated in the guest-free state are observed. However, in the case of **1_I**, ST temperature T_C^{up} increased with keeping a hysteresis width and cooperativity. These results demonstrated that iodine which coordinate to Pt^{IV} sites migrates from **1_I** to guest-free **1** triggered by the ST and formed a homogeneous solid-state. On the other hand, for **2**, iodine was confined as I_2 molecules in the pores, and it formed a clathrate $\{Fe(pz)[Pd(CN)_4]\cdot 0.95I_2\}$ (**2_I**). In large pores of HS state, I_2 behaves as a disordered monomer and preventing shrinkage of the framework. On the other hand, in small pores of LS state, the host-guest interactions among I_2 molecules and Pd, pz form an ordered arrangement of I_2 and contribute to further stabilization of the LS state. This order-disorder transition of I_2 molecules in the pore gives a wide hysteresis of 94 K in ST behaviour. From these results, the solid solutions $\{Fe^{II}(pz)[Pt_xPd_{1-x}(CN)_4]\}$ (**3*x***) are expected to modulate both ST temperature T_C^{up} and hysteresis width depending on the x value. In this work, six types of solid solutions having different Pt content; x were prepared. The ST temperature T_C^{up} of iodine-containing solid solutions **3*x*_I** increased with increasing the Pt content (x) because the LS state was stabilized with forming I–Pt^{IV}–I bonds. On the other hand, the hysteresis expanded only when the x value was quite small. The correlation between x value and ST behaviours was discussed in terms of the arrangement of OMSs in solid solutions.

Experiments

1. Physical Measurements

All compounds were characterized using infrared (IR) spectroscopy, Raman spectroscopy, thermogravimetric analysis (TGA), and powder X-ray diffraction (PXRD). Elemental analysis of carbon, hydrogen and nitrogen was carried out by the staff of technical support division Kyushu University. The ratio of Pt and Pd in solid solutions were estimated by X-ray fluorescence analysis measurements. Shimazu Rayny EDX-800HS2 X-ray fluorescence spectrophotometer at room temperature was used as a X-ray fluorescence analysis measurements. The crystal size was evaluated by scanning electron microscopy (SEM, Zeiss ULTRA55) analysis. The dispersion of Pt and Pd in solid solutions was confirmed by elemental mapping using SEM-EDX (SEM-energy dispersive X-ray spectrometry, Zeiss ULTRA55, with 10.00 kV accelerating voltage). IR spectra were recorded with a JASCO FT/IR-4200 spectrophotometer. Raman spectra were recorded with a Jasco NRS-1000. For temperature dependence Raman spectra, the sample stage Model S84_C from S.T. japan Inc. were attached. The excitation source was a 632 nm He-Ne laser and the laser power were carefully kept low to avoid local heating during laser irradiation. TGA was carried out with a Perkin ElmerSTA6000 from 303 to 973 K temperature range under nitrogen atmosphere (heating rate: 5 K min^{-1}). Rigaku Ultima IV spectrometer were used in PXRD measurement using a reflection-free sample holder, and graphite-monochromated Cu K_{α} radiation was set. Magnetic susceptibilities of the ground samples were recorded using Quantum Design MPMS-XL5R SQUID with the temperature range from 2 to 400 K in an applied dc magnetic field of 1000 Oe. A gelatin capsule and a plastic straw were used to fix samples on the end of the sample transport rod. The molar magnetic susceptibility, χM, was corrected for diamagnetism of the constituent atoms and that of the sample tube.

2. Materials

All chemicals purchased were of reagent grade and used without further purification.

3. Preparation of Compounds

3-1. Guest-free solid solutions

The solid solutions were prepared according to the literature method for synthesis of **1** and **2**. $Fe^{II}(NH_4)_2(SO_4)_2 \cdot 6H_2O$ (0.2553 g, 0.651 mmol), antioxidant ascorbic acid and pz (0.1041 g, 1.30 mmol) were dissolved in degassed water (100 mL). A solution including $K_2[Pt(CN)_4] \cdot 3H_2O$ and $K_2[Pd(CN)_4] \cdot 3H_2O$ (total: 0.651mmol) at an arbitrary ratio (at preparation x = 0 (**2**), 0.5, 0.2, 0.1, 0.075, 0.05, 0.025, 1 (**1**)) in degassed methanol (50 mL) and water (50 mL) added to the solution under nitrogen at room temperature. After stirring overnight, the yellow precipitation was collected by suction filtration, washed with water and methanol, and dried under ambient pressure. After heating at 393 K overnight, guest-free solid was obtained.

3-2. Iodine-containing solid solutions

Iodine-containing solid solutions **3*x*_I** were prepared by exposing the solid solutions to iodine vapour at room temperature overnight. The colour of samples became black from yellow (**Figure 1-1**). Before iodine adsorption, guest-free solid solutions were activated at 393 K for 6 hours.

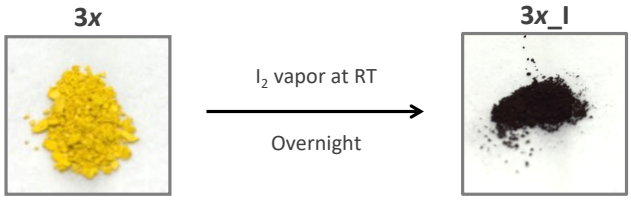

Figure 1-1. Colour change from guest-free **3*x*** (yellow) to iodine-containing **3*x*_I** (black).

Results and Discussion

1. Characterizations of Guest-free Solid Solutions

1-1. XRF measurement

XRF measurement of solid solutions **3*x*** (x = 0.55, 0.26, 0.11, 0.085, 0.057, 0.030) were recorded using Shimazu Rayny EDX-800HS2 X-ray fluorescence spectrometer with calibration curve method in order to confirm the metal ratio in the solid solution. The found metal rate of solid solutions showed almost same with the preparation ratio of $K_2[Pt(CN)_4]$ and $K_2[Pd(CN)_4]$. (at the preparation: x = 0.5, 0.2, 0.1, 0.075, 0.05, 0.025).

Table 1-1. The Pt content (x value) in solid solutions **3*x*** at the preparation and calculated by XRF measurement.

Pt content in preparation / %	*x* value	Pt content in preparation / %	*x* value
50	0.55	7.5	0.085
20	0.26	5	0.057
10	0.11	2.5	0.030

1-2. SEM-EDX

SEM (scanning electron microscopy) analysis of the solid solutions **3*x*** was performed using a Zeiss ULTRA55 (10.00 kV accelerating voltage). For this measurement, powder samples were pasted on the carbon tape. To observe particle size of samples, the magnitude was determined as 2500X for SEM analysis. To observe the dispersion of Pt and Pd in solid solutions **3*x*** and force on the single crystal, the magnitude was decided as 9220X. **Figure 1-2** shows the SEM images of **3*x***, however, the distribution of crystal size have not been calculated. **Figure 1-3** shows the SEM image which forced on single crystal and elemental mapping measured by SEM-EDX (SEM-energy dispersive X-ray spectrometry). The size of prepared solid solutions was around 2 μm and the dispersion of Pt (colour: pink) and Pd (colour: light blue) was observed by the elemental mapping.

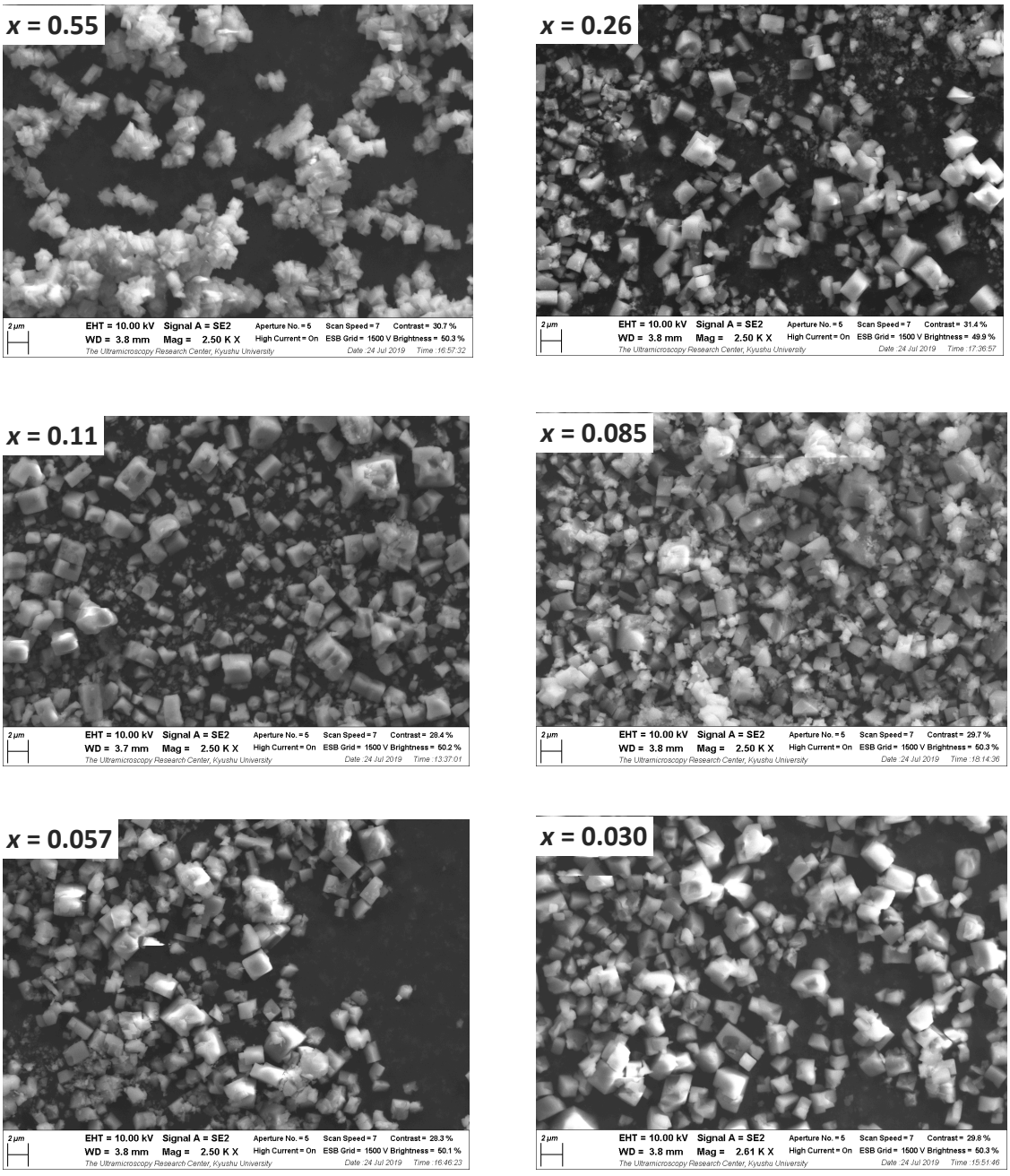

Figure 1-2. SEM images of solid solutions **3*x***. The accelerating voltage was 10.00 kV. The magnitude was 2.50 KX.

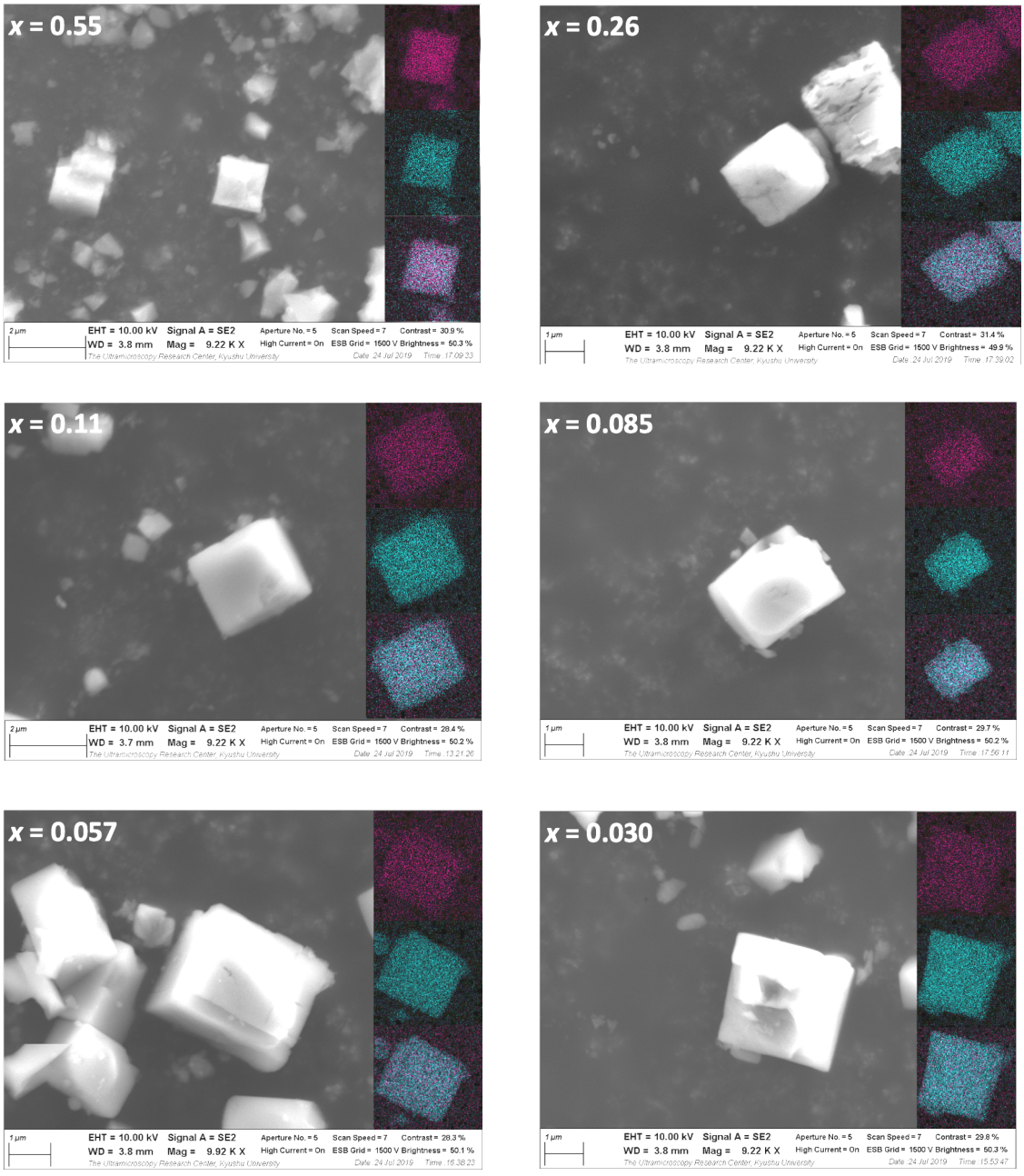

Figure 1-3. SEM-EDX images of solid solutions **3*x***. The accelerating voltage was 10.00 kV, and the magnitude was 9.92 KX. Pt, pink; Pd, blue.

1-3. IR and Raman Spectra

The infrared (IR) spectra of these compounds exhibit ν(C≡N) modes around 2200cm^{-1} and pyrazine internal modes between 600 and 1600 cm^{-1}. The lower frequency modes originated from metal-ligand vibrations. In the previous work shows the ν(C≡N) modes of **1** and **2** in HS state, 2172 cm^{-1} and 2175 cm^{-1} respectively by IR spectroscopy.[34] From IR spectra of solid solutions, the ν(C≡N) modes around 2200cm^{-1} were shifted depending on the ratio of Pt and Pd (**Figure 1-4**). This result indicates that the Pt and Pd sites are distributed in prepared solid solutions and agree with elemental mapping. By the Raman microscopy measurement, the spin state of solid solutions was identified. The most obvious peak shift by the spin transition is in-plane bending mode of pyrazine ring, which exhibits a shift from 645 to 675 cm^{-1}.[34,35]

The Raman spectra showed ν(C≡N) modes around 2200cm^{-1} and pyrazine internal modes between 600 and 1600 cm^{-1} as well as IR spectra. To confirm the spin transition, Raman spectra were measured at RT and 250 K, 340 K respectively, and the peak shift with the spin transition was observed (**Figure 1-5**). Comparing with 250 K and 340 K, the solid solution was high spin state at RT.

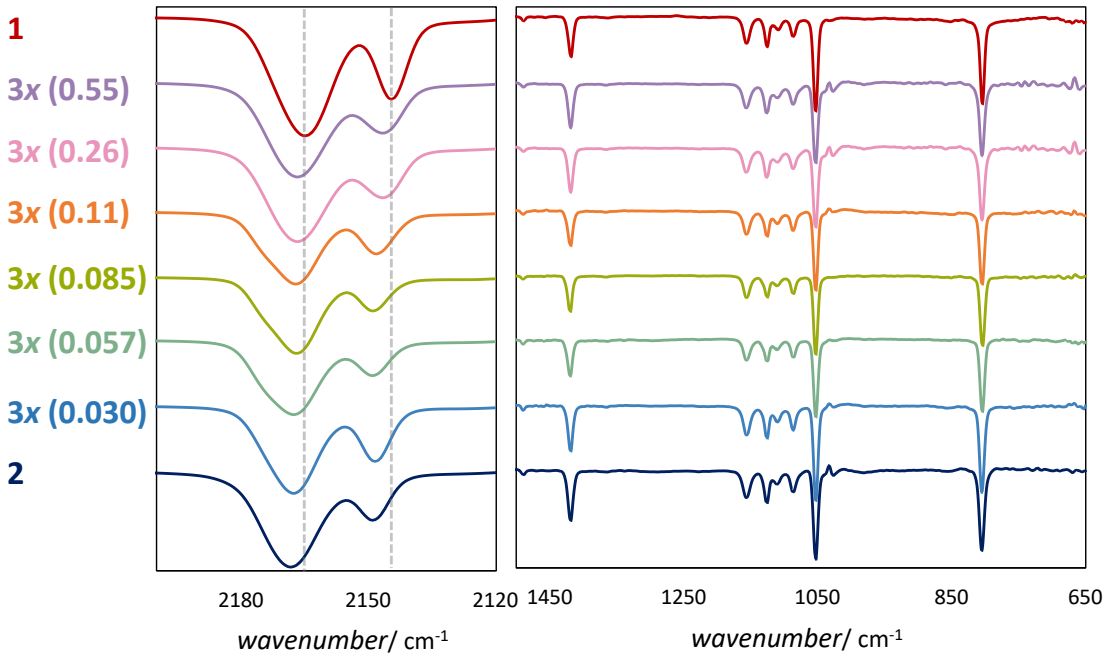

Figure 1-4. IR spectra of guest-free **1**, **2** and **3*x*** at RT.

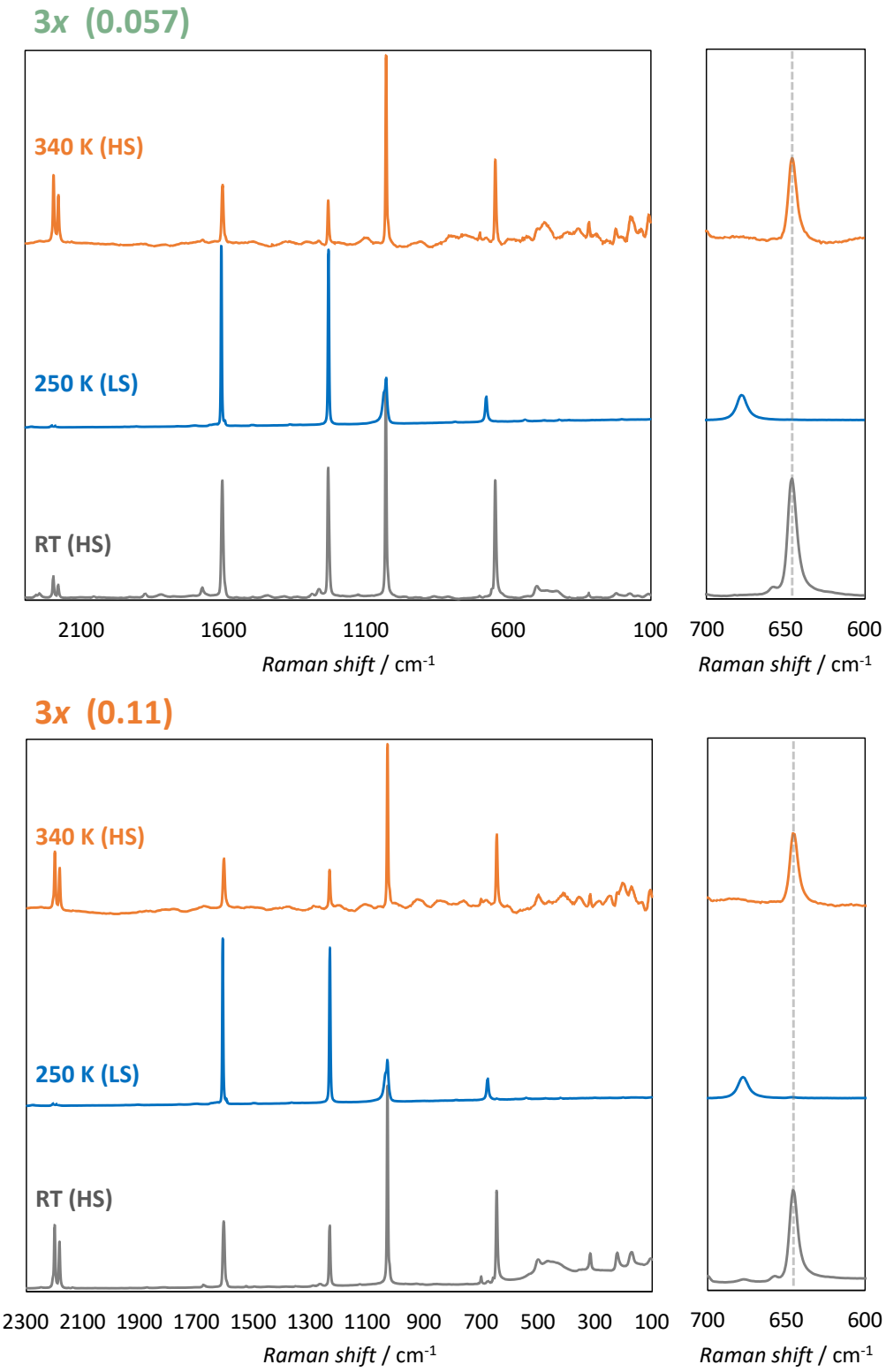

Figure 1-5. Raman spectra of **3*x* (0.057)** and **3*x* (0.11)** at 340 K, 250 K and RT.

1-4.PXRD patterns

Compound **1** and **2** were crystallized in the tetragonal space group *P*4/*mmm* in the LS and HS states, and I could characterize the spin state at RT from PXRD experiments. The lattice parameters in the HS and LS states were $a = b = 7.457(4)$, $c = 7.259(4)$ Å and V = 403.6(4) Å^3, and $a = b = 7.184(6)$, $c = 6.783(5)$ Å and V = 350.1(5) Å^3, respectively. The simulated pattern was obtained from the single crystal structure in the HS state from previous work. The PXRD patterns indicated all guest-free solid solutions **3*x*** had similar structure with **1** and **2**, and these patterns and yellow colour of samples indicated HS state at RT (**Figure 1-6**).[2] According to Vegard's law the lattice parameters of solid solutions have a relationship with the ratio of pure solid.[36,37] However, in this system, the shift of diffraction peaks was not observed because **1** and **2** had quite similar lattice parameter (**Figure 1-7**). In some reports, this phenomenon was observed in spite of the mixed-metal MOFs.[38,39]

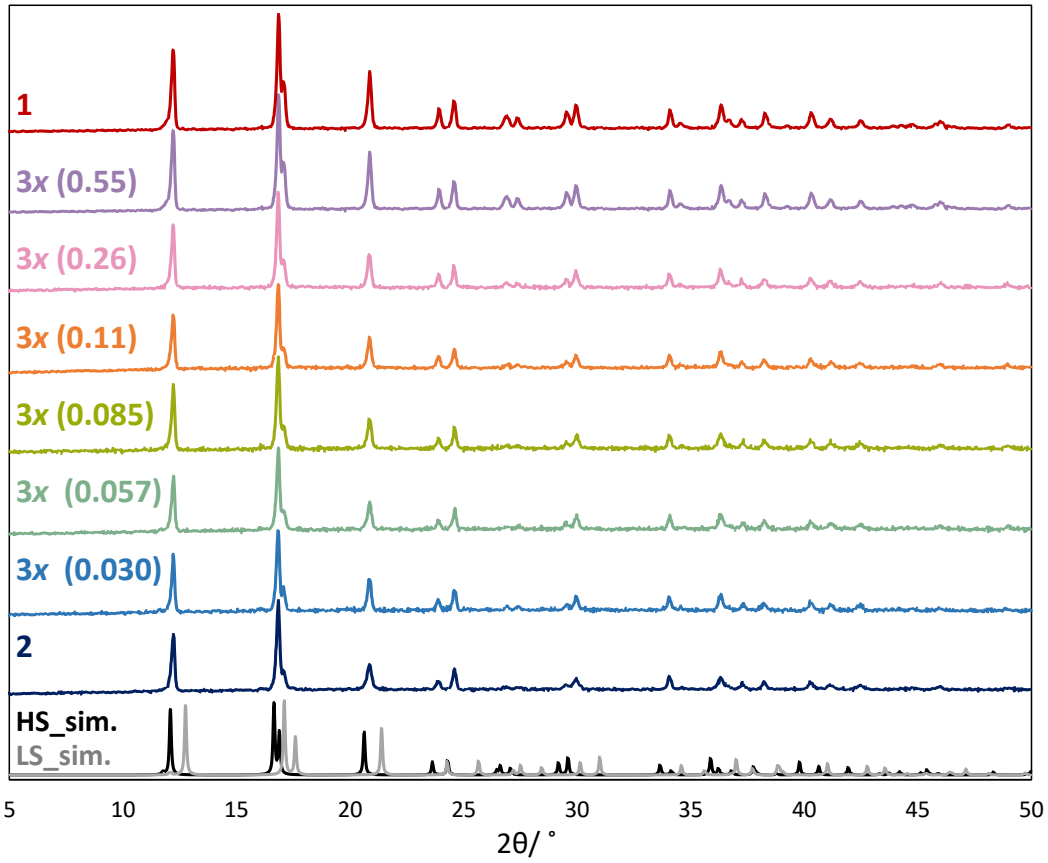

Figure 1-6. PXRD patterns of guest-free **1**, **2** and **3*x*** at RT.

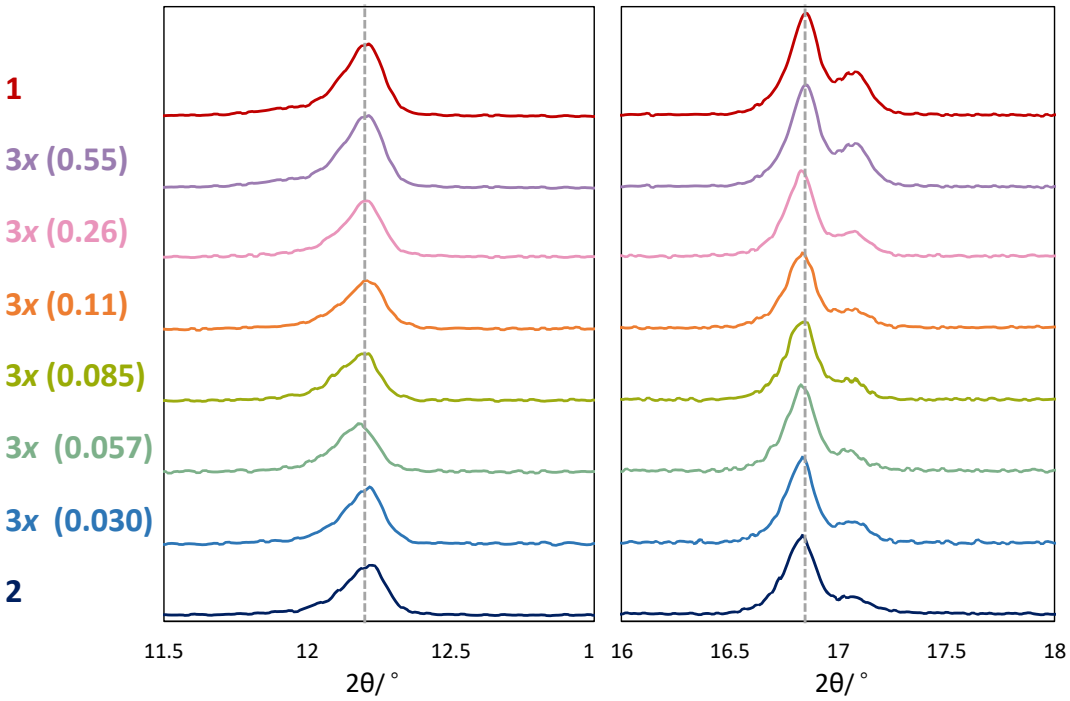

Figure 1-7. PXRD patterns of guest-free solid solutions **3*x***, **1** and **2** at RT. Left graph shows the diffraction peak that can be indexed as 001. Right graph shows the peak indexed as 110.

1-5. Magnetic Measurement

The magnetic behaviours of guest-free solid solutions **3*x*** shown in **Figure 1-8** and **Table 1-2** in the form of $\chi_M T$ *vs. T*. To avoid the influences of the guest water on magnetic behaviours including ST temperature (T_C), cooperativity of ST and hysteresis width, the magnetic measurements were carried out after dehydration of the samples by heating at 403 K for 6 hours. All solid solutions showed the ST temperature T_C^{up} around 300 K and 20 K hysteresis width, and these behaviours were similar with **1** and **2**.[33] These results agreed with PXRD patterns which indicated solid solutions have same structure in regardless of Pt content (*x* value). Measurements details are shown blow.

Magnetic Behaviour of guest-free 3*x*(0.030)

The variable-temperature magnetic susceptibility measurements were carried out operating at 1000 Oe magnetic field and at temperatures between 240 and 320 K. The spin transition temperature, T_C^{up} and T_C^{down} were evaluated to be 308.5 K and 285.8 K, respectively, therefore the hysteresis width was 22.7 K. The $\chi_M T$ value at 320 K is 3.51 emu K mol^{-1}, which closed to an expected value for the Fe^{II} ion at the HS state. In the cooling process, $\chi_M T$ values continued constant until 285.8 K, and then the value of $\chi_M T$ decreased sharply to 0.407 emu K mol^{-1} at 240 K. This value was larger than a value of the Fe^{II} ion at the LS state.

Magnetic Behaviour of guest-free 3*x*(0.057)

The variable-temperature magnetic susceptibility measurements were carried out operating at 1000 Oe magnetic field and at temperatures between 240 and 320 K. The spin transition temperature, T_C^{up} and T_C^{down} were evaluated to be 304.2 K and 283.8 K, respectively, therefore the hysteresis width was 20.4 K. The $\chi_M T$ value at 320 K is 3.35 emu K mol^{-1}, which closed to an expected value for the Fe^{II} ion at the HS state. In the cooling process, $\chi_M T$ values continued constant until 283.8 K, and then the value of $\chi_M T$ decreased sharply to 0.144 emu K mol^{-1} at 240 K. This value was larger than a value of the Fe^{II} ion at the LS state.

Magnetic Behaviour of guest-free 3*x*(0.085)

The variable-temperature magnetic susceptibility measurements were carried out operating at 1000 Oe magnetic field and at temperatures between 240 and 320 K. The spin transition temperature, T_C^{up} and T_C^{down} were evaluated to be 302.2 K and 285.9 K, respectively, therefore the hysteresis width was 16.3 K. The $\chi_M T$ value at 320 K is 3.55 emu K mol^{-1}, which closed to an expected value for the Fe^{II} ion at the HS state. In the

cooling process, $\chi_M T$ values continued constant until 285.9 K, and then the value of $\chi_M T$ decreased sharply to 0.199 emu K mol^{-1} at 240 K. This value was larger than a value of the Fe^{II} ion at the LS state.

Magnetic Behaviour of guest-free 3*x*(0.11)

The variable-temperature magnetic susceptibility measurements were carried out operating at 1000 Oe magnetic field and at temperatures between 240 and 320 K. The spin transition temperature, T_C^{up} and T_C^{down} were evaluated to be 310.2 K and 287.7 K, respectively, therefore the hysteresis width was 22.5 K. The $\chi_M T$ value at 320 K is 3.72 emu K mol^{-1}, which closed to an expected value for the Fe^{II} ion at the HS state. In the cooling process, $\chi_M T$ values continued constant until 287.7 K, and then the value of $\chi_M T$ decreased sharply to 0.189 emu K mol^{-1} at 240 K. This value was larger than a value of the Fe^{II} ion at the LS state.

Magnetic Behaviour of guest-free 3*x*(0.26)

The variable-temperature magnetic susceptibility measurements were carried out operating at 1000 Oe magnetic field and at temperatures between 240 and 320 K. The spin transition temperature, T_C^{up} and T_C^{down} were evaluated to be 310.3 K and 291.6 K, respectively, therefore the hysteresis width was 18.7 K. The $\chi_M T$ value at 320 K is 3.30 emu K mol^{-1}, which closed to an expected value for the Fe^{II} ion at the HS state. In the cooling process, $\chi_M T$ values continued constant until 291.6 K, and then the value of $\chi_M T$ decreased sharply to 0.144 emu K mol^{-1} at 240 K. This value was larger than a value of the Fe^{II} ion at the LS state.

Magnetic Behaviour of guest-free 3*x*(0.55)

The variable-temperature magnetic susceptibility measurements were carried out operating at 1000 Oe magnetic field and at temperatures between 240 and 320 K. The spin transition temperature, T_C^{up} and T_C^{down} were evaluated to be 302.3 K and 285.7 K, respectively, therefore the hysteresis width was 16.6 K. The $\chi_M T$ value at 320 K is 3.70 emu K mol^{-1}, which closed to an expected value for the Fe^{II} ion at the HS state. In the cooling process, $\chi_M T$ values continued constant until 285.7 K, and then the value of $\chi_M T$ decreased sharply to 0.505 emu K mol^{-1} at 240 K. This value was larger than a value of the Fe^{II} ion at the LS state.

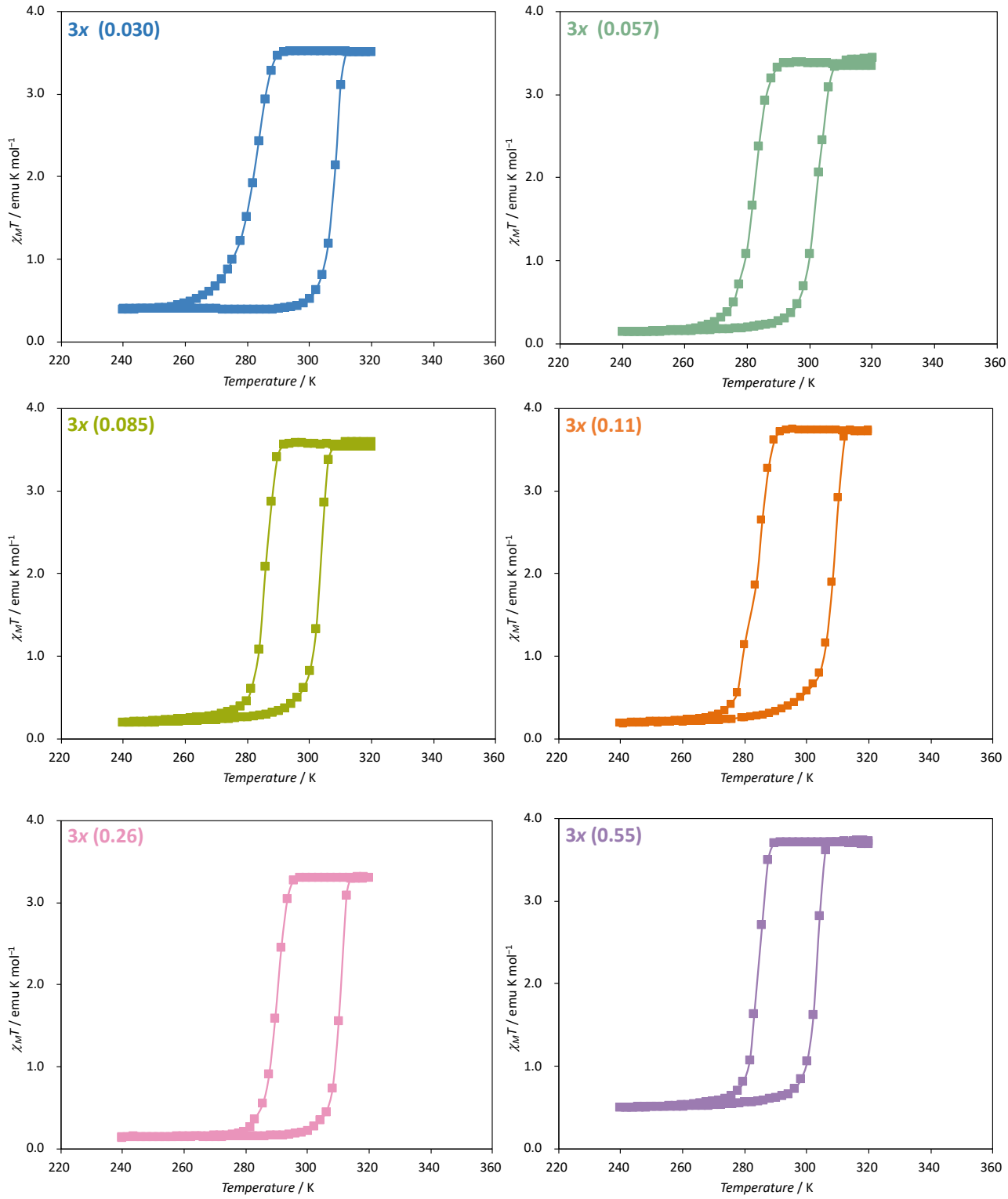

Figure 1-8. Magnetic behaviour of guest-free **3*x***.

Table 1-2. Spin transition temperature and hysteresis width of guest-free **3*x***.

Sample	T_C^{up} / K	T_C^{down} / K	Hysteresis width / K
2	304	284	20
3*x* (0.030)	308.5	285.8	22.7
3*x* (0.057)	304.2	283.8	20.4
3*x* (0.085)	302.2	285.9	16.3
3*x* (0.11)	310.2	287.7	22.5
3*x* (0.26)	310.3	291.6	18.7
3x (0.55)	302.3	285.7	16.6
1[ref4]	304	284	20

2. Characterizations of Iodine-containing Solid Solutions

2-1. TG Analysis

The iodine content in solid solutions were determined using TGA curve (**Figure 1-9**). From previous work about **1_I**, iodine anion (I^-) and pz are removed at same temperature around 500 K, which means iodine forms I–Pt^{IV}–I bonds until the framework is decomposed.[5,4] While for **2_I**, confined I_2 molecule is removed at around 350 K before decomposition of the framework. In the case of solid solutions **3*x*_I**, I_2 molecule between Pd sites was removed firstly, then iodine anion of I–Pt^{IV}–I bonds and pz were removed at higher temperature, as a result, **3*x*_I** showed two steps weight loss. **Table 1-3** shows the summary of iodine content as I not I_2 removed from both Pt sites and Pd sites.

Table 1-3. Iodine content in **3*x*_I**.

Sample	Iodine content as I	Sample	Iodine content as I
3*x*_I(0.55)	0.73	3*x*_I(0.085)	1.69
3*x*_I(0.26)	1.06	3*x*_I(0.057)	1.84
3*x*_I(0.11)	1.35	3*x*_I(0.030)	1.91

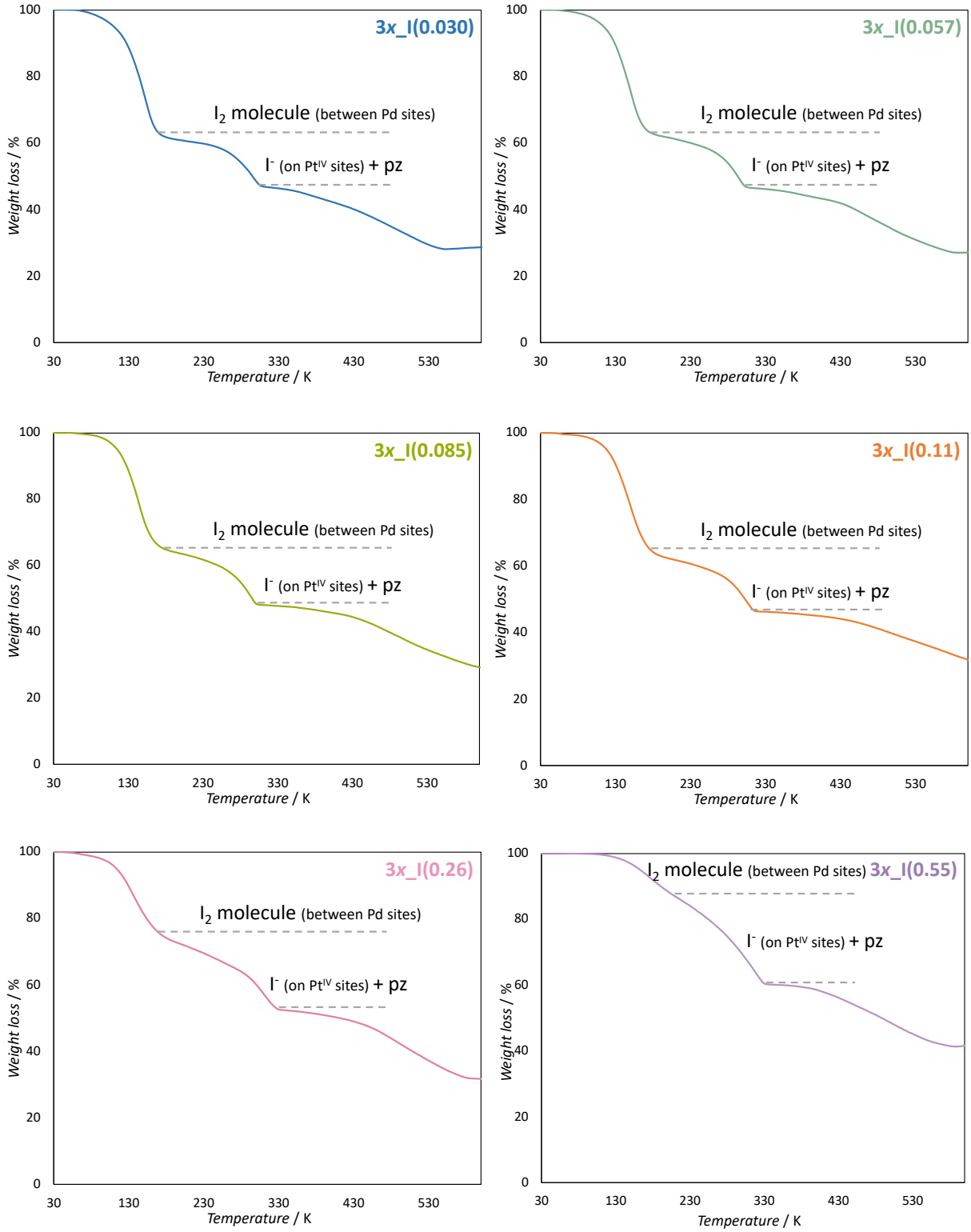

Figure 1-9. TGA curve of iodine-containing **3*x*_I**.

2-2. Raman Spectra

Figure 1-10 shows the Raman spectra of **1_I**, **2_I** and **3*x*_I** at RT. For this measurement, N_2 gas was flowed to the samples for 10 min after exposing iodine vapour overnight. Raman spectra showed not only information about framework but also iodine state in the pore. The ν(C≡N) modes was observed at around 2200cm^{-1} and pyrazine internal modes, between 600 and 1600 cm^{-1}. The lower frequency modes originated from metal-ligand vibrations. From the previous works, I attempted to determine the spin state of iodine-containing solid solutions **3*x*_I** at RT. The most obvious peak shift by the spin transition is in-plane bending mode of pyrazine ring, which exhibits a shift from 645 to 675 cm^{-1}.[34,35] The intensity ratio of ν(ring) modes (at 1230 cm^{-1}) and δ(CH) (at 1605 cm^{-1}) are changed through the ST as well. Considering these previous works, iodine-containing **3*x*_I** ($x \geq 0.085$) were considered the LS state at RT, which means the ST temperature T_C^{up} increased up to higher than RT.

In the case of iodine-containing **1_I,** a very strong Pt-I vibration peak was observed around 130 cm^{-1} (g), and these results agreed with the reported Raman spectra by Ohtani.[4] For iodine-containing **2_I**, there were three kinds of peaks; (i) I_2 monomer at around 170 cm^{-1} (d); (ii) the coupled I_2 motions of the pseudo $I_2\cdots I_2$ dimers (two inclined I_2 molecules interacted though the Pd sites) similar with a strong intermolecular interaction in $I_2\cdots I_2$, which observed in the solid I_2 crystal under high pressure (a); (c); (e); (f), (iii) the intramolecular stretching mode of I_2 monomer (b). In the previous work, type (ii) was observed only in the LS state, and type (iii) was observed only in the HS

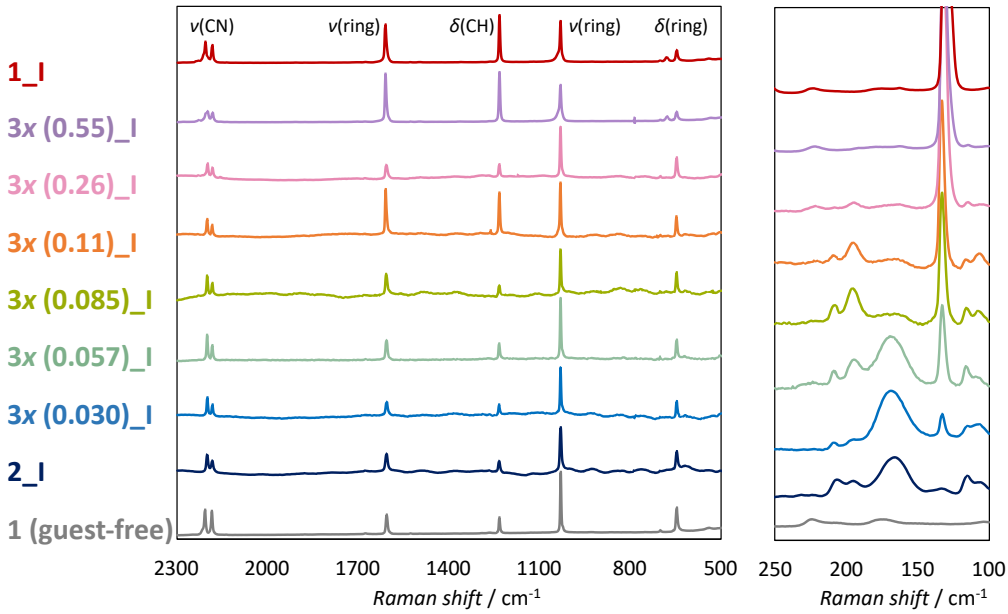

Figure 1-10. Raman spectra of iodine-containing **1_I**, **2_I** and **3*x*_I** at RT.

state. Therefore, the state of I_2 molecules in **2_I** was co nsidered not unified after exposing I_2 vapour at RT, and it is necessary to swing temperature for unify the I_2 molecules behaviours. In the case of iodine-containing **3*x*_I**, a strong peak originated in I-Pt bonds were observed as well as **1_I**. In addition, there were peaks originated from I_2 monomer: type (i), and the coupled I_2 motions of the pseudo $I_2 \cdots I_2$ dimers: type (ii).

Figure 1-11 shows the Raman spectra at 300 K, 180 K (in LS state) and each temperature higher than T_C^{up} (in HS state). Peak (g) originated in I-Pt bonds was observed all solid solutions **3*x*_I** at all temperature. However, peaks originated in I_2 molecules were difficult to recognize, especially, samples which have high Pt content such as **3*x*_I (0.26)** and **3*x*_I (0.55)** at 300 K. This result agreed with the TGA curve. The higher Pt content decrease the Pd continuous arrangement which needed to confine I_2 molecules, and $I–Pt^{IV}–I$ bonds disturb diffusion of I_2 molecules in the pore. As mentioned above, I_2 molecules exhibit the order-disorder transition in the original **2_I**, and the mobility of I_2 molecules are observed by the Raman spectra. In particular, the peaks (ii) corresponded to the coupled I_2 motions of the pseudo $I_2 \cdots I_2$ dimers is a distinctive feature. Similarly, all iodine-containing **3*x*_I** showed type (ii) peaks at 180 K. For this result, I considered confined I2 molecules exhibited the order-disorder transition in the solid solutions **3*x*_I**.

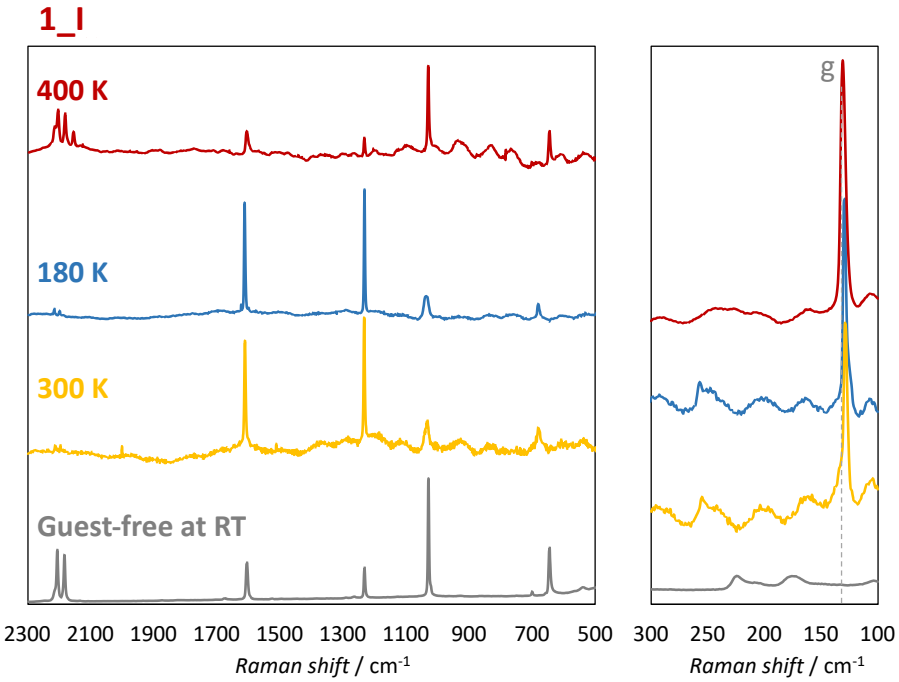
1_I
400 K
180 K
300 K
Guest-free at RT
g
2300 2100 1900 1700 1500 1300 1100 900 700 500
Raman shift / cm-1
300 250 200 150 100
Raman shift / cm-1

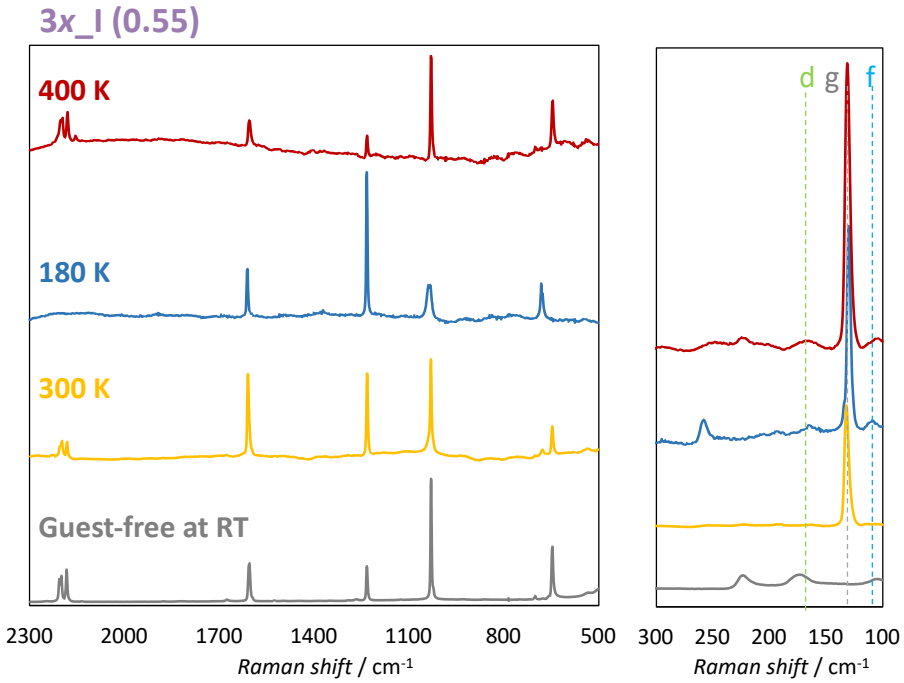
3x_I (0.55)
400 K
180 K
300 K
Guest-free at RT
d g f
2300 2000 1700 1400 1100 800 500
Raman shift / cm-1
300 250 200 150 100
Raman shift / cm-1

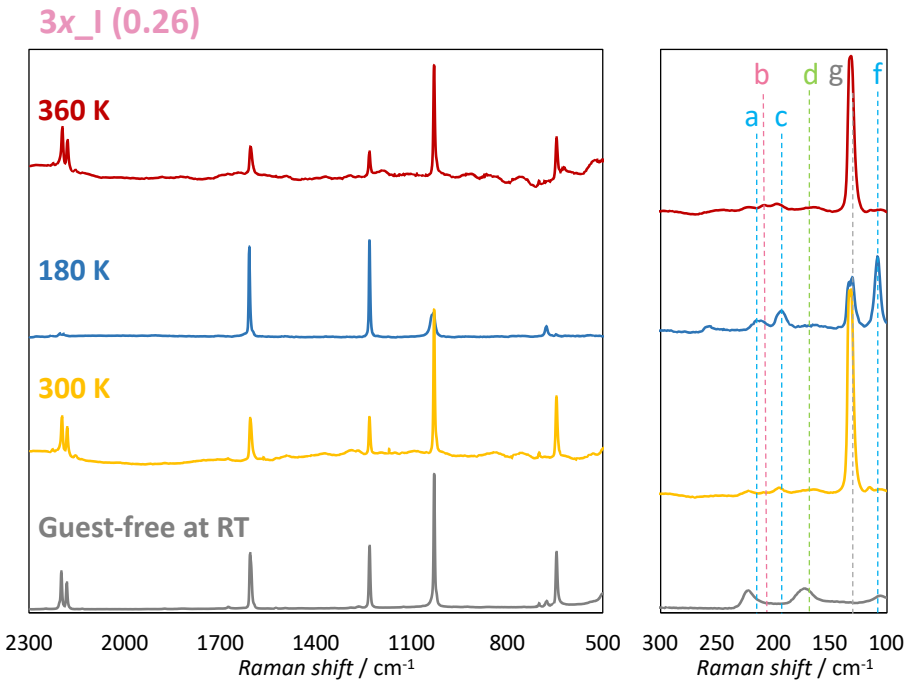
3x_I (0.26)
360 K
180 K
300 K
Guest-free at RT
2300 2000 1700 1400 1100 800 500
Raman shift / cm-1
a b c d g f
300 250 200 150 100
Raman shift / cm-1

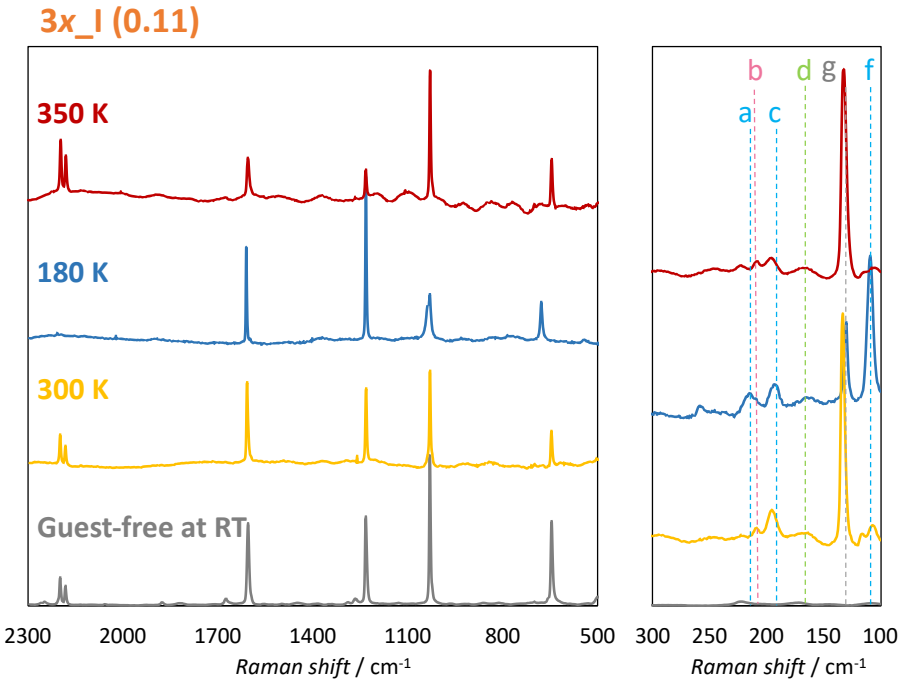
3x_I (0.11)
350 K
180 K
300 K
Guest-free at RT
2300 2000 1700 1400 1100 800 500
Raman shift / cm-1
a b c d g f
300 250 200 150 100
Raman shift / cm-1

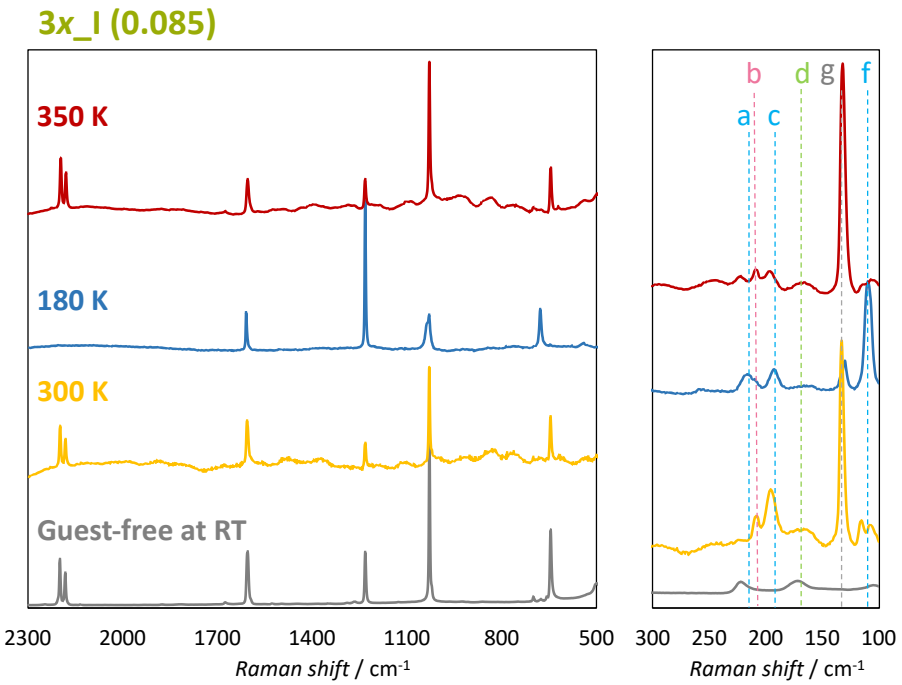
3x_I (0.085)
350 K
180 K
300 K
Guest-free at RT
2300 2000 1700 1400 1100 800 500
Raman shift / cm-1
b d g f
a c
300 250 200 150 100
Raman shift / cm-1

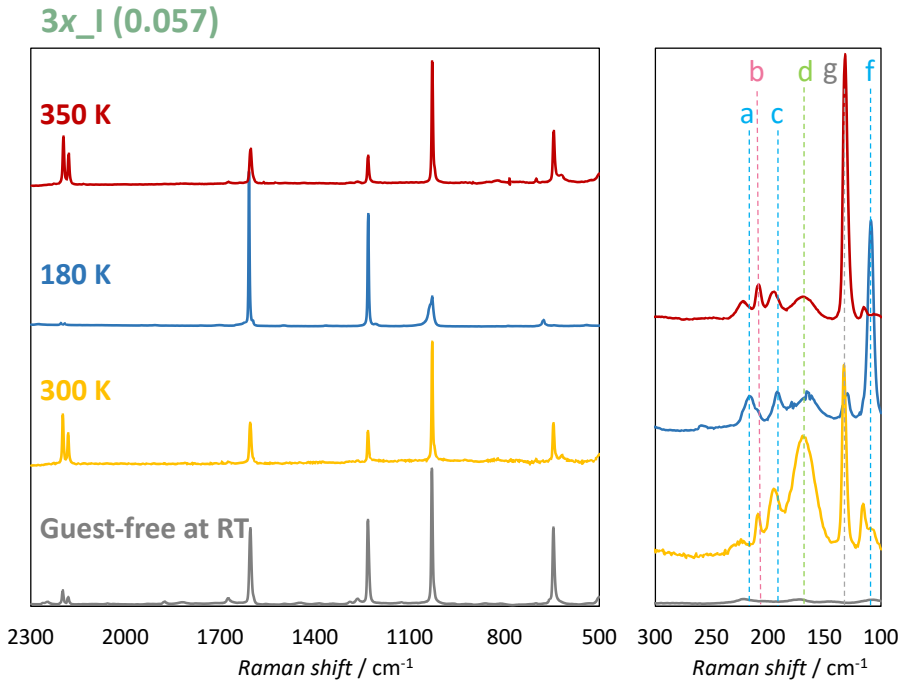
3x_I (0.057)
350 K
180 K
300 K
Guest-free at RT
2300 2000 1700 1400 1100 800 500
Raman shift / cm-1
b d g f
a c
300 250 200 150 100
Raman shift / cm-1

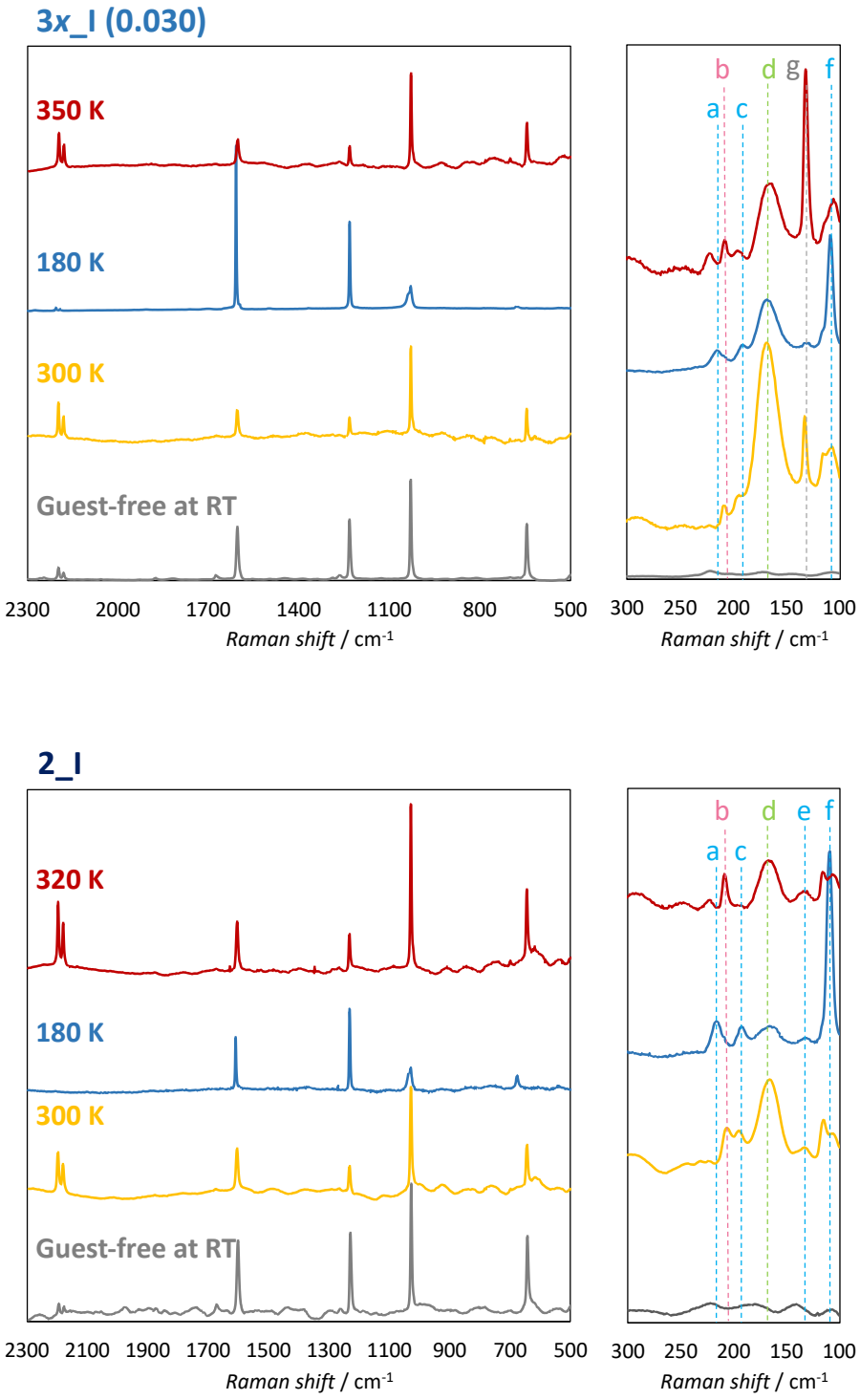

Figure 1-11. Raman spectra of iodine-containing **3*x*_I** at 180 K, 300 K and at the higher than each spin transition temperature T_C^{up}.

2-3. PXRD Patterns

In the case of guest-free solid solutions, the PXRD patterns indicated all samples had similar structure and same spin state, HS state. However, the PXRD patterns of iodine-containing solid solutions **3*x*_I** showed different patterns, in particular **3*x*_I** ($x \geq 0.085$) had similar patterns with the simulation of **1_I** at LS state, which means, these **3*x*_I** ($x \geq 0.085$) were LS state at RT, and the ST temperature T_C^{up} increased comparing with guest-free **3*x*** (**Figure 1-12**). The broad peaks in the lower *x* content samples such as **3*x*_I(0.030)**, **3*x*_I(0.057)** were considered the effect of I_2 molecules disorder which observed as well in **2_I** at the HS state.

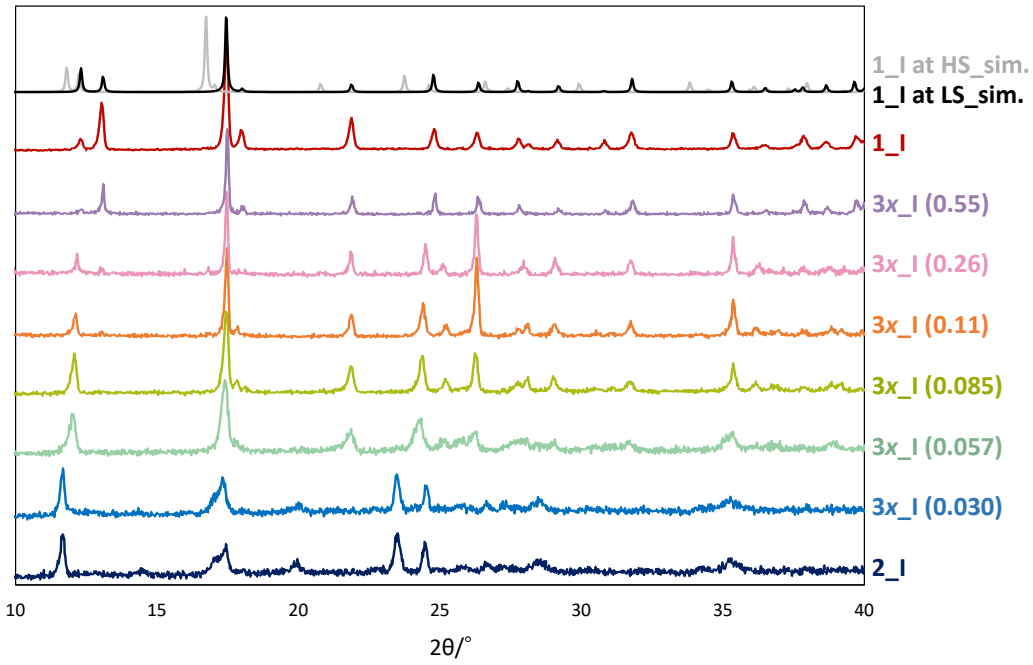

Figure 1-12. PXRD patterns of iodine-containing **1_I**, **2_I** and **3*x*_I** at RT.

2-4. Magnetic Measurement of Solid Solutions

The magnetic behaviours of iodine-containing solid solutions **3*x*** are shown in the form of $\chi_M T$ *vs.* T (**Figure 1-13**). To avoid adsorption water, iodine-containing solid solutions (**3*x*_I**) were stuffed with the gelatin capsule as soon as possible after exposing iodine vapour. The ST temperature T_C^{up} increased, in other word, LS state was stabilized with increasing x value. While, the thermal hysteresis width decreased with increasing x value, and a wide hysteresis was provided only when x value was tiny. **Figure 1-15** shows the correlation between ST temperature and x value. This graph indicated the increasing rate of T_C^{up} was drastically changed above and below $x = 0.1$. For the hysteresis, when x value was over 0.1, they had 20 K thermal hysteresis as with guest-free, on the other hand, the hysteresis expanded when x was less than 0.1. Therefore, only when x value was less than 0.1, both T_C^{up} and hysteresis width increased. Measurements details are shown blow.

If these prepared solid solutions have a large domain as the solid mixture (**1_I** : **2_I** = 1 : 1), it will show two-steps spin crossover phenomenon, and each step originated in **1_I** or **2_I**. To compare with the solid mixture, I simulated the magnetic behaviour of the solid mixture using the magnetic measurements results of **1_I** and **2_I** (**Figure 1-14)**. Comparing with simulated magnetic behaviour of solid mixture, all **3*x*_I** showed a single step spin crossover phenomenon. Which means, Pt and Pd sites disperse in prepared solid solutions unlike solid mixture.

Magnetic Behaviour of 3*x*_I(0.030)

The variable-temperature magnetic susceptibility measurements were carried out operating at 1000 Oe magnetic field and at temperatures between 180 and 360 K. The spin transition temperature, T_C^{up} and T_C^{down} were evaluated to be 320 K and 240 K, respectively, therefore the hysteresis width was 80 K. The $\chi_M T$ value at 360 K is 3.52 emu K mol^{-1}, which closed to an expected value for the Fe^{II} ion at the HS state. In the cooling process, $\chi_M T$ values continued constant until 240 K, and then the value of $\chi_M T$ decreased sharply to 0.293 emu K mol^{-1} at 180 K. This value was larger than a value of the Fe^{II} ion at the LS state.

Magnetic Behaviour of 3*x*_I(0.057)

The variable-temperature magnetic susceptibility measurements were carried out operating at 1000 Oe magnetic field and at temperatures between 180 and 360 K. The spin transition temperature, T_C^{up} and T_C^{down} were evaluated to be 328 K and 267 K, respectively, therefore the hysteresis width was 61 K. The $\chi_M T$ value at 360 K is 3.58 emu K mol^{-1}, which closed to an expected value for the Fe^{II} ion at the HS state. In the cooling

process, $\chi_M T$ values continued constant until 267 K, and then the value of $\chi_M T$ decreased sharply to 0.183 emu K mol^{-1} at 180 K. This value was larger than a value of the Fe^{II} ion at the LS state.

Magnetic Behaviour of 3*x*_I(0.085)

The variable-temperature magnetic susceptibility measurements were carried out operating at 1000 Oe magnetic field and at temperatures between 180 and 360 K. The spin transition temperature, T_C^{up} and T_C^{down} were evaluated to be 334 K and 289 K, respectively, therefore the hysteresis width was 45 K. The $\chi_M T$ value at 360 K is 3.58 emu K mol^{-1}, which closed to an expected value for the Fe^{II} ion at the HS state. In the cooling process, $\chi_M T$ values continued constant until 289 K, and then the value of $\chi_M T$ decreased sharply to 0.180 emu K mol^{-1} at 180 K. This value was larger than a value of the Fe^{II} ion at the LS state.

Magnetic Behaviour of 3*x*_I(0.11)

The variable-temperature magnetic susceptibility measurements were carried out operating at 1000 Oe magnetic field and at temperatures between 200 and 380 K. The spin transition temperature, T_C^{up} and T_C^{down} were evaluated to be 340 K and 315 K, respectively, therefore the hysteresis width was 25 K. The $\chi_M T$ value at 380 K is 3.55 emu K mol^{-1}, which closed to an expected value for the Fe^{II} ion at the HS state. In the cooling process, $\chi_M T$ values continued constant until 315 K, and then the value of $\chi_M T$ decreased sharply to 0.238 emu K mol^{-1} at 200 K. This value was larger than a value of the Fe^{II} ion at the LS state.

Magnetic Behaviour of 3*x*_I(0.26)

The variable-temperature magnetic susceptibility measurements were carried out operating at 1000 Oe magnetic field and at temperatures between 200 and 380 K. The spin transition temperature, T_C^{up} and T_C^{down} were evaluated to be 352 K and 331 K, respectively, therefore the hysteresis width was 21 K. The $\chi_M T$ value at 380 K is 3.55 emu K mol^{-1}, which closed to an expected value for the Fe^{II} ion at the HS state. In the cooling process, $\chi_M T$ values continued constant until 331 K, and then the value of $\chi_M T$ decreased sharply to 0.175 emu K mol^{-1} at 200 K. This value was larger than a value of the Fe^{II} ion at the LS state.

Magnetic Behaviour of 3*x*_I(0.55)

The variable-temperature magnetic susceptibility measurements were carried out operating at 1000 Oe magnetic field and at temperatures between 180 and 400 K. The spin transition temperature, T_C^{up} and T_C^{down} were evaluated to be 365 K and 349 K, respectively, therefore the hysteresis width was 16 K. The $\chi_M T$ value at 400 K is 3.51 emu K mol^{-1}, which closed to an expected value for the Fe^{II} ion at the HS state. In the cooling process, $\chi_M T$ values continued constant until 349 K, and then the value of $\chi_M T$ decreased sharply to 0.175 emu K mol^{-1} at 180 K. This value was larger than a value of the Fe^{II} ion at the LS state.

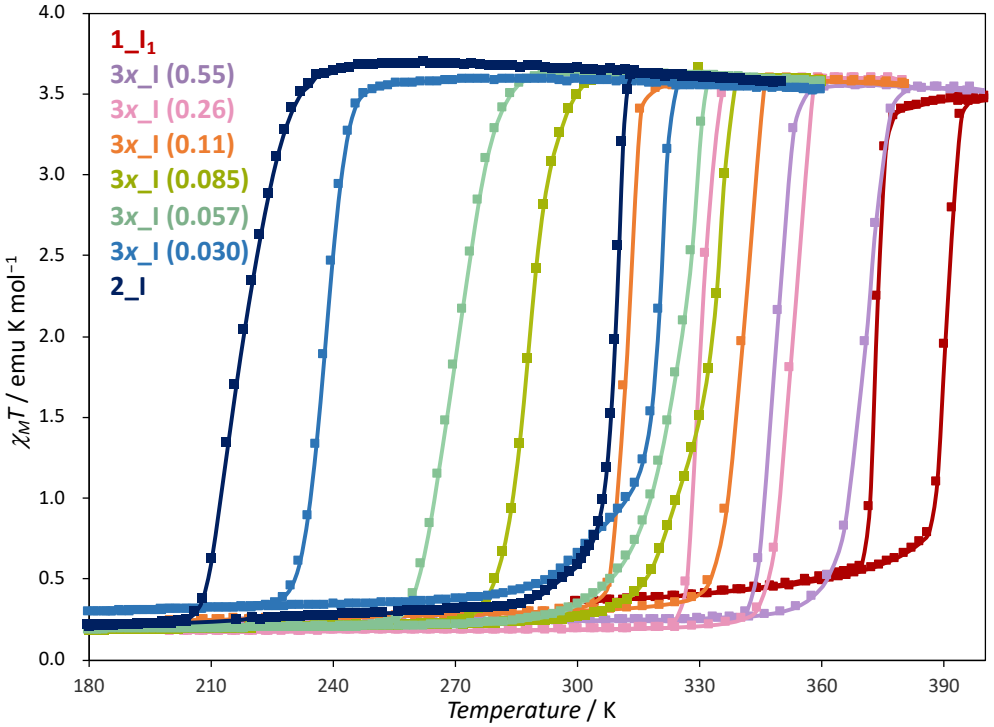

Figure 1-13. Magnetic behaviors of iodine-containing **1_I**, **2_I** and **3*x*_I**.

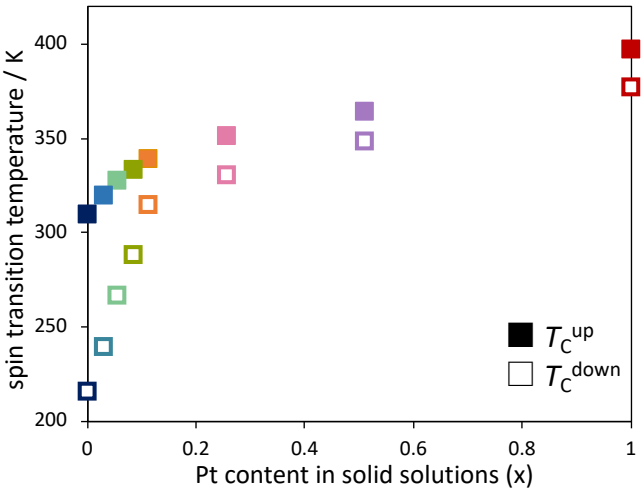

Figure 1-15. The correlation between Pt content and spin transition (ST) temperature.

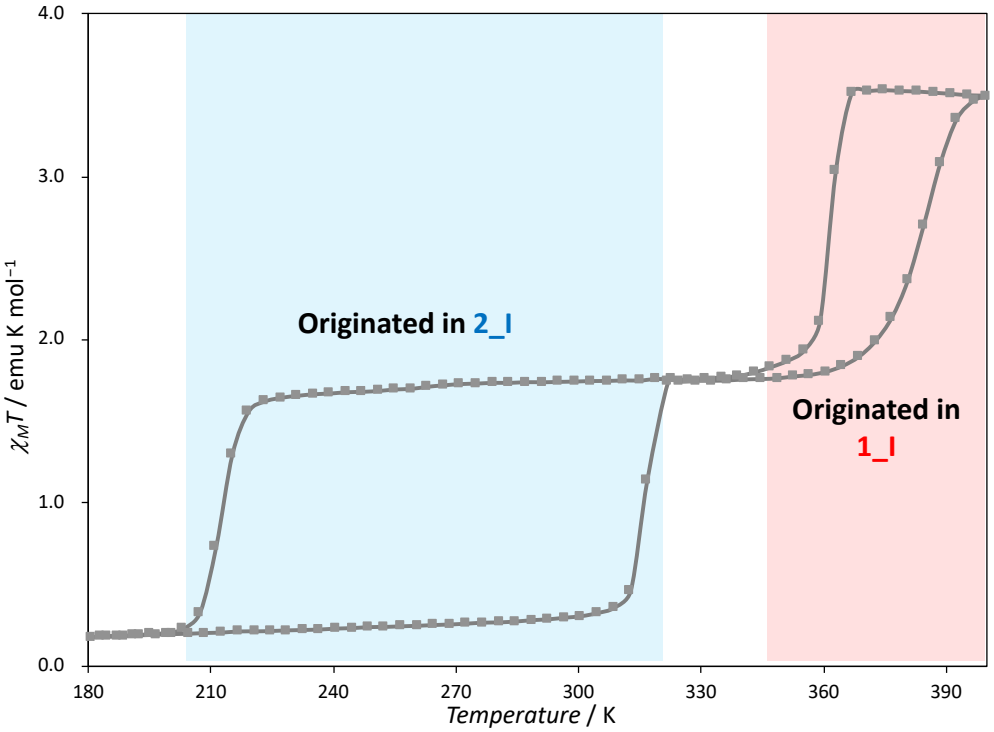

Figure 1-14. Simulated magnetic behavior of solid mixture (**1_I** : **2_I** = 1 : 1).

2-5. Magnetic Measurement of Solid Mixtures

To investigate the iodine migration between Pt and Pd sites in solid solutions, I measured magnetic behaviour of two kinds of iodine-containing solid mixtures, **1_I** and **2**; **2_I** and **1**. In the previous work of **1_I**, iodine migration from **1_I** to guest-free **1** through the spin transition. Here, I attempted to investigate the iodine migration in solid solution using solid mixture as a mimic condition. The iodine migration was evaluated through cooling and heating in SQUID equipment repeatedly. The magnetic behaviours are shown in the form of $\chi_M T$ *vs.* T plots (**Figure 1-16**). To avoid adsorption water, iodine-containing solid mixtures were stuffed with the gelatin capsule as soon as possible after exposing iodine vapour.

Both solid mixtures showed two-step spin crossover phenomenon, and each step corresponds to guest-free/iodine-containing **2** and guest-free/iodine-containing **1_I**, respectively. In the case of the solid mixture (**1_I** : **2** = 1 : 1), magnetic behaviour did not change even after 3rd cycle, which means the iodine migration from Pt sites to Pd sites did not occur. On the other hand, for the solid mixture (**1_I** : **2** = 1: 1), the shape of hysteresis at 1st step (lower temperature side) changed and the ST temperature of 2nd step (higher temperature side) increased with repeating each cycle. This change of magnetic behaviour in cooling and heating process indicated the iodine migration from **2_I** to guest-free **1**, in other word, from Pd sites to Pt sites. For these results, I considered that iodine coordinates to Pt sites preferentially, then I_2 molecules were confined between Pd sites. Measurements details are shown blow.

Magnetic Behaviour of Solid Mixture (1_I : 2 = 2 : 1)

The variable-temperature magnetic susceptibility measurements were carried out operating at 1000 Oe magnetic field and at temperatures between 260 and 400 K until 3rd cycle. The $\chi_M T$ value at 400 K was 3.45 emu K mol^{-1}, which closed to an expected value for the Fe^{II} ion in the HS state. The value of $\chi_M T$ at 260 K was 0.159 emu K mol^{-1}, which closed to an expected value for the Fe^{II} ion in the LS state. Both spin transition steps had around 20 K thermal hysteresis, and 1st step (lower temperature side) corresponds to guest-free **1**, 2nd step (higher temperature side) corresponds to iodine-containing **1_I**.

Magnetic Behaviour of Solid Mixture (1 : 2_I = 1 : 1)

The variable-temperature magnetic susceptibility measurements were carried out operating at 1000 Oe magnetic field and at temperatures between 180 and 400 K until 4th cycle. The $\chi_M T$ value at 400 K was 3.30 emu K mol^{-1}, which closed to an expected

value for the Fe^{II} ion in the HS state. The value of $\chi_M T$ at 180 K was 0.200 emu K mol^{-1}, which closed to an expected value for the Fe^{II} ion in the LS state. The 1st step (lower temperature side) corresponds to **1**, 2nd step (higher temperature side) corresponds to **2**. In the 1st step, decrease of hysteresis and a concavity were observed with repeating cooling and heating process because I_2 molecules came out from Pd sites and generated the domain of guest-free **1**. While, in the 2nd step, the ST temperature increased because I_2 molecules which came out from Pd sites trapped at Pt^{II} sites and formed I–Pt^{IV}–I bonds.

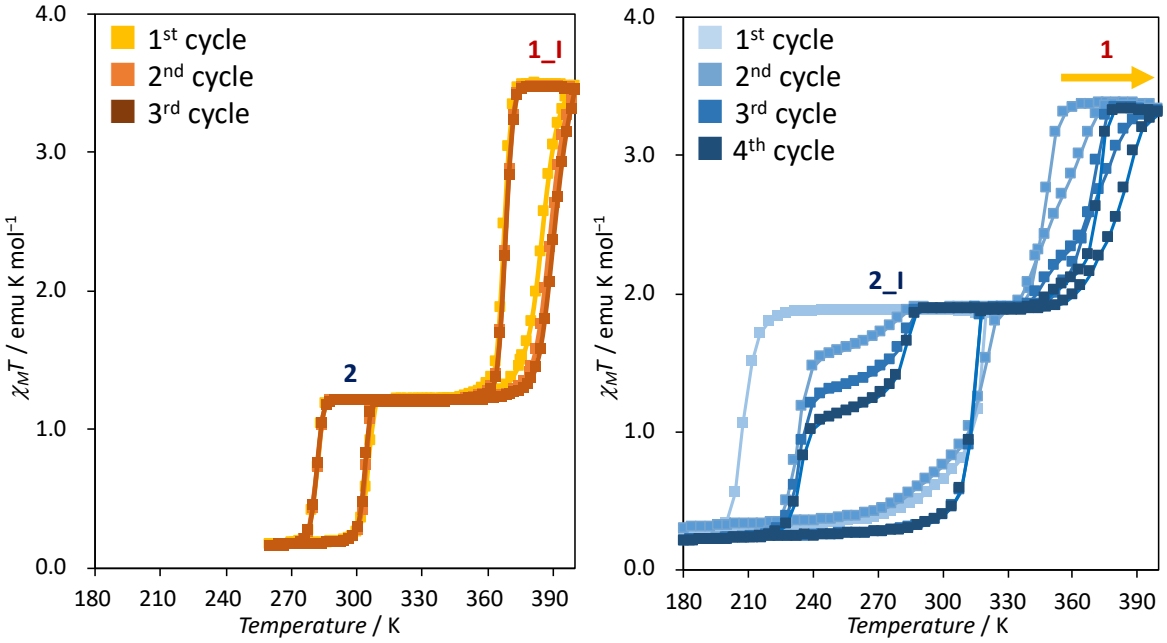

Figure 1-16. Magnetic behaviours of solid mixtures. (**1_I** : **2** = 2 : 1), left; (**1** : **2_I** = 1 : 1), right.

In this work, solid solutions achieved both high T_C^{up} and wide hysteresis only when x value was tiny. To consider these results, a hypothesis was set up. First, after exposing iodine to guest-free solid solutions, I–Pt^{IV}–I bonds are formed, then the I_2 molecule is confined between two Pd sites. In this case, the sites above and below I–Pt^{IV}–I sites cannot confine I_2 molecules. In the previous work, one of the author, R. Ohtani and his colleague reported the iodine migration phenomenon from **1_I** to guest-free **1**.[4] When the solid mixture of guest-free **1** and iodine adduct **1_I** was heated above ST temperature (450 K), the iodine migrated from the I–Pt^{IV}–I sites to Pt^{II} site, then iodine dispersed in the solid mixture. Although I–Pt^{IV}–I bonds were formed once, iodine can migrate among Pt sites. The iodine migration among Pt and Pd sites was evaluated using SQUID measurement. In the case of the solid mixture (**1_I** : **2** = 1 : 2), magnetic behaviour did not change even though the temperature exceeded was greater than the spin transition temperature of **1_I** (398K). The iodine migration from I–Pt^{IV}–I sites to Pd sites was not observed in the solid mixture (**1_I** and **2**). Which means I–Pt^{IV}–I bonds were formed irreversibility.

For these results and hypothesis, the relationship between T_C^{up} and the Pt content (x) in the iodine-containing solid solutions was considered. As mentioned above, T_C^{up} increases because of the formation of I–Pt^{IV}–I bonds, so it is easy to interpret the increasing of T_C^{up} with Pt content (x). In particular, when x was less than 0.1, the increasing rate of T_C^{up} was steeper, because the probability which Pt sites arrange continuously was low when x was low, so almost all Pt sites can form I–Pt^{IV}–I bonds (**Figure 1-17**). While when x is higher than 0.1, the probability which Pt sites arrange continuously is high. In this case, the Pt sites above and below I–Pt^{IV}–I site cannot form I–Pt^{IV}–I, consequently slowing down the rate of increase of T_C^{up}. To confirm the relationship between the x value and the ratio of Pt^{IV}/Pt. The amount of Pt^{IV} was estimated by TG curve (**Figure 1-18**). When x was smaller than 0.1, around 80 % Pt sites in solid solutions became Pt^{IV} and formed I–Pt^{IV}–I bonds. In terms of the relationship between hysteresis width and the Pt content (x) in the iodine-containing solid solutions, the confined I_2 molecules between Pd sites is important. The synergistic transition coupling between the spin transition of the framework and the order-disorder transition of confined I_2 molecules brings out wide hysteresis. When x value increase, the probability which Pd sites arrange continuously is low, which means the order-disorder transition of I_2 cannot be observed when x value is high.

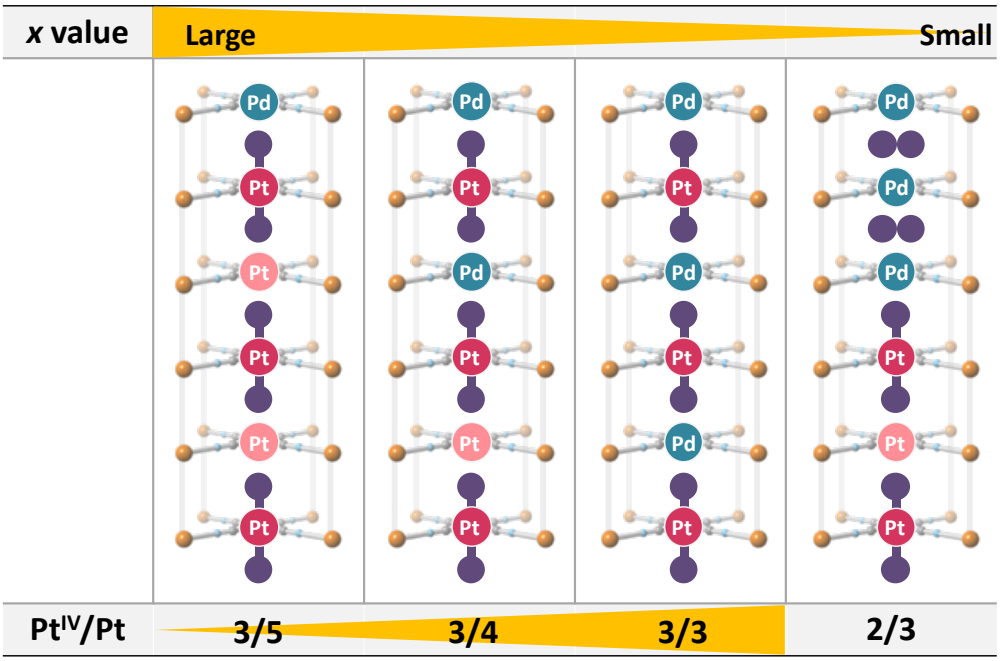

Figure 1-17. Schematic illustration of the correlation between the Pt content (x) and the ratio of Pt^{IV}site/Pt site.

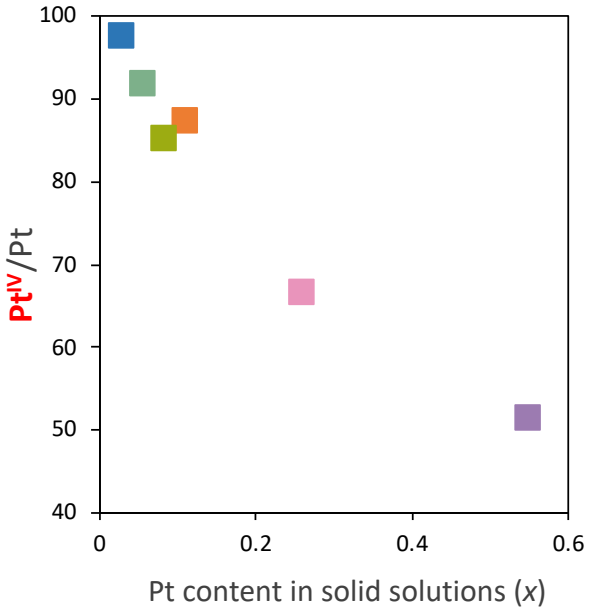

Figure 1-18. The correlation between the Pt content (x) and the ratio of Pt^{IV}site/Pt site.

Conclusion

In this work, 3D Hofmann-type metal-organic framework solid solution {Fe(pz)[$Pt_xPd_{1-x}(CN)_4$]} (**3*x***; pz = pyrazine) were preprared successfully. The dispersion of Pt and Pd was evaluated by SEM-EDX. All guest-free **3*x*** had a similar structure and magnetic behaviour with {Fe(pz)[$Pt(CN)_4$]} (**1**) and {Fe(pz)[$Pd(CN)_4$]} (**2**).

In the iodine-containing **3*x*_I,** both the spin transition (ST) temperature and hysteresis width were changed depending on the *x* value (Pt content). The ST temperature T_C^{up} increased with increasing *x* value. In the case of {Fe(pz)[$Pt^{II/IV}(CN)_4(I)_n$]} (**1_I**, *n* = 0.0-1.0), iodine coordinates to Pt sites and ligand field strength around Fe^{II} are raised through the σ-donor capability of cyano-nitrogen through Pt^{IV} enhanced by the strong π-donor capability of iodide. As the result, the low spin (LS) state is stabilized and T_C^{up} increases with increasing of iodine content (*n*), in other word, increasing of I–Pt^{IV}–I bonds. In the **3*x*_I**, the T_C^{up} increased depending on *x* value because I–Pt^{IV}–I bonds increased. On the other hand, the higher *x* value condition decreased the space for confine I_2 molecules, and so the hysteresis width decreased with increasing *x* value. In addition, I–Pt^{IV}–I and Pt^{II} sites arrange alternately because of the steric effect in **1_I**. However, in **3*x*_I**, Pd^{II} sites can play a role of the Pt^{II} sites, which means I–Pt^{IV}–I bonds form effectively in dilute condition: *x* value is lower. Therefore, the increasing rate of T_C^{up} is steeper when *x* value was small. I succeed to tune the magnetic behaviour using the difference of the interaction between open metal sites and iodine.

References

1. Ni, Z. P.; Liu, J. L.; Hoque, M. N.; Liu, W.; Li, J. Y.; Chen, Y. C.; Tong, M. L., *Coord. Chem. Rev.*, **2017**, *335*, 2843.
2. Ohba, M.; Yoneda, K.; Agusti, G.; Muñoz, M. C.; Gaspar, A. B.; Real, J. A.; Yamasaki, M.; Ando, H.; Nakao, Y.; Sakaki, S., *Angew. Chem. Int. Ed.*, **2009**, *48*, 4767−4771.
3. Southon, P. D.; Liu, L.; Fellows, E. A.; Price, D. J.; Halder, G. J.; Chapman, K. W.; Moubaraki, B.; Murray, K. S.; Létard, J. F.; Kepert, C. J., *J. Am. Chem. Soc.*, **2009**, *131*, 10998−11009.
4. Ohtani, R.; Yoneda, K.; Furukawa, S.; Horike, N.; Kitagawa, S.; Gaspar, A. B.; Muñoz, M. C.; Real, J. A.; Ohba, M., *J. Am. Chem. Soc.*, **2011**, *133*, 8600−8605.
5. Agusti, G.; Ohtani, R.; Yoneda, K.; Gaspar, A. B.; Ohba, M.; Sánchez-Royo, J. F.; Carmen Muñoz, M.; Kitagawa, S.; Real, J. A., *Angew. Chem. Int. Ed.*, **2009**, *121*, 9106−9109.
6. Morris, R. E.; Wheatley, P. S., *Angew. Chem. Int. Ed.*, **2008**, *47*, 4966−4981.
7. Janiak, C., *J. Chem. Soc. Dalton. Trans.*, **2003**, 2781−2804.
8. Li, B.; Wen, H. M.; Zhou, W.; Chen, B., *J. Phys. Chem. Lett.*, **2014**, *5*, 3468−3479.
9. Mukherjee, S.; Manna, B.; Desai, A. V.; Yin, Y.; Krishna, R.; Babarao, R.; Ghosh, S. K., *Chem. Commun.*, **2016**, *52*, 8215−8218.
10. Chughtai, A. H.; Ahmad, N.; Younus, H. A.; Laypkov, A.; Verpoort, F., *Chem. Soc. Rev.*, **2015**, *44*, 6804−6849.
11. Lee, J.; Farha, O. K.; Roberts, J.; Scheidt, K. A.; Nguyen, S. T.; Hupp, J. T., *Chem. Soc. Rev.*, **2009**, *38*, 1450−1459.
12. Dong, M. J.; Zhao, M.; Ou, S.; Zou, C.; Wu, C. De., *Angew. Chem. Int. Ed.*, **2014**, *53*, 1575−1579.
13. Chen, L.; Liu, D.; Peng, J.; Du, Q.; He, H., *Coord. Chem. Rev*., **2020**, *404*, 213113.
14. Kreno, L. E.; Leong, K.; Farha, O. K.; Allendorf, M.; Van Duyne, R. P.; Hupp, J. T., *Chem. Rev.*, **2012**, *112*, 1105−1125.
15. Furukawa, H.; Cordova, K. E.; O'Keeffe, M.; Yaghi, O. M., *Science*, **2013**, *341*, 1230444.
16. Li, B.; Wen, H. M.; Cui, Y.; Zhou, W.; Qian, G.; Chen, B., *Adv. Mater.*, **2016**, *28*, 8819−8860.
17. Czaja, A. U.; Trukhan, N.; Müller, U., *Chem. Soc. Rev.*, **2009**, *38*, 1284−1293.

18. Hu, Z.; Deibert, B. J.; Li, J., *Chem. Soc. Rev.*, **2014**, *43*, 5815−5840.
19. Jain, P.; Ramachandran, V.; Clark, R. J.; Hai, D. Z.; Toby, B. H.; Dalal, N. S.; Kroto, H. W.; Cheetham, A. K., *J. Am. Chem. Soc.*, **2009**, *131*, 13625−13627.
20. Hurd, J. A.; Vaidhyanathan, R.; Thangadurai, V.; Ratcliffe, C. I.; Moudrakovski, I. L.; Shimizu, G. K. H., *Nat. Chem.*, **2009**, *1*, 705−710.
21. Givaja, G.; Amo-Ochoa, P.; Gómez-García, C. J.; Zamora, F., *Chem. Soc. Rev.*, **2012**, *41*, 115−147.
22. Wang, H. Y.; Ge, J. Y.; Hua, C.; Jiao, C. Q.; Wu, Y.; Leong, C. F.; D'Alessandro, D. M.; Liu, T.; Zuo, J. L., *Angew. Chem. Int. Ed.*, **2017**, *56*, 5465−5470.
23. Cirera, J., *Rev. Inorg. Chem.*, **2014**, *34*, 199−216.
24. Gütlich, P.; Hauser, A.; Spiering, H., *Angew. Chem. Int. Ed.*, **1994**, *33*, 2024−2054.
25. Bousseksou, A.; Molnár, G.; Salmon, L.; Nicolazzi, W., *Chem. Soc. Rev.*, **2011**, *40*, 3313−3335.
26. Sato, O.; Tao, J.; Zhang, Y. Z., Angew. Chem. Int. Ed., 2007, 46, 21252187.
27. Brooker, S., *Chem. Soc. Rev.*, **2015**, *44*, 2880−2892.
28. Spiering, H., Elastic Interaction in Spin-Crossover Compounds. In Spin Crossover in Transition Metal Compounds III, **2006**.
29. Bousseksou, A.; McGarvey, J. J.; Varret, F.; Real, J. A.; Tuchagues, J.-P.; Dennis, A. C.; Boillot, M. L., *Chem. Phys. Lett.*, **2000**, *318*, 409−416.
30. Baldé, C.; Desplanches, C.; François Létard, J.; Chastanet, G., *Polyhedron*, **2017**, *123*, 138−144.
31. Gao, J.; Cong, J.; Wu, Y.; Sun, L.; Yao, J.; Chen, B., *ACS Appl. Energy Mater.*, **2018**, *1*, 5140−5144.
32. Tayagaki, T.; Galet, A.; Molnár, G.; Carmen Muñoz, M.; Zwick, A.; Tanaka, K.; Real, J. A.; Bousseksou, A., *J. Phys. Chem. B.*, **2005**, *109*, 14859−14867.
33. Niel, V.; Martinez-Agudo, J. M.; Muñoz, M. C.; Gaspar, A. B.; Real, J. A., *Inorg. Chem.*, **2001**, *40*, 3838−3839.
34. Molnár, G.; Niel, V.; Gaspar, A. B.; Real, J. A.; Zwick, A.; Bousseksou, A.; McGarvey, J. J., *J. Phys. Chem. B*., **2002**, *106*, 9701−9707.
35. Cobo, S.; Molnár, G.; Real, J. A.; Bousseksou, A., *Angew. Chem. Int. Ed.*, **2006**, *45*, 5786.
36. Lammert, M.; Glißmann, C.; Stock, N., *Dalton. Trans.*, **2017**, *46*, 2425−2429.
37. Sapnik, A. F.; Geddes, H. S.; Reynolds, E. M.; Yeung, H. H. M.; Goodwin, A. L., *Chem. Commun.*, **2018**, *54*, 9651−9654.

38. Das, S.; Kim, H.; Kim, O., *J. Am. Chem. Soc.*, **2009**, *131*, 3814−3815.
39. Yao, Q.; Sun, J.; Li, K.; Su, J.; Peskov, M. V.; Zou, X., *Dalton. Trans.*, **2012**, *41*, 3953−3955.

Chapter 2

Modulation of Spin Transition Behaviour by Patterning of Inter-layer Space through the Layer-by-Layer Method

Abstract

SURMOF (surface-mounted metal-organic framework) prepared by the Layer-by-Layer (LbL) method is one of the thin film MOFs[1,2], and they have high orientation and crystallinity compared with other thin films MOFs.[3] More recently, hetero-structured SURMOFs (hetero-SURMOFs) are attracting attention as an approach to design the crystal structure.[4,5] In this work, hetero-SURMOFs consisting of "Pt block" {Fe(pz)[Pt(CN)$_4$]} (pz = pyrazine; **1**) and "Pd block" {Fe(pz)[Pd(CN)$_4$]} (**2**) were prepared. As mentioned in Chapter 1, when iodine is used for guest-molecules, compounds **1** and **2** provide interesting magnetic behaviours because of the different interactions with iodine. Therefore, hetero-SURMOFs are expected to exhibit unique magnetic behaviour depending on the arrangement of Pt block and Pd block. The orientation and crystallinity of hetero-SURMOFs were evaluated by XRD measurement. After exposing iodine vapour, both I-Pt^{IV}-I bonds and I_2 molecules were observed in hetero-SURMOFs by Raman spectra. The spin transition (ST) behaviour was proved by the temperature dependence of Raman spectroscopy. Comparing with guest-free hetero-SURMOFs, all iodine-containing SURMOFs indicated an increase of ST temperature. Furthermore, the SCO behavior was different depending on the different layered structures using Pt and Pd block.

Introduction

Recently, the MOF thin films technique gained significant importance[6] in order to expand the MOFs application fields such as smart membranes[7,8,9], catalytic coatings[10], or sensing devices.[11,12] The seeded growth[13], spin coating[14], and the Langmuir-Blodgett method[15] have been reported as the way for the synthesis of MOF thin film.[16] However, MOF thin films prepared by these methods were not enough for the future applications required monolithic, low defect density, and crystal orientation. In order to make full these requests, some of the researchers focus on the layer-by-layer (LbL) method (**Figure 2-1**)[17] which originated in the fabrication of multilayer organic LB films[18] by Langmuir and Blodgett in 1937. MOF thin films fabricated using this LbL method are called surface-mounted metal-organic frameworks (SURMOFs), and this approach has been shown to provide monolithic and high crystallinity, and highly oriented MOF thin films on suitable substrates.[19,20] In 2007, Wöll and his co-workers reported the first SURMOF of **HKUST-1** $[Cu_3(btc)_2(H_2O)_n]$ (H_3btc = benzen-1,3,5-tricarboxylic acid) which had both high orientation and crystallinity.[17] In this first report, Au substrate functionalized by self-assembly monolayer (SAM) was used for its substrate.[17] In general, when substrate metal is coinage metal like gold or copper, thiol-based SAMs are used.[21] Because of the chemical reaction between the thiol groups and Au atoms of the substrate surface, thiol-based monolayers arrange on the substrate (R-S-H + Au → R-S-Au + $1/2H_2$) (R = any functional species).[22,23] Not only Au substrate but also silver, silicon, silicon oxide, quartz, alumina, etc. have been studied as a substrate for extensively expanding their application field. One of the objectives in SURMOF research is preparing hetero-structured SURMOF (hetero-SURMOF) because the systems in which the components are segregated material have the potential to be hierarchical materials. Wöll

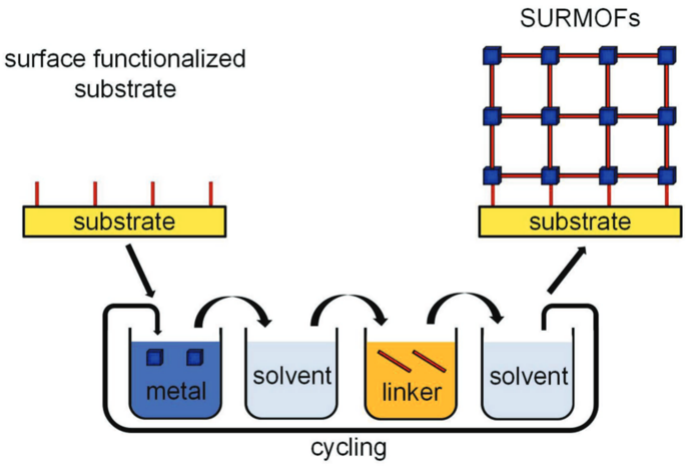

Figure 2-1. Schematic illustration of Layer-by-Layer (LbL) method.

and his co-workers reported hetero-SURMOF containing photo switchable linkers between *trans* and *cis* which can release guest molecules: butanediol only when the hetero-SURMOF was irradiated with light.[24] The bottom of hetero-SURMOF (50 layers) was {Cu_2(BPDC)$_2$(BiPy)} (BPDC = biphenyl-4,40-dicarboxylic acid, BiPy = 4,40-bipyridine) which can uptake and storage butanediol, and the top (45 layers) was photo-switchable MOFs {Cu_2(AB-BPDC)$_2$(BiPy)} (AB-BPDC = 2-azobenzene-4,40-biphenyldicarboxylic acid). They determined the photo-switchable properties of SURMOF by QCM (quartz crystal microbalance). QCM method is useful for the evaluation of absorption properties on SURMOF which has a tiny amount compound on the substrate. Not only absorption measurement but also other physical measurements are different from the evaluation of bulk MOF because of a tiny amount and substrate. Comparing with the solid solutions in which more than two components are dispersion, hetero-SURMOFs have some domains like "block", so that each single MOF can perform each property such as storage and photo-switching.

In this research, the author focused on Hoffmann-type MOF thin film. In 2006, Bousseksou and co-workers prepared 3D Hofmann-type MOF {Fe(pz)[M(CN)$_4$]} (pz = pyrazine, M = Ni, Pd, Pt (**1**)) on Au substrate through the LbL method[25,26] (a total of 30 cycles). It was the first report on 3D Hofmann-type MOF thin film mounted on the substrate, however, the orientation and crystallinity had not been evaluated until when Kitagawa and co-workers demonstrated it using XRD in 2012.[27] In this report, they carried out Raman microscopy measurements to probe spin state because the amount of compound on substrate was not enough to measure by SQUID (**Figure 2-3**). They focused on the intensity ratio of the pyrazine modes at 1025 and 1230 cm^{-1} during the spin transition (ST). For the results, MOF thin film revealed a hysteresis width around RT as well as bulk MOF. The same research group demonstrated the nanopatterned thin film of compound **1**.[26] In this work, the substrate was coated by PMMA (Polymethyl methacrylate) to the pattern in nanoscale. They evaluated the quality of thin films by AFM and surface plasmon resonance (SPR) observation without XRD measurement. Kitagawa and his-coworker evaluated the orientation and crystallinity of thin film **1** (a total of 30 cycles) by synchrotron X-ray diffraction in 2012. Comparing with reports by Bousseksou group, they did not use 4,4'-azopyridine as an anchoring layer. They monitored the thin film growth by the infrared refraction absorption spectroscopy (IRRAS). The maximum absorbance of the ν(CN) mode increased with increasing the number of cycles linearly. From Raman spectroscopy, prepared thin film was high spin (HS) state at RT. Synchrotron radiation was selected for XRD measurement to obtain high-quality information because of the low thickness and density of the thin film. In the horizontal direction (in-plane,

grading-incidence mode), some peaks indexed *hk0* diffraction were observed. While, two peaks indexed 00l were observed in the vertical direction (out-of-plane, *θ-2θ* mode). These results of XRD measurement provided the high orientation and crystallinity of thin film. Besides, *in situ* XRD measurement revealed its guest molecules (benzene) adsorption. The correlation between lattice constants (*a* or *c* axis) and pressure indicated benzene adsorption expanded the interlayer spacing. Although the structure and physical properties of homo structured thin film have been already demonstrated, there is no report on hetero-SURMOF of Hofmann-type MOF. Hetero-SURMOF has the potential to enhance or combine its physical properties. As mentioned in Chapter 1, the magnetic behaviour of iodine-containing **3*x*_I** (**3*x***: {Fe(pz)[$Pt_xPd_{1-x}(CN)_4$]}) changed depending on *x* value. However, the wide hysteresis was observed only when *x* value was tiny because Pt^{II} sites form I–Pt^{IV}–I bonds preferentially, and the generated I–Pt^{IV}–I sites disturb confinement of I_2 between Pd sites. In contract with solid solutions in which Pt and Pd sites were dispersed, hetero-SURMOF can form Pt sites domain and Pd sites domain separately. Here, three types of hetero-SURMOFs were prepared (**Figure 2-2**) and evaluated their spin crossover phenomenon by Raman spectroscopy.

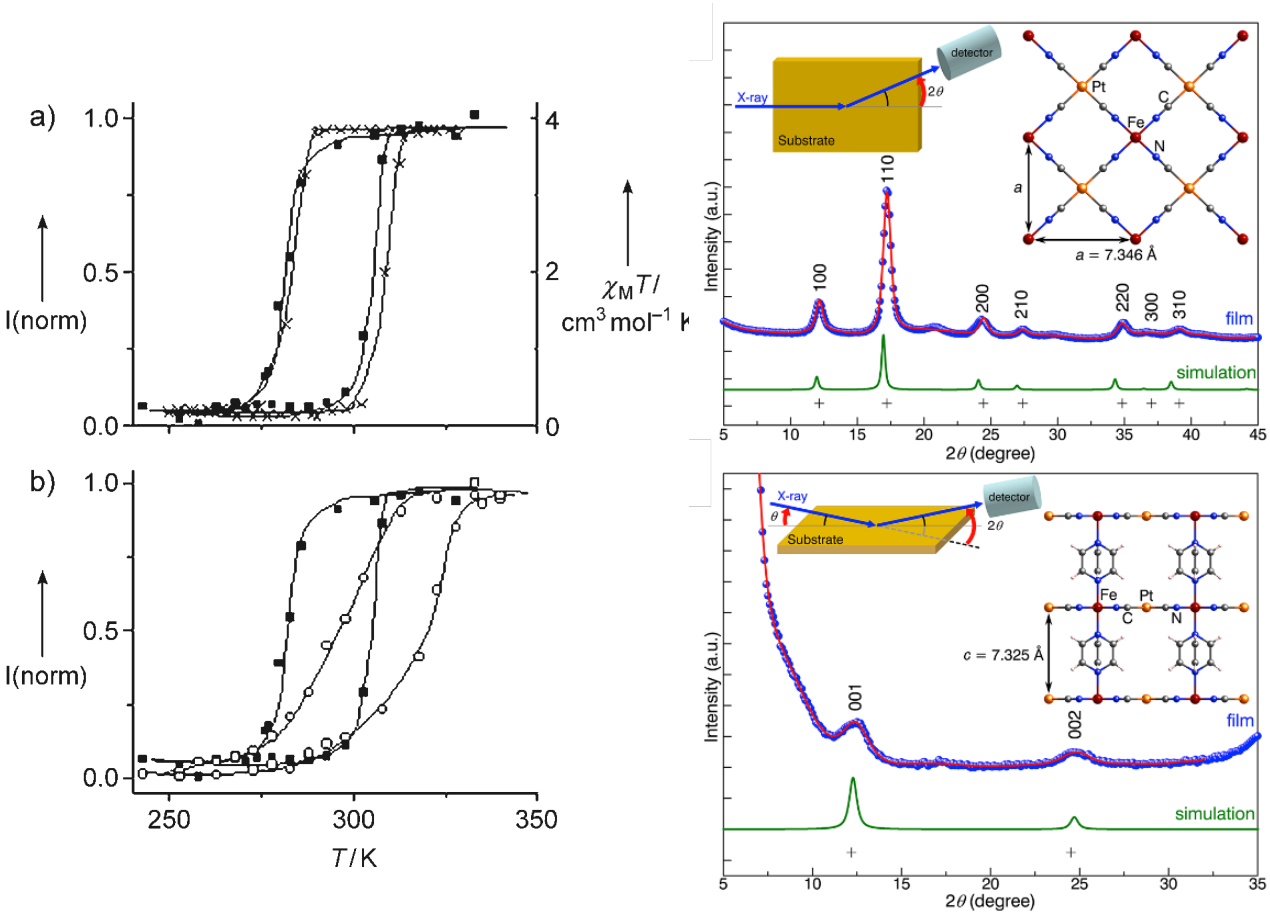

Figure 2-3. The temperature dependence $\chi_M T$ (×) and normalized Raman intensity ratio ((I (norm) = I(1025 cm^{-1})/I(1230 cm^{-1});■) of bulk MOF **1** (left a). Comparison of bulk **1** (■) and thin film **1** (□) by Raman intensity ratio (left b). Synchrotron XRD patterns of thin film **1** (λ = 1.555 Å, RT). In-plane XRD patterns provided diffraction peaks originated from *hk0* (right top). Out-plane XRD patterns provided diffraction peaks indexed 001 and 002 (right bottom).

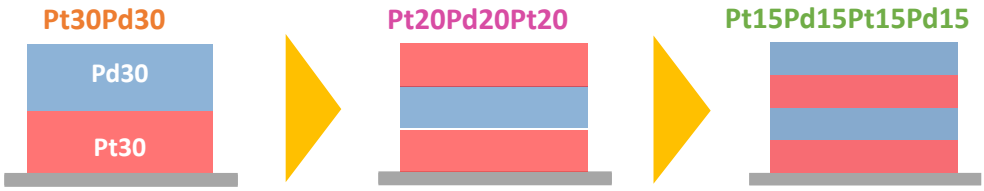

Figure 2-2. Schematic representations of hetero-SURMOFs: **Pt30Pd30**, **Pt20Pd20Pt20** and **Pt15Pd15Pt15Pd15**. The number after Pt or Pd indicates cycle number of LbL method (example: **Pt30Pd30** indicates {Fe(pz)[Pd(CN)$_4$]} 30 cycles after {Fe(pz)[Pt(CN)$_4$]} 30 cycles).

Experiments

1. Physical Measurements

All compounds were characterized using Raman spectroscopy, X-ray diffraction measurement. The arrangement of Pt and Pd in hetero-SURMOF was confirmed by elemental mapping using SEM-EDX (SEM-energy dispersive X-ray spectrometry, Zeiss ULTRA55, with 10.00 kV accelerating voltage). Raman spectra were recorded with a Jasco NRS-1000. For temperature dependence Raman spectra, the sample stage Model S84_C from S.T. japan Inc. was attached (**Figure 2-4**). The excitation source was a 632 nm He-Ne laser, and the laser power was carefully kept low to avoid local heating during laser irradiation. XRD measurement was recorded using a Rigaku Smart lab spectrometer with graphite-monochromated CuK_α radiation. To observe the surface of SURMOF, atomic force microscopy (AFM) images were obtained using a Nanocute system (SII NanoTechnology Inc.).

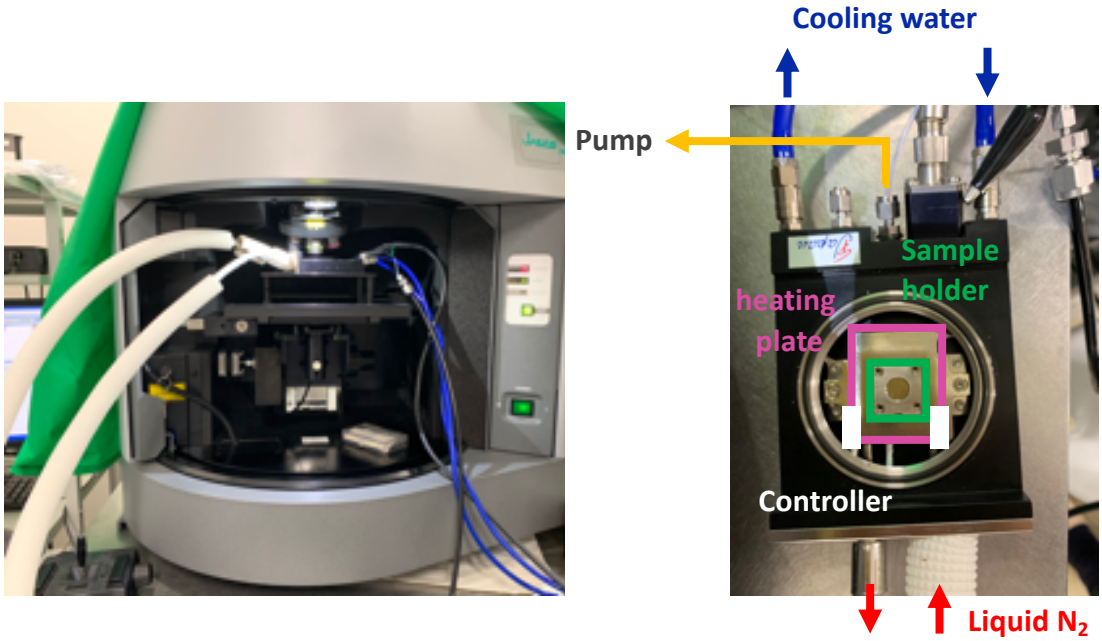

Figure 2-4. Raman spectroscopy and sample state for temperature dependence of Raman spectra.

2. Materials

$[(C_4H_9)_4N]_2M(CN)_4$ (M = Pd or Pt) were prepared by reported method using tetrabutylammonium perchlorate and $K_2[M(CN)_4]$. Other chemicals purchased were of reagent grade and used without further purification.

3. Preparation of Compounds

3-1. Guest-free solid solutions

The substrates were prepared with chromium layer as a buffer between silicon wafers (5 nm) and gold layer on the top (100 nm) purchased from Nilaco Corp. The typical substrate size was 15 × 15 × 0.5 mm^3. The Au/Cr/Si substrate was washed by basic piranha solution (NH_4OH and H_2O_2) at 70 ℃, then soaked in an EtOH solution of 4-mercaptopyridine (1mM) for a day after. These substrates were alternately soaked in EtOH solutions of 200 mM $Fe(BF_4)_2 \cdot 6H_2O$, 30 mM $[(C_4H_9)_4N]_2M(CN)_4$ (M = Pt or Pd), and 200 mM pyrazine for 3 min at 198 K until a total of each cycles, and the substrates were washed with EtOH after each soaking to remove the uncoordinated metal connectors or organic linkers.

3-2. Iodine-containing solid solutions

Iodine-exposed thin films were prepared by exposing iodine vapour at room temperature overnight. Before exposing iodine vaper, these thin films were vacuumed overnight at RT. The colour of samples changed from yellow to black after exposing iodine vapour.

Results and Discussion

1. Characterizations of Guest-free Hetero-SURMOFs

1-1. Raman Spectra

In the case of these bulk compounds, ν(C≡N) modes appear around 2200cm^{-1} and pyrazine internal modes between 600 and 1600 cm^{-1} (as mentioned in Chapter 1). The lower frequency modes originated from metal-ligand vibrations.[28] Comparing with bulk guest-free **1** and **2**, prepared hetero-SURMOFs showed the same spectra (**Figure 2-5**). Furthermore, the spin state of prepared hetero-SURMOFs at RT could be evaluated. The spin state of Hofmann-type MOFs has been evaluated by using the Raman spectra in the previous work.[25] In the reported paper, Bousseksou suggested a shift from 645 to 675 cm^{-1} (the intense pyrazine in-plane bending mode) during ST from the HS state to the LS state was useful. Using this suggestion, the prepared thin films were HS state at RT as well as bulk samples. The intensity ratio of ν(ring) modes at 1025 cm^{-1} and δ(CH) at 1230 cm^{-1} indicated HS state as well.

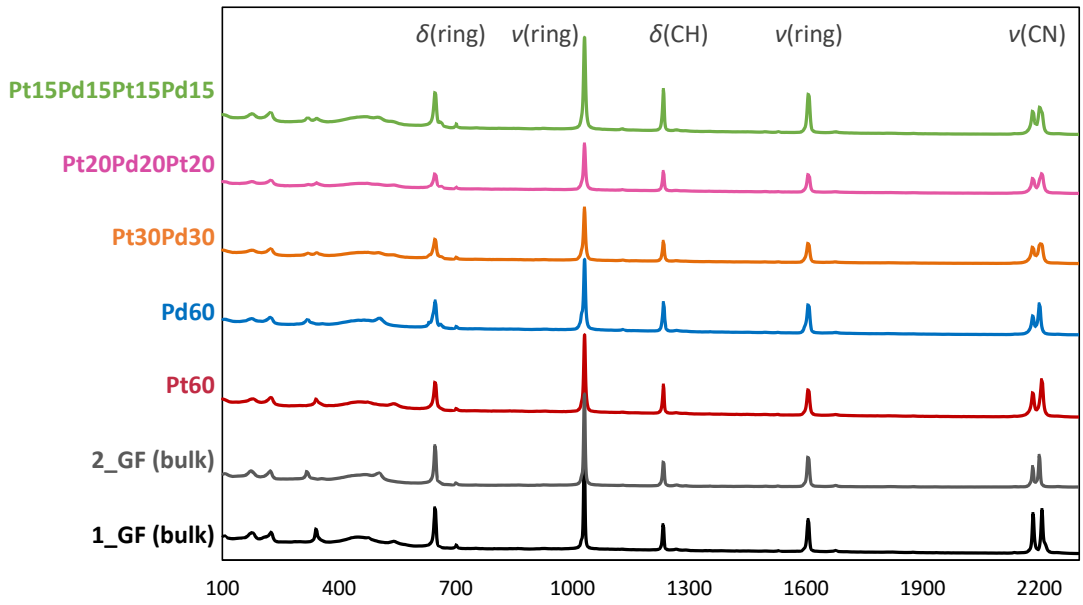

Figure 2-5. Raman spectra of bulk MOF **1**, **2** and hetero-SURMOFs at RT.

1-2. XRD patterns

The crystallinity and orientation of SURMOF are evaluated by XRD in general.[1,29,30] The out-of-plane scan provides information on the direction perpendicular to the substrate, whereas the in-plane scan provides information in the horizontal direction to the substrate (**Figure 2-6**). In the case of the in-plane scan, to remove the effect of substrate diffraction, the incident-angle fixed 2θ scan geometry (GI-XRD; grazing-incidence mode) is adopted. The rising of background is caused by the Au substrate.

In the out-of-plane diffraction (**Figure 2-7**), four peaks were observed. In the previous work, only two peaks originated in *00l* diffraction were obtained. Comparing with previous works, the orientation of prepared hetero-SURMOFs was lower. One of the reasons for the lower orientation of hetero-SURMOFs might be cycle number. In this work, all samples were deposited through 60 cycles which were double times cycles and increasing of cycles number brings out the decline of orientation. For the high orientation SURMOF, the sheller equation provides the thickness of films, however, the orientation of prepared SURMOF was not enough to discuss it.

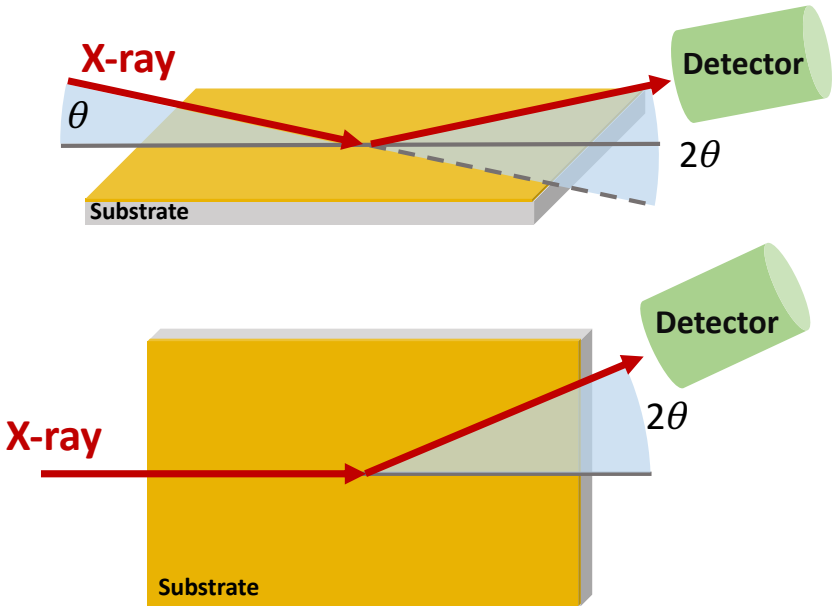

Figure 2-6. Schematic illustration of several experimental geometries of XRD measurements to evaluation of SURMOFs. Out-of-plane (above); in-plane geometries (below).

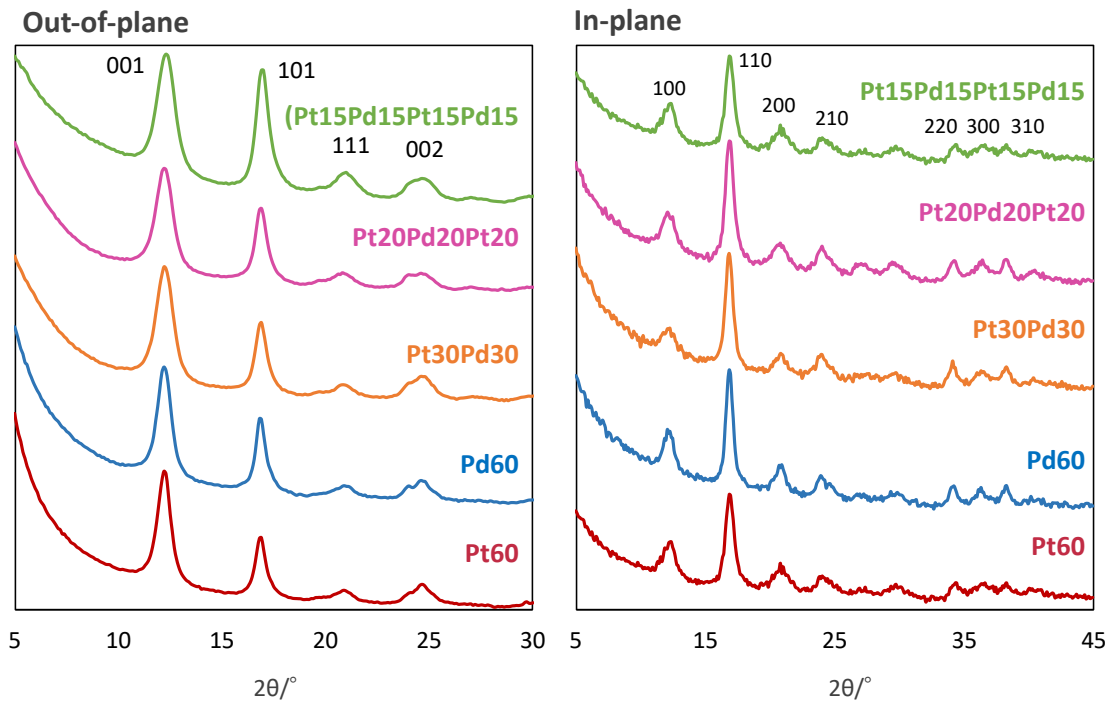

Figure 2-7. XRD patterns of SURMOFs. Out-of-plane diffraction shows pyrazine ligand-mediated interlayer spacing (left); In-plane diffraction shows an ordering of 2D sheet of cyano-bridged layer (right).

1-3. AFM Images

Atomic force microscopy (AFM) images were obtained by Nanocute system (SII Nano Technology Inc.). To investigate the roughness depending on the cycle number (thickness of films), three types SURMOFs: **Pt15**, **Pt30** and **Pt60** were evaluated. The average roughness of these SURMOFs were 18.05 nm, 70.64 nm and 113.7 nm, respectively (**Figure 2-8**). From amplitude images, MOF mounted on the substrate uniformly, and the domain of particle was observed (**Figure 2-9**).

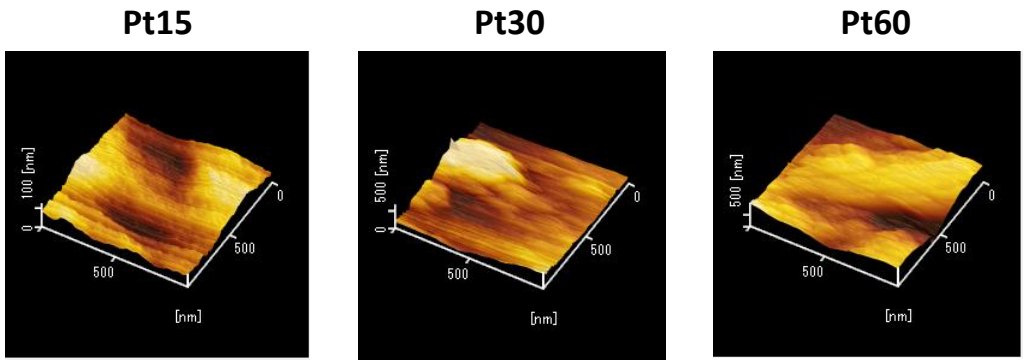

Figure 2-8. AFM 3D images.

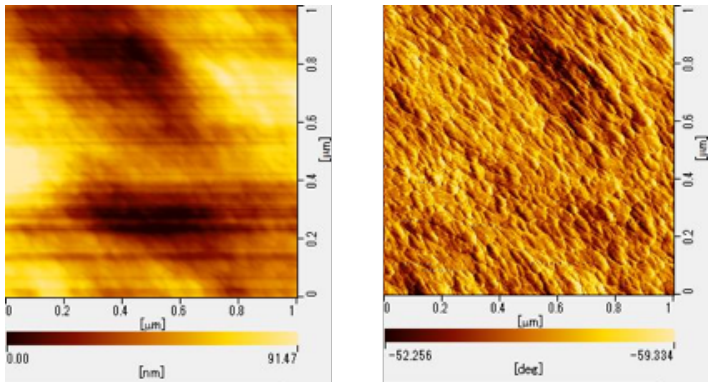

Figure 2-9. AFM images of SURMOFs at RT. Height image (left); Amplitude image (right).

1-4. SEM-EDX Images

SEM (scanning electron microscopy) analysis hetero-SURMOFs was performed using a Zeiss ULTRA55 (10.00 kV accelerating voltage). For this measurement, the substrate was cut and pasted on the holder with carbon tape. In this measurement, the accelerating voltage was decided at 10.00 kV to avoid the decomposition of SURMOFs. From SEM images, the thickness of SURMOFs prepared with 60 cycles was around 1 μm (**Figure 2-10**).

The arrangement of Pt block and Pd block was evaluated by SEM-EDX. **Pt30Pd30** and **Pd30Pt30** were selected for SEM-EDX measurement because it was easy to observe the arrangement. In this measurement, to avoid overlap in spectra of three elements: platinum, palladium, and gold which have a spectrum at the similar energy level, the accelerating voltage 20.00 kV was determined. **Figure 2-11** shows the elemental mapping of two SURMOFs. As a result, the arrangement of Pt block (pink) and Pd block (light blue) could be observed. In the elemental mapping of Pt, the colour intensity was the strongest in the bottom due to the gold substrate.

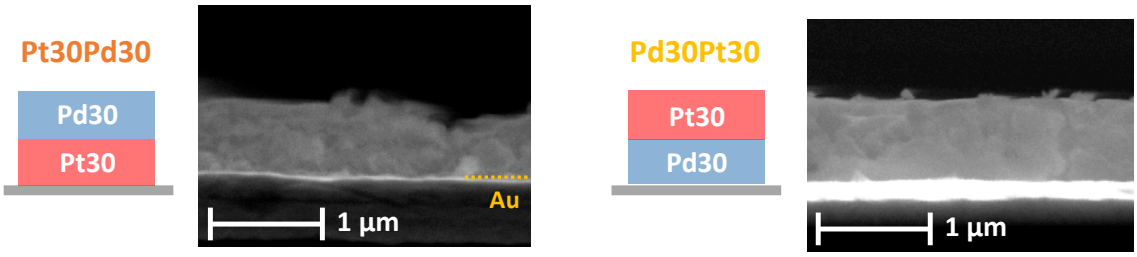

Figure 2-10. Schematic illustration and SEM images of hetero-SURMOFs. The accelerating voltage was 10.00 kV, the magnitude was 10.00 KX.

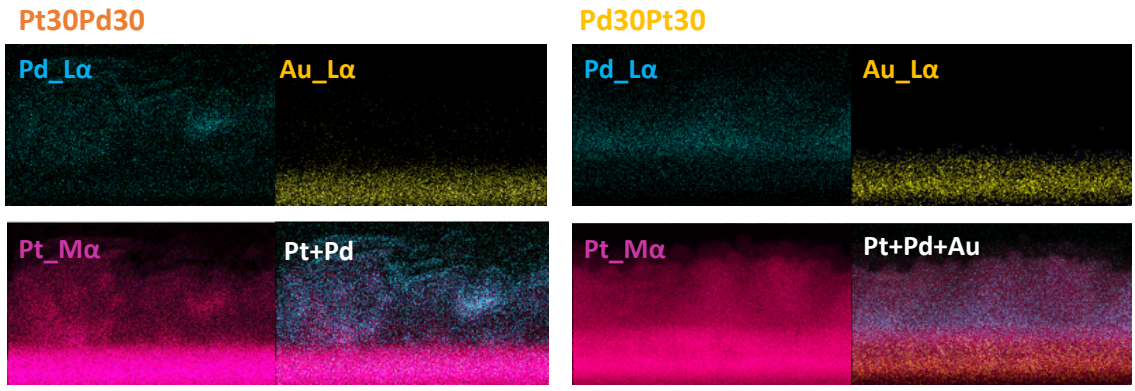

Figure 2-11. Elemental mapping of hetero-SURMOFs, **Pt30Pd30** and **Pd30Pt30**. The accelerating voltage was 20.00 kV in order to use the spectrum originated from Lα at Au elemental mapping. The magnitude was 10.00 KX. Pt, pink; Pd, blue; Au, yellow.

2. Characterizations of Iodine-containing Thin-film MOFs

2-1. Raman Spectra at RT

Raman spectroscopy was performed to confirm iodine adsorption on hetero-SURMOFs (**Figure 2-12**). The ν(C≡N) modes appear around 2200cm^{-1} and pyrazine internal modes between 600 and 1600 cm^{-1} as well as guest-free hetero-SURMOFs.[28] A very strong Pt-I vibration peak was observed around 130 cm^{-1} in all SURMOFs including Pt block. Comparing with bulk MOF **2_I**, I_2 monomer vibration peak around 170 cm^{-1} was observed in SURMOFS including Pd remarkably. The SURMOF roughness might be contributing to this result. In addition, the spin state of SURMOFs at RT was estimated using the intensity ratio of ν(ring) modes at 1025 cm^{-1} and δ (CH) at 1230 cm^{-1}. For the results, iodine-containing SURMOFs including Pt indicated LS state. Which means, the ST temperature T_C^{up} might be increased by forming I–Pt^{IV}–I bonds.

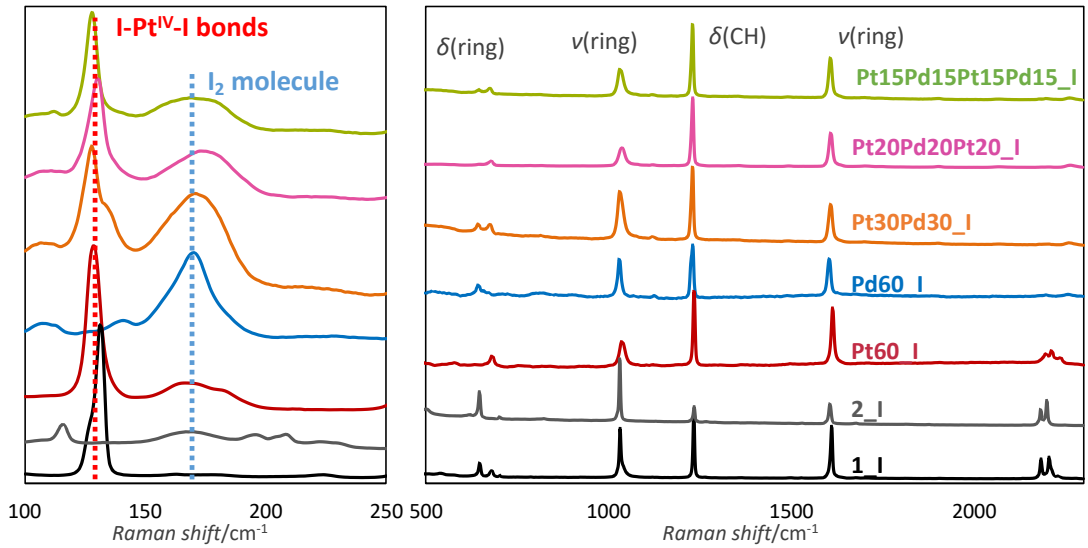

Figure 2-12. Raman spectra of iodine-containing hetero-SURMOF at RT.

2-2. Temperature Dependence of Raman Spectra

In the previous work, the ST behaviour of Hofmann-type SURMOFs has been probed by using the temperature dependence of Raman spectra.[25] Using this suggestion, the ST behaviours of iodine-containing hetero-SURMOF were probed through the ratio of ν(ring) modes at 1025 cm^{-1} and δ (CH) at 1230 cm^{-1}. **Figure 2-13** shows the temperature dependence of Raman spectra of guest-free **Pt30Pd30** as an example. From these spectra, the intensity ratio was picked up to probe ST behavour. The ST behaviours of SURMOFs are shown in the form of *Intensity ratio* (I (1025cm^{-1}) / I (1230 cm^{-1})) *vs. T* plots.

Figure 2-14 shows the comparison of the ST behaviour in guest-free SURMOF (**Pt30Pd30**) and bulk MOF (solid mixture **1** : **2** = 1 : 1). In general, crystal-size effects on the spin crossover (SCO) phenomenon because the interaction between electron and lattice is important in these behaviours.[31,32,33] In the previous works on nano- or meso-sized particle of 3D Hofmann-type MOF, decreasing of ST temperature and extinguish of hysteresis have been demonstrated.[34,35,30] The crystal-downsizing effect has been observed in the case of thin film.[36] Therefore, the difference of ST behaviour between SURMOF and bulk MOF was considered as the result of decreasing of cooperativity by the crystal-downsizing. **Figure 2-15** shows the ST behaviour on guest-free/iodine-containing SURMOFs at the same graph (guest-free, pale colour; iodine-containing, deep colour). Comparing with each guest-free SURMOF, iodine-containing SURMOFs provided higher ST temperature. The increase in ST temperature was considered as the result of forming I–Pt^{IV}–I bonds. Interestingly, **Pt30Pd30_I** showed two-step SCO phenomena, although iodine-containing hetero-SURMOF **Pt20Pd20Pt20_I** and **Pt15Pd15Pt15Pd15_I** showed one step SCO phenomenon. In addition, solid mixture (**1_I** : **2_I** = 1 : 1) showed similar SCO behaviour with **Pt30Pd30_I**.

In this work, the cycle number of LbL was decided until 60 cycles because the cycle number effected on crystal-size.[36] However, the block thickness of prepared three types of SURMOFs was different. In addition, the number of boundary surfaces increased with decreasing in block thickness. The Pt block and Pd block were mixed and formed like solid solution phase around the boundary surface because the roughness of the SURMOF surface evaluated by AFM measurement was a nano-sized scale. **Pt20Pd20Pt20_I** and **Pt15Pd15Pt15Pd15_I** had the boundary surface formed by different metal (Pt and Pd) more than **Pt30Pd30_I**. Therefore, **Pt20Pd20Pt20_I** and **Pt15Pd15Pt15Pd15_I** formed a solid solution phase for wide areas in SURMOF. However, **Pt30Pd30_I** had enough thickness to obtain both effects of Pt block and Pd

block, and so it showed two-step SCO originated from Pt block (SCO at a higher temperature) and Pd block (SCO at a lower temperature) respectively in same way with solid mixture.

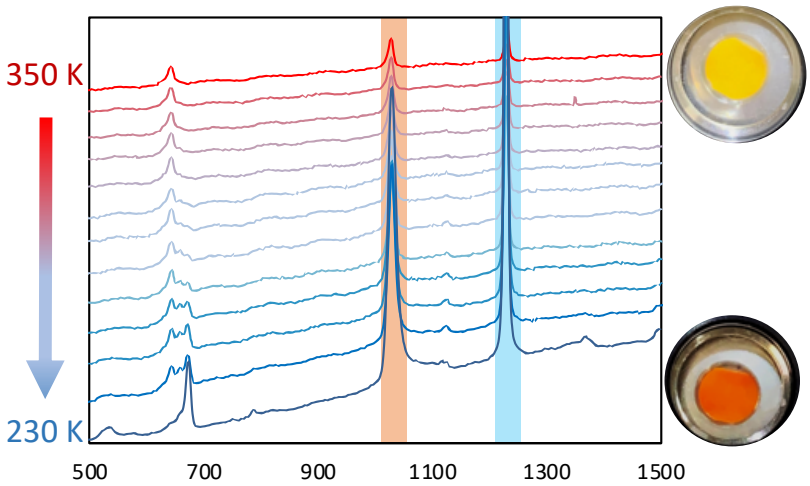

Figure 2-13. Temperature dependence of Raman spectra and guest-free **Pt30Pd30** colour at 350 K (yellow) and 230 K (orange).

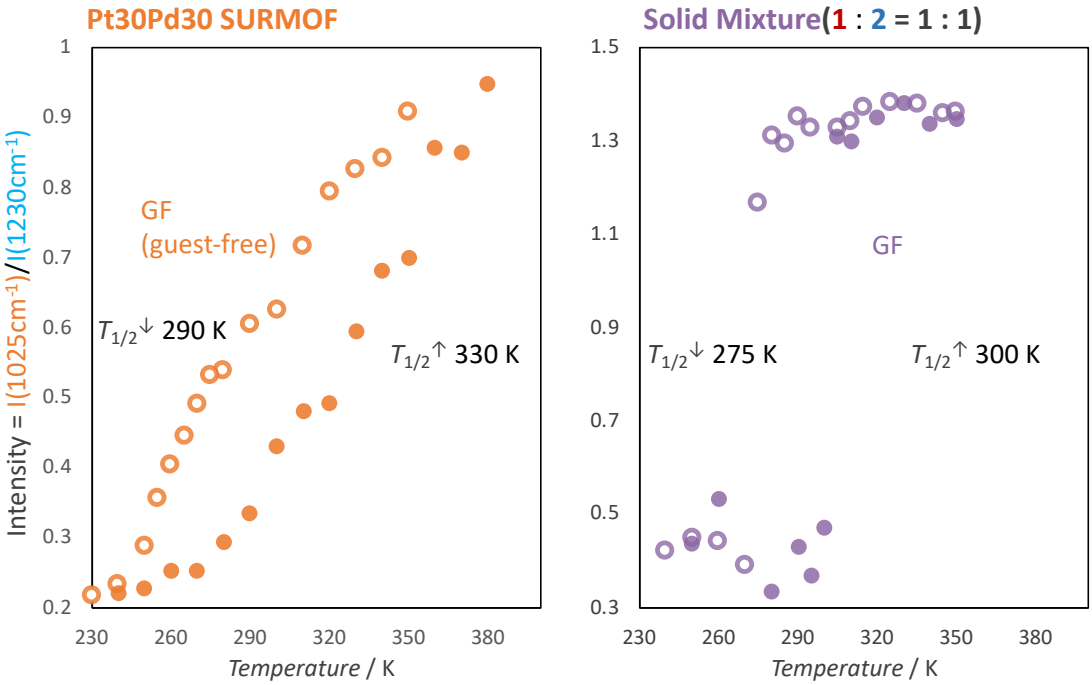

Figure 2-14. Temperature dependence of the normalized Raman intensity ratio (I(norm) = I(1025 cm^{-1})/I(1230 cm^{-1})) of guest-free **Pt30Pd30** and guest-free solid mixture (**1** : **2** = 1 : 1).

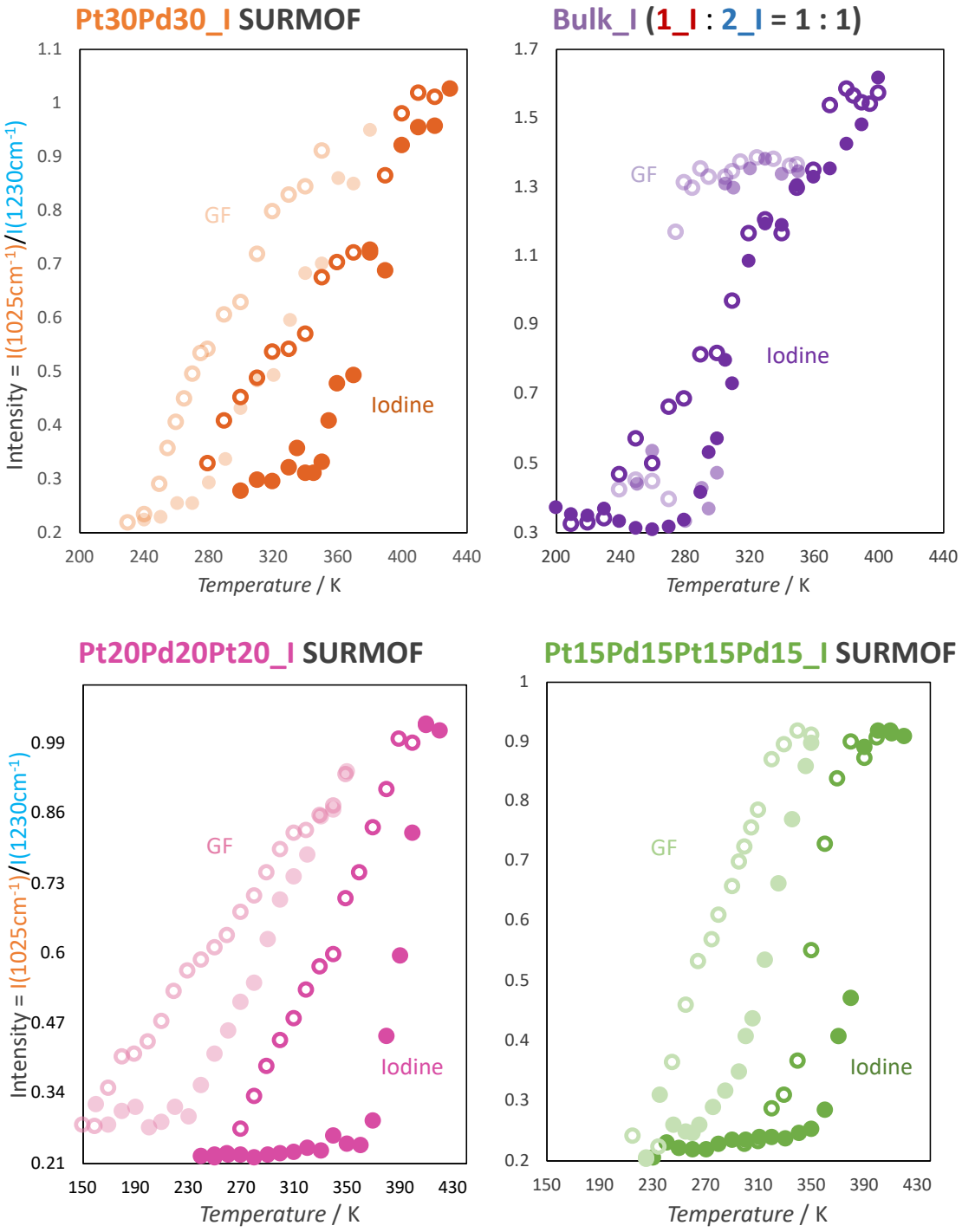

Figure 2-15. Temperature dependence of the normalized Raman intensity ratio (I(norm) = I(1025 cm^{-1})/I(1230 cm^{-1})) of guest-free/iodine-containing SURMOF (**Pt30Pd30**, **Pt20Pd20Pt20** and **Pt15Pd15Pt15Pd15**) and solid mixture (**1** : **2** = 1 : 1).

Conclusion

Hetero-structured surface-mounted MOFs (hetero-SURMOFs) consisting of "Pt block" {Fe(pz)[Pt(CN)$_4$]} (pz = pyrazine; **1**) and "Pd block" {Fe(pz)[Pd(CN)$_4$]} (**2**) were prepared. Compounds **1** and **2** which have similar lattice parameters are the acceptable combinations for forming hetero-SURMOFs. As mentioned in Chapter 1, when iodine is used for guest-molecules, compounds **1** and **2** show different magnetic behaviours due to the different interactions with iodine. In this work, three types of hetero-SURMOFs were prepared by the Layer-by-Layer (LbL) method. In this LbL method, the functionalized substrate is soaked into the metal precursor solution and ligand solution alternately. Therefore, the space for forming I–Pt^{IV}–I bonds and confiding I_2 molecules can be formed and designed the crystal stricture in these hetero-SURMOFs. The orientation and high crystallinity of guest-free hetero-SURMOFs were evaluated by XRD measurement, and the arrangement of Pt block and Pd block were confirmed by SEM-EDX images. In addition, the ST behaviour was evaluated using the intensity ratio of Raman spectra. Guest-free hetero-SURMOFs showed spin crossover (SCO) behaviour as well as bulk samples, however, the cooperativity decreased in SURMOF because of the downsizing effect. After exposing iodine vapour, peaks originated from I–Pt^{IV}–I bonds and I_2 molecules were observed in all hetero-SURMOFs by Raman spectroscopy. Because of forming I–Pt^{IV}–I bonds, the ST temperature T_C^{up} increased in all iodine-containing hetero-SURMOFs. Interestingly, only **Pt30Pd30_I** provided two-step SCO phenomena. In contrast, iodine-containing hetero-SURMOF **Pt20Pd20Pt20_I** showed increase of T_C^{up} and a bulge of hysteresis, and **Pt15Pd15Pt15Pd15** showed an only increase of T_C^{up}. For these results, the author considered the gain of the boundary surface and the decline of thickness provided the mixed state like solid solutions.

References

1. Wang, Z.; Wöll, C., *Adv. Mater. Tech.*, **2019**, *4*, 1800413.
2. Shekhah, O., *Materials (Basel)*, **2010**, *3*, 1302−1315.
3. Zacher, D.; Shekhah, O.; Wöll, C.; Fischer, R. A., *Chem. Soc. Rev.*, **2009**, *38*, 1418−1429.
4. Knebel, A.; Wulfert-Holzmann, P.; Friebe, S.; Pavel, J.; Strauß, I.; Mundstock, A.; Steinbach, F.; Caro, J.*, Chem. A Eur. J.*, **2018**, *24*, 5728−5733.
5. Liu, B.; Ma, M.; Zacher, D.; Bétard, A.; Yusenko, K.; Metzler-Nolte, N.; Wöll, C.; Fischer, R. A., *J. Am. Chem. Soc.*, **2011**, *133*, 1734−1737.
6. Talin, A. A.; Centrone, A.; Ford, A. C.; Foster, M. E.; Stavila, V.; Haney, P.; Kinney, R. A.; Szalai, V.; El Gabaly, F.; Yoon, H. P., *Science*, **2014**, *343*, 6669.
7. Qiu, S.; Xue, M.; Zhu, G., *Chem. Soc. Rev.*, **2014**, *43*, 6116−6140.
8. Peng, Y.; Li, Y.; Ban, Y.; Jin, H.; Jiao, W.; Liu, X.; Yang, W., *Science*, **2014**, *346*, 1356−1359.
9. Rodenas, T.; Luz, I.; Prieto, G.; Seoane, B.; Miro, H.; Corma, A.; Kapteijn, F.; Llabrés I Xamena, F. X.; Gascon, J., *Nat. Mater.*, **2015**, *14*, 4855.
10. Ye, L.; Liu, J.; Gao, Y.; Gong, C.; Addicoat, M.; Heine, T.; Wöll, C.; Sun, L., *J. Mater. Chem. A.*, **2016**, *4*, 15320−15326.
11. Gu, Z. G.; Pfriem, A.; Hamsch, S.; Breitwieser, H.; Wohlgemuth, J.; Heinke, L.; Gliemann, H.; Wöll, C., *Nano Lett.*, **2015**, *211*, 8287.
12. Shekhah, O.; Liu, J.; Fischer, R. A.; Wöll, C., *Chem. Soc. Rev.*, **2011**, *40*, 1081−1160.
13. Guerrero, V. V.; Yoo, Y.; McCarthy, M. C.; Jeong, H. K., *J. Mater. Chem.*, **2010**, *20*, 3938−3943.
14. Zhuang, J. L.; Ceglarek, D.; Pethuraj, S.; Terfort, A., *Adv. Funct. Mater.*, **2011**, *21*, 1442−1447.
15. Motoyama, S.; Makiura, R.; Sakata, O.; Kitagawa, H., *J. Am. Chem. Soc.*, **2011**, *133*, 5640−5643.
16. Zhuang, J. L.; Ar, D.; Yu, X. J.; Liu, J. X.; Terfort, A., *Adv. Mater.*, **2013**, *25*, 4631−4635.
17. Shekhah, O.; Wang, H.; Kowarik, S.; Schreiber, F.; Paulus, M.; Tolan, M.; Sternemann, C.; Evers, F.; Zacher, D.; Fischer, R. A., *J. Am. Chem. Soc.*, **2007**, *129*, 15118−15119.
18. Makiura, R.; Motoyama, S.; Umemura, Y.; Yamanaka, H.; Sakata, O.; Kitagawa, H., *Nat. Mater.*, **2010**, *9*, 565−571.

19. Arslan, H. K.; Shekhah, O.; Wohlgemuth, J.; Franzreb, M.; Fischer, R. A.; Wöll, C., *Adv. Funct. Mater.*, **2011**, *21*, 4228−4231.
20. Heinke, L.; Wöll, C., *Adv. Mater.*, **2019**, *31*, 1806324.
21. Shekhah, O.; Hirai, K.; Wang, H.; Uehara, H.; Kondo, M.; Diring, S.; Zacher, D.; Fischer, R. A.; Sakata, O.; Kitagawa, S., *Dalton. Trans.*, **2011**, *40*, 4954−4958.
22. Kŭcera, J.; Gross, A., *Langmuir*, **2008**, *24*, 1398513992.28, 6839−6847.
23. Ramírez, E. A.; Cortés, E.; Rubert, A. A.; Carro, P.; Benítez, G.; Vela, M. E.; Salvarezza, R. C., *Langmuir*, **2012**, *28*, 6839−6847.
24. Heinke, L.; Cakici, M.; Dommaschk, M.; Grosjean, S.; Herges, R.; Bräse, S.; Wöll, C., *ACS Nano*., **2014**, *8*, 1463−1467.
25. Cobo, S.; Molnár, G.; Real, J. A.; Bousseksou, A., *Angew. Chem. Int. Ed.*, **2006**, *45*, 5786−5789.
26. Molnár, G.; Cobo, S.; Real, J. A.; Carcenac, F.; Daran, E.; Vieu, C.; Bousseksou, A., *Adv. Mater.*, **2007**, *19*, 2163−2167.
27. Otsubo, K.; Haraguchi, T.; Sakata, O.; Fujiwara, A.; Kitagawa, H., *J. Am. Chem. Soc.*, **2012**, *134*, 9605–9608.
28. Molnár, G.; Niel, V.; Gaspar, A. B.; Real, J. A.; Zwick, A.; Bousseksou, A.; McGarvey, J. J., *J. Phys. Chem. B*, **2002**, *106*, 9701−9707.
29. Shekhah, O.; Wang, H.; Zacher, D.; Fischer, R. A.; Wöll, C., *Angew. Chem. Int. Ed.*, **2009**, *48*, 5038−5041.
30. Otsubo, K.; Haraguchi, T.; Kitagawa, H., *Coord. Chem. Rev.*, **2017**, *346*, 123138.
31. Shepherd, H. J.; Molnár, G.; Nicolazzi, W.; Salmon, L.; Bousseksou, A., Eur. J. *Inorg. Chem.*, **2013**, *5*, 653−661.
32. Mikolasek, M.; Félix, G.; Nicolazzi, W.; Molnár, G.; Salmon, L.; Bousseksou, A., *New J. Chem.*, **2014**, *38*, 1834−1839.
33. Molnár, G.; Rat, S.; Salmon, L.; Nicolazzi, W.; Bousseksou, A., *Adv. Mater.*, **2018**, *30*, 1703862.
34. Mishima, A.; Koshiyama, T.; Real, J. A.; Ohba, M., *J. Mater. Chem. C*, **2017**, *5*, 3706−3713.
35. Bousseksou, A.; Molnár, G.; Salmon, L.; Nicolazzi, W., *Chem. Soc. Rev.*, **2011**, *40*, 3313−3335.
36. Rubio-Giménez, V.; Bartual-Murgui, C.; Galbiati, M.; Núñez-López, A.; Castells-Gil, J.; Quinard, B.; Seneor, P.; Otero, E.; Ohresser, P.; Cantarero, A., *Chem. Sci.*, **2019**, *10*, 4038−4047.

Concluding Remarks

In this thesis, the author found the mixed-component (MC) approach was appropriate to design the framework and control guest molecules behaviour in the metal-organic framework (MOFs). The MC approach has been studied for combining each physical property of single MOFs, and the physical properties of the framework can be tuned or exceed by this approach. Here, the author focused on the correlation between the design of inter-layer space by MC approach and guest molecule behaviours.

3D Hofmann-type MOFs {Fe(pz)[M(CN)$_4$]} (pz = pyrazine, M = Pt (**1**), Pd (**2**), Ni) were selected as a platform because they showed spin crossover phenomenon depending on the interaction with the guest molecule. In other words, guest molecule behaviour can be observed through the magnetic measurement. In the previous work, **1** and **2** exhibited quite different magnetic behaviour when iodine was used for guest molecule. In Chapter 1, solid solutions {Fe(pz)[Pt$_x$Pd$_{1-x}$(CN)$_4$]} (**3*x***) were prepared and evaluated. Although guest-free **3*x*** exhibited similar magnetic behaviour regardless of the ratio of Pt/Pd, iodine-containing **3*x*_I** showed the different magnetic behaviour depending on the ratio of Pt/Pd. Therefore, iodine behaviour in the pore could be changed by the ratio of Pt/Pd. In addition, the author considered the arrangement of OMSs effected on iodine behaviour. Because of I–Pt^{IV}–I bonds, above and below sites could not confine I_2 molecules, and so wide hysteresis was obtained only when Pt content (*x*) was quite small. Therefore, in Chapter 2, the author focused on the Layer-by-Layer (LbL) method as the way to arrange OMSs. In order to design the inter-layer space for forming I–Pt^{IV}–I bonds and confining I_2 molecules, "Pt block" (**1**) and "Pd block" (**2**) were separated by the LbL method. As a result, magnetic behaviour was changed from two-step to one-step spin crossover (SCO) behaviour with increasing the number of boundary surface and decreasing block thickness. Hetero-SURMOF (hetero-structured surface-mounted MOF) which had thicker blocks exhibited two-step SCO originated each **1_I** and **2_I**, however, Pt sites and Pd sites were mixed around the boundary surface, and so hetero-SUFMOF which had thinner blocks exhibited one step SCO as well as solid solutions.

More recently, MOFs have been attracted attention as the multifunctional materials combining their porous property and physical properties. In this thesis, the author suggested the MC approach was appropriate to modulate physical properties linking with guest molecules behaviour, on demand.

List of Publications

Chapter 1

Tuning of Spin Transition Temperature and Hysteresis Width in 3D Hofmann-type Metal-organic frameworks using Two Kinds of Open Metal Sites

M. Tsuji, A. Mishima, R. Ohtani, O. Masaaki

Chemical Communications (to be submitted)

Acknowledgments

All the studies in this thesis have been carried out under the direction of Professor Masaaki Ohba during April 2015- March 2020 at the Department of Chemistry, Graduate School of Science, Kyushu University.

The author expresses her deepest appreciation to Professor Masaaki Ohba for his guidance and encouragement. The author could research liberally in the study due to his generosity. Because of his guidance, the author could learn a lot of things required to promote scientific studies, including the ways to how to design and think of her research project. The author thanks to Professor Ken Sakai, Professor Osamu Sato, Associate Professor Ryo Ohtani and Associate Professor Tomomi Koshiyama for their guidance.

The author expresses her gratitude to Professor Roland A. Fischer (Munich University of Technology) and for accepting her as visiting scholar and careful guidance, and valuable discussion.

The acknowledgement is also given the Advanced Graduate Course on Molecular Systems for Devices for the financial supports for the activities of the author, which enabled the author to attend various domestic and international conferences, together with his 9-months of oversea research in Germany.

Finally, the author gives special thanks to all members of Ohba group and Fischer group for their kind support.

Miho Tsuji
Department of Chemistry, Graduate School of Science,
Kyushu University March 2020